The Stability of Localized Spot Patterns for the Brusselator on the Sphere

I. ROZADA, S. RUUTH, M. J. WARD

Steven Ruuth, Dept. of Mathematical Sciences, Simon Fraser University, Burnaby, British Columbia, V5A 1S6, Canada, Ignacio Rozada and Michael Ward (corresponding author); Dept. of Mathematics, University of British Columbia, Vancouver, British Columbia, V6T 1Z2, Canada.

(*Received 27 August 2013*)

In the singularly perturbed limit of an asymptotically small diffusivity ratio ε^2, the existence and stability of localized quasi-equilibrium multi-spot patterns is analyzed for the Brusselator reaction-diffusion model on the unit sphere. Formal asymptotic methods are used to derive a nonlinear algebraic system that characterizes quasi-equilibrium spot patterns, and to formulate eigenvalue problems governing the stability of spot patterns to three types of "fast" $\mathcal{O}(1)$ time-scale instabilities; self-replication, competition, or oscillatory instabilities of the spot amplitudes. The nonlinear algebraic system and the spectral problems are then studied using simple numerical methods, with emphasis on the special case where the spots have a common amplitude. Overall, the theoretical framework provides a hybrid asymptotic-numerical characterization of the existence and stability of spot patterns that is asymptotically correct to within all logarithmic correction terms in powers of $\nu = -1/\log\varepsilon$. From a leading-order-in-ν analysis, and with an asymptotically large inhibitor diffusivity, some rigorous results for competition and oscillatory instabilities are obtained from an analysis of a new class of nonlocal eigenvalue problem (NLEP). Theoretical results for the stability of spot patterns are confirmed with full numerical computations of the Brusselator PDE system on the sphere using the Closest Point Method.

Key words: Brusselator, matched asymptotics, quasi-equilibria, nonlocal eigenvalue problem, Hopf bifurcation, sphere, localized spots, Closest-Point Method.

1 Introduction

Turing in [**38**] proposed that localized peaks in the concentration of a chemical substance, known as a morphogen, could be responsible for the process of morphogenesis, which describes the development of a complex organism from a single cell. By means of a linearized analysis, he showed how stable spatially inhomogeneous patterns can develop from small perturbations of spatially homogeneous initial data for a coupled system of reaction-diffusion (RD) equations.

Motivated by this initial work, a systematic and rigorous approach has been developed over the last few decades for the analysis of small amplitude patterns in RD systems. After linearizing the RD system around a spatially uniform state to identify bifurcation points for the emergence of spatially non-uniform patterns, a weakly nonlinear analysis based on a center manifold reduction leads to normal form ODE's characterizing the evolution of small amplitude patterns. The coefficients in these normal form ODE's are calculated in terms of the specific RD system, and the nature of the bifurcation (sub-critical or super-critical) established. However, when applied to the analysis of RD patterns on a sphere of increasingly large radius, or equivalently for an RD system in the singularly perturbed limit on the unit sphere, the pattern selection problem becomes increasingly intricate owing to the fact that there can be many eigenfunctions with the same growth rate. This degeneracy in the eigenspace associated with spherical harmonics leads to a coupled system of ODE's for the normal form amplitude equations. These normal form ODE's have an intricate bifurcation structure, and so the pattern that emerges from an interaction of these modes is difficult to

predict theoretically (see [**7**], [**9**], [**22**], [**23**], [**29**], and [**41**]). It is the goal of this paper to develop and then implement an alternative theoretical framework for analyzing RD patterns on the sphere.

There have been many numerical studies of RD patterns on the sphere and other compact manifolds (cf. [**8**], [**17**], [**3**], [**24**]) motivated by specific scientific applications, including those in [**28**], [**15**], and [**30**]. However, to date there has only been limited analytical work for analyzing RD patterns on surfaces. In contrast to a weakly nonlinear theory framework, our theoretical analysis is based not on the asymptotic closeness of parameters to a Turing bifurcation point, but instead it relies on an assumed large diffusivity ratio between the two species in the RD system. In this singularly perturbed limit, many RD systems allow for the existence of localized quasi-equilibrium solutions characterized by the concentration of one of the solution components at certain points in the domain. A survey of "far-from-equilibrium" pattern formation is given in [**27**]. Although our framework can be applied to a class of RD systems, for concreteness we will study the existence and stability of such localized spot patterns for a singularly perturbed Brusselator RD model (cf. [**31**]) on the surface of the unit sphere. Our choice for analyzing the Brusselator model is motivated by the fact that there have been no prior analytical studies of localized spot patterns for this model in 2-D, and that the analysis of the 1-D problem with spike solutions has only been performed recently (cf. [**39**], [**40**]). In addition, in the weakly nonlinear regime explicit normal form ODE's for the Brusselator on the sphere have been derived (cf. [**7**]). Finally, the Brusselator model has been proposed to model growing plant tips on a hemisphere (cf. [**24**]).

In the singularly perturbed limit of a large diffusivity ratio, the method of matched asymptotic expansions will be used to construct localized spot-type patterns for the Brusselator. A precise asymptotic characterization of these patterns and the parameter ranges where they occur will be found, and the stability of these patterns analyzed. Three types of fast $\mathcal{O}(1)$ time-scale instabilities of these patterns will be discovered and analyzed. These instabilities are a spot self-replication instability arising when a spot is sufficiently isolated, a competition instability leading to spot annihilation that occurs when spots are too-closely spaced, and an oscillatory instability of the spot amplitude. Parameter ranges where these three instabilities occur will be delineated. Our theoretical appproach is related to that done for the Gray-Scott model [**10**] and for the Schnakenburg model [**14**] in a planar domain.

In terms of a non-dimensional space variable, the standard form of the Brusselator [**31**] RD model is

$$U_T = \varepsilon_0^2 \Delta U + E - (B+1)U + U^2 V\,, \qquad V_T = D\Delta V + BU - U^2 V\,. \tag{1.1}$$

Here we have defined $\varepsilon_0^2 = D_u/L^2$, $D = D_v/L^2$, where L is a characteristic length-scale, and D_u, D_v are the diffusivities of U and V. We will consider the singularly perturbed limit $\varepsilon_0 \to 0$ while maintaining an asymptotically large diffusivity ratio $D_v/D_u = \mathcal{O}(\varepsilon_0^{-2})$ so that $D = D_v/L^2 = \mathcal{O}(1)$ as $\varepsilon_0 \to 0$.

In the parameter regime where $E = \mathcal{O}(\varepsilon_0)$, (1.1) for $\varepsilon_0 \to 0$ has localized spot solutions that are characterized by the concentration of U at discrete points in the domain. It is convenient to choose a scaling of (1.1) for which these spots have an $\mathcal{O}(1)$ amplitude as $\varepsilon_0 \to 0$. Upon writing $E = \varepsilon_0 \mathrm{E}_0$ with $\mathrm{E}_0 = \mathcal{O}(1)$, the appropriate re-scaling $T = t/(B+1)$, $U = Bu/\varepsilon_0$, and $V = \varepsilon_0 v$, of (1.1), as outlined in Appendix A, leads to the singularly perturbed RD system

$$u_t = \varepsilon^2 \Delta u + \varepsilon^2 \mathrm{E} - u + f u^2 v\,, \qquad \tau v_t = \mathcal{D}\Delta v + \frac{1}{\varepsilon^2}(u - u^2 v)\,. \tag{1.2 a}$$

Here we have defined f, τ, E, $\mathcal{D}$, and ε, by

$$f \equiv \frac{B}{B+1}\,, \qquad \tau \equiv \frac{1}{f^2}\,, \qquad \mathrm{E} \equiv \frac{\mathrm{E}_0}{B}\,, \qquad \mathcal{D} \equiv \frac{D(B+1)}{B^2}\,, \qquad \varepsilon \equiv \frac{\varepsilon_0}{\sqrt{B+1}}\,. \tag{1.2 b}$$

This system has three independent bifurcation parameter E, $\mathcal{D}$, and f, depending on D, B, and E_0, with f defined in the narrow interval $0 < f < 1$. In our non-dimensionalization we chose not to scale v by an $\mathcal{O}(1)$ constant, as this

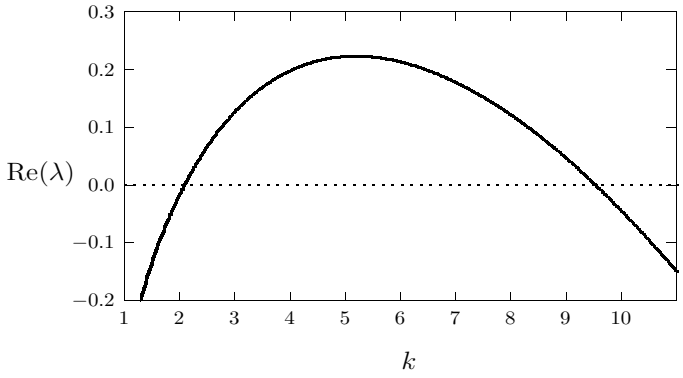

FIGURE 1. The growth rate $\mathrm{Re}(\lambda)$ versus k for the linearization of (1.2) around the spatially homogeneous equilibrium $u_e = \varepsilon^2\mathrm{E}/(1-f)$ and $v_e = (1-f)/(\mathrm{E}\varepsilon^2)$ for $f = 0.8$, $\varepsilon = 0.075$, $\mathcal{D} = 0.2$, $\tau = 1.5625$, and $\mathrm{E} = 4$, on the unit sphere. For $\varepsilon \ll 1$, the upper edge of the instability band is $k_{\mathrm{up}} \sim \sqrt{2f-1}/\varepsilon \approx 10.32$, which agrees well with the numerical result of $k_{\mathrm{up}} \approx 9.57$. The lower edge of the instability band is $k_{\mathrm{low}} \approx 2.11$. Any spherical harmonic $Y_l^m(\theta,\phi)$ with integers l and m satisfying $k_{\mathrm{low}}^2 < l(l+1) < k_{\mathrm{up}}^2$ and $|m| < l$ are linearly unstable. There are many unstable spherical harmonics with roughly comparable growth rates.

allows us to better isolate bifurcations due to changes in the feed-rate parameter E. We will consider (1.2) on the surface of the unit sphere for which $\Delta \equiv \Delta_s$, where Δ_s is the Laplace-Beltrami operator

$$\Delta_s u \equiv \frac{1}{\sin^2\theta}u_{\phi\phi} + \frac{1}{\sin\theta}(\sin\theta\, u_\theta)_\theta\,, \qquad 0 < \theta < \pi\,, \qquad 0 < \phi < 2\pi\,.$$

With the asymptotically large diffusivity ratio in (1.2), localized large amplitude patterns are readily observed in full numerical simulations of (1.2) with initial conditions close to the spatially uniform state $u_e = \varepsilon^2\mathrm{E}/(1-f)$ and $v_e = (1-f)/(\varepsilon^2\mathrm{E})$. Introducing the perturbation $(u,v) = (u_e, v_e) + e^{\lambda t}Y_l^m(\theta,\phi)$, we readily derive that the growth rate λ satisfies $\tau\lambda^2 - T_k\lambda + d_k = 0$, where

$$T_k \equiv (2f-1)\tau - \tau\varepsilon^2k^2 - \mathcal{D}k^2 - \frac{\varepsilon^2\mathrm{E}^2}{(1-f)^2}\,, \qquad d_k \equiv \frac{\varepsilon^2\mathrm{E}^2}{(1-f)} - (2f-1)\mathcal{D}k^2 + \mathcal{D}\varepsilon^2k^4 + \frac{\varepsilon^4\mathrm{E}^2k^2}{(1-f)^2}\,,$$

with $k^2 \equiv l(l+1)$ and $|m| \le l$.

For $0 < f < 1/2$, we have $T_k < 0$ and $d_k > 0$ for all k, and there is no instability of the spatially uniform state. However, for $1/2 < f < 1$, the $k = 0$ mode is unstable as $\varepsilon \to 0$ but it may be stable at finite ε. Therefore, there exists a lower edge $k_{\mathrm{low}} \ge 0$ of the instability band for which $\mathrm{Re}(\lambda) > 0$ when $k_{\mathrm{low}} < k < k_{\mathrm{up}}$. A simple calculation shows that the upper edge k_{up} of the instability band satisfies $k_{\mathrm{up}} \sim \sqrt{2f-1}/\varepsilon$ when $\varepsilon \ll 1$. Since all the spherical harmonics $Y_l^m(\theta,\phi)$ with integers $l \ge 0$ and m satisfying $k_{\mathrm{low}}^2 \le l(l+1) < k_{\mathrm{up}}^2$ and $|m| < l$ are linearly unstable when $1/2 < f < 1$, the linear stability problem of the spatially uniform state is highly degenerate when $\varepsilon \ll 1$. To illustrate this, in Fig. 1 we plot the growth rate $\mathrm{Re}(\lambda)$ versus k for $f = 0.8$, $\varepsilon = 0.075$, $\mathcal{D} = 0.2$, $\tau = 1.5625$, and $\mathrm{E} = 4$. We obtain that the unstable modes of the spherical harmonics $Y_l^m(\theta,\phi)$ satisfy $4.45 \le l(l+1) \le 91.6$ and $|m| \le l$, which yields $l = 2,\ldots,9$. Moreover, the results in this figure show that the growth rate is rather flat near the most unstable mode, which suggests that the transient development of small amplitude patterns is a consequence of the interaction of many unstable modes with comparable growth rates.

For the parameter values of Fig. 1, in Fig. 2 we show results from a full numerical simulation of (1.2) using the numerical method of §6.1. The initial condition was a 2% random perturbation of the spatially uniform state $u_e = \varepsilon^2\mathrm{E}/(1-f)$ and $v_e = (1-f)/(\mathrm{E}\varepsilon^2)$ as given below in (6.1). Due to the weakly nonlinear interaction of many unstable spherical harmonics, the transient dynamics at short times as seen in Fig. 2 is very intricate. However, as time

increases the pattern becomes localized with eight observable spots at $t = 75$. The goal of this paper is to characterize the existence and stability properties of these localized spot patterns.

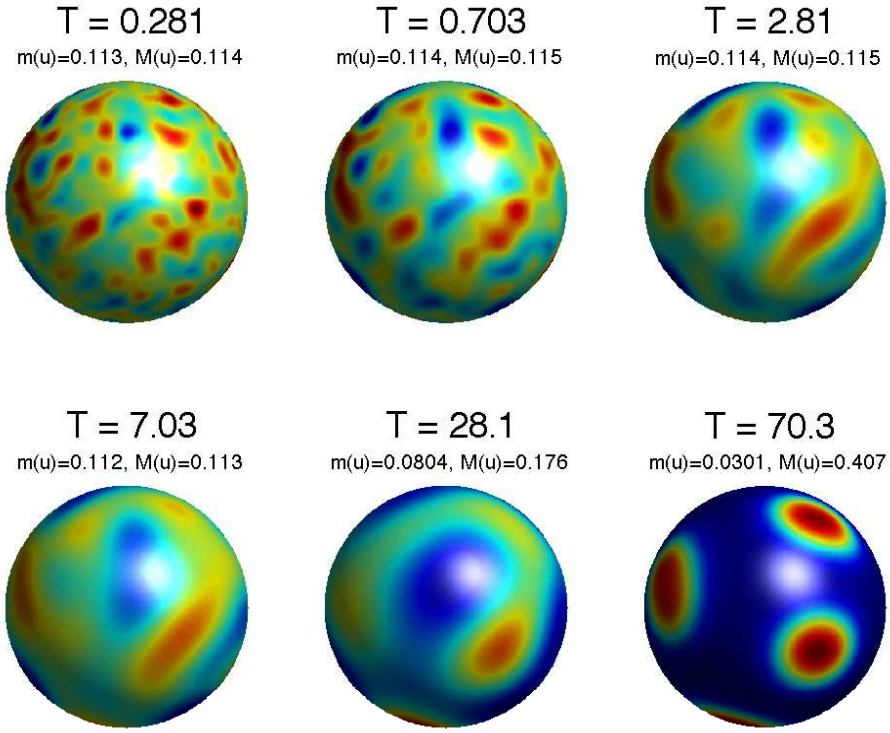

FIGURE 2. Full numerical computations for (1.2) on the unit sphere for $f = 0.8$, $\varepsilon = 0.075$, $\mathcal{D} = 0.2$, $\tau = 1/f^2$, and E = 4. The initial data (6.1) represents a 2% random perturbation from the spatially uniform state. There is a very complicated transient dynamics due to the weakly nonlinear interaction of many unstable spherical harmonics. A distinct localized pattern with 8 localized spots has emerged by the last frame at $t \approx 70.3$. The amplitudes of the spots as compared to their background state is $\approx 0.407 = \mathcal{O}(1)$. Here $m(U)$ and $M(u)$ denote the minimum and maximum of u on the sphere. This is Experiment 1 of §6.

In §2 we use formal asymptotic methods to construct quasi-equilibrium spot patterns. In the outer region, away from the spots centered at $\{x_1, \ldots, x_N\}$, we show that the inhibitor concentration field v in (1.2) can be represented asymptotically as a sum of Green's functions, where each spot corresponds to a Coulomb singularity of the form $v \sim \mathcal{D}^{-1/2} S_j \log|x - x_j|$ as $x \to x_j$ for $j = 1, \ldots, N$. We show that the construction of a quasi-equilibrium spot pattern can be reduced to the problem of determining the "source strengths" $S_1, \ldots, S_N$ from a nonlinear algebraic system.

In §3 we formulate eigenvalue problems governing the linear stability of spot patterns to the three types of "fast" $\mathcal{O}(1)$ time-scale instabilities discuussed above. In §3.1 we analyze spot self-replication instabilities resulting from non-radially symmetric perturbations near an individual spot. These instabilities are local in the sense that a peanut-splitting instability occurs if an individual source strength S_j exceeds some threshold value $\Sigma_2(f)$. Numerical evidence shows that this instability for $S_j > \Sigma_2(f)$ leads to spot self-replication. In contrast, in the class of radially symmetric perturbations near each spot, in §3.2 we formulate a globally coupled eigenvalue problem that governs competition and oscillatory instabilities of the spot amplitudes. We then investigate the thresholds for these instabilities for spot patterns that have a common source strength $S_c \equiv S_j$ for $j = 1, \ldots, N$. In §3.3 it is shown that competition instabilities,

which result from zero eigenvalue crossings, occur for multi-spot patterns whenever $\mathcal{D}$ exceeds a threshold. This linear instability mechanism, which preserves the sum of the amplitude perturbations of the spots, is found numerically to lead to spot annihilation. In §3.4 we calculate thresholds for oscillatory instabilities of the spot amplitudes formulated in terms of the roots of transcendental equations involving certain Legendre functions. We emphasize that the existence and stability theory of §2 and §3 is asymptotically correct to within all logarithmic correction terms in powers of $\nu = -1/\log\varepsilon$.

In §4 we formulate a leading-order-in-ν existence and stability theory of multi-spot patterns for the case of large diffusivity where $\mathcal{D} = \mathcal{O}(\nu^{-1})$. In this regime, for which $S_j \ll 1$, there are no spot self-replication instabilities, as these occur only when $S_j > \Sigma_2(f) = \mathcal{O}(1)$. This leading-order-in-$\nu$ theory leads to a new class of nonlocal eigenvalue problem (NLEP) whose spectrum governs, to leading order, any competition and oscillatory instabilities of the spot amplitudes. A similar leading-order-in-ν theory, leading to NLEP's of a related but simpler form, have been derived and analyzed for classifying the stability of multi-spot patterns for other RD systems such as the Gray-Scott, Schnakenburg, and Gierer-Meinhardt models (cf. [**44**], [**45**], [**46**], [**47**], and [**48**]). In §4.4 we analyze the spectrum of our more complicated NLEP for the Brusselator by extending some of these prior rigorous results.

In §5 we give some results that determine where spots are to be located on the sphere to ensure that the quasi-equilibrium pattern has spots of a common source strength.

As a partial confirmation of our stability theory, numerical experiments are undertaken in §6 for the full Brusselator model (1.2) to investigate spot self-replication, competition, and oscillatory instabilities for moderate values of ε. The comparisons between results from our stability theory and full numerics are done for various scenarios including, spot patterns on a slowly growing sphere, or spot patterns resulting from an increase or decrease in the "fuel" supply E. To solve the Brusselator model for moderate values of ε on a sphere, or other smooth manifold, we use the explicit Closest Point Method [**34**]. The Closest Point Method [**34**, **19**] is a general numerical method that approximates PDEs on smooth surfaces in 3-D by alternating between an interpolation step and a 3-D PDE evolution step. Because the method is composed of standard algorithmic components, it is particularly straightforward to implement and has the additional advantage of having an automatic extension to arbitrary smooth surfaces. In §6 this extension is illustrated for a specific non-spherical surface. Further details on the Closest Point Method and our discretizations are provided in Section 6.1. These comparisons between full numerics and the asymptotic theory at moderate ε show that the asymptotic theory is still quantitatively reliable when $\varepsilon = 0.075$ and $\mathcal{D} = 0.2$, which gives a diffusivity ratio of only 36.

Finally, in the concluding section §7 a few open problems are discussed.

2 The Core Problem and the Construction of a Quasi-Equilibrium Solution

In this section we construct a quasi-steady, or quasi-equilibrium, multi-spot pattern for (1.2) in the limit $\varepsilon \to 0$. We first formulate the local (or inner) problem that determines the profile of an isolated spot. We center a spot at the angular coordinates $\phi = \phi_j$ and $\theta = \theta_j$, and we define

$$y_1 = \hat{\phi}\sin\theta_j\,, \quad y_2 = \hat{\theta}\,, \qquad \text{where} \qquad \hat{\phi} = \varepsilon^{-1}(\phi - \phi_j)\,, \quad \hat{\theta} = \varepsilon^{-1}(\theta - \theta_j)\,.$$

Then, in the inner region near this spot we obtain, up to an $\mathcal{O}(\varepsilon)$ error, that $\Delta_s u = \Delta_y u \equiv u_{y_1y_1} + u_{y_2y_2} + \mathcal{O}(\varepsilon)$. With this local tangent-plane approximation to the sphere, we now construct a quasi-equilibrium multi-spot pattern with spots centered at (ϕ_j, θ_j) for $j = 1, \ldots, N$.

In the inner region near the j-th spot, we obtain to leading-order in ε that (1.2) reduces to

$$\Delta_y U_j - U_j + f U_j^2 V_j = 0\,, \qquad \mathcal{D}\Delta_y V_j + U_j - U_j^2 V_j = 0\,, \tag{2.1}$$

on $-\infty < y_1, y_2 < \infty$. We seek a radially symmetric solution to this problem after first rescaling U_j and V_j as

$$U_j = \sqrt{\mathcal{D}} u_j\,, \qquad V_j = v_j/\sqrt{\mathcal{D}}\,, \tag{2.2}$$

to eliminate $\mathcal{D}$. In this way, we obtain that $u_j(\rho)$ and $v_j(\rho)$ satisfy the radially symmetric problem

$$\begin{aligned} &\Delta_\rho u_j - u_j + f u_j^2 v_j = 0\,, \qquad \Delta_\rho v_j + u_j - u_j^2 v_j = 0\,, \qquad 0 < \rho < \infty\,, \\ &u_j'(0) = v_j'(0) = 0\,; \qquad u_j \to 0 \quad \text{and} \quad v_j \sim S_j \log\rho + \chi(S_j; f) + o(1) \quad \text{as} \quad \rho \to \infty\,, \end{aligned} \tag{2.3}$$

where f is a bifurcation parameter. This problem is called the *core problem*. Here we have defined $\rho \equiv \sqrt{y_1^2 + y_2^2}$ and $\Delta_\rho \equiv \partial_{\rho\rho} + \frac{1}{\rho}\partial_\rho$. Upon integrating the two boundary value problems in (2.3) over $0 < \rho < \infty$, we readily derive that

$$S_j = \int_0^\infty (u_j^2 v_j - u_j)\rho\, d\rho = (1-f)\int_0^\infty u_j^2 v_j \rho\, d\rho\,. \tag{2.4}$$

The key feature in (2.3) is that we must impose that $v_j \sim S_j \log\rho$ as $\rho \to \infty$, which is appropriate for $\Delta_\rho v_j = (u_j^2 v_j - u_j)$ given that $u_j \to 0$ at infinity. The constant S_j is a parameter at this stage, but it will eventually be determined after the asymptotic matching of the inner and outer solutions for v. In terms of S_j and the bifurcation parameter f, the function $\chi(S_j; f)$ is computed numerically from the limiting process $\lim_{\rho\to\infty}(v_j - S_j\log\rho) = \chi(S_j; f)$. We remark that, in contrast to the parameter-free related core problem identified for the Gray-Scott model in [**10**], the core problem (2.3) for the Brusselator involves a bifurcation parameter f.

The core problem (2.3) is solved numerically for various f and S_j by approximating the infinite domain by the finite domain $0 \le \rho \le R$, where $R \gg 1$. In this way, $\chi(S_j; f)$ is determined by computing v_j at $\rho = R$. The results shown in Fig. 3 are for $R = 15$. Increasing R did not change these results to a few significant digits. The spot profile $u_j(\rho)$ is seen to develop a volcano shape as S_j increases.

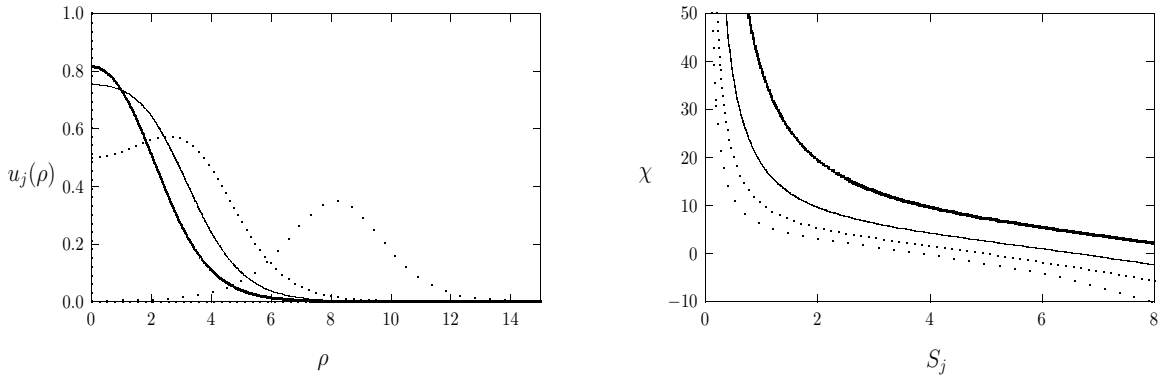

FIGURE 3. Left panel: the spot solution $u_j(\rho)$ computed numerically from (2.3) when $S_j = 8$ for $f = 0.3$ (heavy solid curve), $f = 0.4$ (solid curve), $f = 0.5$ (dotted curve), $f = 0.6$ (widely spaced dots). As f increases, u_j develops a volcano shape. Right panel: the function $\chi(S_j; f)$ defined in the asymptotic boundary condition in (2.3) for $f = 0.3$, $f = 0.4$, $f = 0.5$, and $f = 0.6$, with the same labelling as in the left panel.

Next, we asymptotically match the far-field behaviours of the inner solutions near each spot to a certain global solution for v, which we will construct. In doing so, we will derive a nonlinear algebraic system of equations for the unknowns S_j, referred to as the "source strengths". Our asymptotic analysis has the important feature that it retains

all of the logarithmic terms in $\nu \equiv -1/\log\varepsilon$ as $\varepsilon \to 0$, and so our asymptotic approximation for the solution and for the source strengths has an error that is algebraic, rather than logarithmic, in ε.

To determine the far-field behaviour of each inner solution we recall from (2.2) that $u = D^{1/2}u_j$ and $v = D^{-1/2}v_j$, with $v_j \sim S_j \log|y| + \chi(S_j; f) + o(1)$ as $|y| \to \infty$. We let $x_j = (\cos\phi_j \sin\theta_j, \sin\phi_j \sin\theta_j, \cos\theta_j)$ be a point on the unit sphere. Then, by Lemma B.1 of Appendix B, we have that

$$|x - x_j| = \varepsilon|y|(1 + o(1)) \quad \text{as} \quad x \to x_j\,, \quad \text{with} \quad y = (y_1\,, y_2)^T \equiv (\hat{\phi}\sin\theta_j, \hat{\theta})^T\,,$$

where $\hat{\phi} = \varepsilon^{-1}(\phi - \phi_j)$ and $\hat{\theta} = \varepsilon^{-1}(\theta - \theta_j)$. Thus, we obtain the following far-field behaviour of the inner solution

$$v \sim \mathcal{D}^{-1/2}\left[S_j \log|x - x_j| + \frac{S_j}{\nu} + \chi(S_j; f)\right] \quad \text{as} \quad x \to x_j\,, \quad j = 1, \ldots, N\,; \qquad \nu \equiv -\frac{1}{\log\varepsilon}\,, \tag{2.5}$$

which provides the singularity behaviour of the outer solution for v at each x_j.

Next, we study the outer solution for (1.2). In the outer region away from $\mathcal{O}(\varepsilon)$ neighborhoods of the spot locations $\{x_1, \ldots, x_N\}$ we have that $\varepsilon^2\mathrm{E} - u + fu^2v = 0$, so that $u \sim \varepsilon^2\mathrm{E} + \mathcal{O}(\varepsilon^2)$. By combining the inner and outer approximations for u, we get the leading-order uniformly valid approximation for u given by

$$u \sim \varepsilon^2\mathrm{E} + \mathcal{D}^{1/2}\sum_{j=1}^{N} u_j\left(\varepsilon^{-1}|x - x_j|\right)\,. \tag{2.6}$$

We then must estimate the term $\varepsilon^{-2}(u - u^2v)$ in the v-equation of (1.2) in the sense of distributions. The evaluation of this term requires care in order to retain both the local contribution near each spot and the global contribution arising from the non-vanishing outer solution for u. In the sense of distributions, we obtain upon using (2.4) that

$$\frac{1}{\varepsilon^2}(u - u^2v) \sim \mathrm{E} + 2\pi\mathcal{D}^{1/2}\sum_{j=1}^{N}\left(\int_0^\infty (u_j - u_j^2v_j)\,\rho\,d\rho\right)\delta(x - x_j) = \mathrm{E} - 2\pi\mathcal{D}^{1/2}\sum_{j=1}^{N} S_j\,\delta(x - x_j)\,.$$

By using this result together with the matching condition (2.5) for v, the outer problem for v is

$$\Delta_s v + \frac{\mathrm{E}}{\mathcal{D}} = \frac{2\pi}{\sqrt{\mathcal{D}}}\sum_{j=1}^{N} S_j\delta(x - x_j)\,, \quad x \in \Omega\,; \qquad v \sim \frac{1}{\sqrt{\mathcal{D}}}\left[S_j\log|x - x_j| + \frac{S_j}{\nu} + \chi(S_j; f)\right] + o(1) \quad \text{as} \quad x \to x_j\,, \tag{2.7}$$

for $j = 1 \ldots, N$, where Ω is the surface of the unit sphere. By pre-specifying the form of the non-singular $\mathcal{O}(1)$ term in each singularity condition as $x \to x_j$, we will obtain a nonlinear algebraic system for the source strengths $S_1, \ldots, S_N$.

To solve (2.7) we introduce the source-neutral Green's function $G(x; x_0)$ defined as the unique solution to

$$\Delta_s G = \frac{1}{4\pi} - \delta(x - x_0)\,, \qquad \int_\Omega G\,dx = \int_0^{2\pi}\int_0^{\pi} G\sin\theta\,d\theta d\phi = 0\,. \tag{2.8}$$

Here G is 2π periodic in ϕ, is smooth at the poles $\theta = 0, \pi$, and the integral condition eliminates an otherwise arbitrary constant in G, and thus specifies it uniquely. It is well known (cf. [**26**] and the references therein) that

$$G(x; x_0) = -\frac{1}{2\pi}\log|x - x_0| + R, \qquad R \equiv \frac{1}{4\pi}(\log 4 - 1)\,. \tag{2.9}$$

The solution to (2.7) is readily obtained in terms of G as

$$v = -\frac{2\pi}{\sqrt{\mathcal{D}}}\sum_{j=1}^{N} S_j G(x; x_j) + \frac{\bar{v}}{\sqrt{\mathcal{D}}}\,, \qquad \text{where} \qquad \sum_{j=1}^{N} S_j = \frac{2\mathrm{E}}{\sqrt{\mathcal{D}}}\,. \tag{2.10}$$

Here $\bar{v}$ is an arbitrary constant that must be determined as part of the analysis.

As $x \to x_i$, the matching condition in (2.7), together with the explicit solution for v in (2.10), yields that

$$-\frac{2\pi}{\sqrt{\mathcal{D}}}\left[-\frac{S_i}{2\pi}\log|x-x_i|+S_iR\right]-\frac{2\pi}{\sqrt{\mathcal{D}}}\sum_{\substack{j=1\\ j\neq i}}^{N}S_jG_{ij}+\frac{\bar{v}}{\sqrt{\mathcal{D}}}\sim\mathcal{D}^{-1/2}\left[S_i\log|x-x_i|+\frac{S_i}{\nu}+\chi(S_i;f)\right],$$

for $i=1,\dots,N$. With $G_{ij}\equiv G(x_i;x_j)$, we obtain the $N+1$ nonlinear algebraic equations for S_i and $\bar{v}$ given by

$$\frac{S_i}{\nu}+2\pi\left(S_iR+\sum_{j\neq i}^{N}S_jG_{ij}\right)+\chi(S_i;f)=\bar{v}\,,\quad i=1,\dots,N\,;\qquad\sum_{i=1}^{N}S_i=\frac{2\mathrm{E}}{\sqrt{\mathcal{D}}}\,. \tag{2.11}$$

Next, we write (2.11) in a more convenient form by using (2.9) to decompose G_{ij} as $G_{ij}=-\frac{1}{2\pi}L_{ij}+R$, where $R=\frac{1}{4\pi}(\log 4-1)$ and $L_{ij}\equiv\log|x_i-x_j|$. In this way, (2.11) becomes

$$S_i-\nu\sum_{j\neq i}^{N}S_jL_{ij}+\frac{\nu R_0\mathrm{E}}{\sqrt{\mathcal{D}}}+\nu\chi(S_i;f)=\nu\bar{v}\,,\quad i=1,\dots,N\,;\qquad\sum_{j=1}^{N}S_j=\frac{2\mathrm{E}}{\sqrt{\mathcal{D}}}\,,\qquad R_0\equiv\log 4-1\,. \tag{2.12}$$

Before re-casting (2.12) in matrix form, we make a few remarks. Firstly, the nonlinearity in (2.12) arises from the $\chi(S_i;f)$ term, which is determined from the nonlinear core problem (2.3). For each $S_j>0$ and f in $0<f<1$ our numerical results indicate that there is a unique solution to (2.3). For a given set of spot locations $\{x_1,\dots,x_N\}$, any solution $S_1,\dots,S_N$ and $\bar{v}$ to (2.12) determines a quasi-equilibrium pattern. However, due to the intractability of solving (2.12) analytically, the solvability of this system must typically be explored numerically.

To re-write (2.12) in matrix form, we introduce

$$\mathbf{S}\equiv\begin{pmatrix}S_1\\ \vdots\\ S_N\end{pmatrix},\quad\mathbf{e}\equiv\begin{pmatrix}1\\ \vdots\\ 1\end{pmatrix},\quad\chi\equiv\begin{pmatrix}\chi(S_1;f)\\ \vdots\\ \chi(S_N;f)\end{pmatrix},\quad\mathcal{G}\equiv\begin{pmatrix}0 & L_{12} & \cdots & L_{1N}\\ L_{21} & \ddots & & \vdots\\ \vdots & & & \\ L_{N1} & \cdots & & 0\end{pmatrix},\quad L_{ij}\equiv\log|x_i-x_j|\,, \tag{2.13}$$

so that (2.12) becomes

$$(I-\nu\mathcal{G})\mathbf{S}+\nu\chi=\nu\left(\bar{v}-\frac{R_0\mathrm{E}}{\sqrt{\mathcal{D}}}\right)\mathbf{e}\,,\qquad\mathbf{e}^T\mathbf{S}=\frac{2\mathrm{E}}{\sqrt{\mathcal{D}}}\,.$$

Upon pre-multiplying this equation by $\mathbf{e}^T$ we can readily decouple the nonlinear algebraic system for $\mathbf{S}$ and $\bar{v}$. After a short calculation we obtain that $\mathbf{S}$ satisfies

$$\mathbf{S}-\nu(I-\mathcal{E}_0)\mathcal{G}\mathbf{S}+\nu(I-\mathcal{E}_0)\chi=\frac{2\mathrm{E}}{\sqrt{\mathcal{D}}N}\mathbf{e}\,,\qquad\text{where}\quad\mathcal{E}_0\equiv\frac{1}{N}\mathbf{e}\mathbf{e}^T=\frac{1}{N}\begin{pmatrix}1 & \cdots & 1\\ \vdots & & \vdots\\ 1 & \cdots & 1\end{pmatrix}, \tag{2.14 a}$$

while $\bar{v}$ is given by

$$\bar{v}=\frac{2\mathrm{E}}{\sqrt{\mathcal{D}}N\nu}+\frac{R_0\mathrm{E}}{\sqrt{\mathcal{D}}}+\frac{1}{N}(\mathbf{e}^T\chi-\mathbf{e}^T\mathcal{G}\mathbf{S})\,. \tag{2.14 b}$$

We summarize our result as follows:

Principal Result 2.1 *Let $\varepsilon\to 0$ and define $\nu=-1/\log\varepsilon\ll 1$. Suppose that the nonlinear algebraic system (2.14 a) for the source strengths S_j, for $j=1,\dots,N$, has a solution. Then, there is a quasi-equilibrium solution u_{qe} and v_{qe} for the Brusselator model (1.2) with leading-order uniformly valid asymptotics given by*

$$u_{qe}\sim\varepsilon^2\mathrm{E}+\mathcal{D}^{1/2}\sum_{j=1}^{N}u_j\left(\varepsilon^{-1}|x-x_j|\right),\qquad v_{qe}\sim\begin{cases}\frac{1}{\sqrt{\mathcal{D}}}v_j\left(\varepsilon^{-1}|x-x_j|\right) & \text{for } |x-x_j|=\mathcal{O}(\varepsilon)\\ -\frac{2\pi}{\sqrt{\mathcal{D}}}\sum_{i=1}^{N}S_iG(x;x_i)+\frac{\bar{v}}{\sqrt{\mathcal{D}}} & \text{for } |x-x_j|\gg\mathcal{O}(\varepsilon)\end{cases}, \tag{2.15}$$

where $\bar{v}$ is given in (2.14 b). In (2.15) each spot profile $v_j(\rho)$ and $u_j(\rho)$ for $j = 1, \ldots, N$ satisfies the core problem (2.3) *defined in terms of f and the local source strength S_j, as determined from the coupled system (2.14 a).*

3 Stability Analysis of the Quasi-Equilibrium Pattern

In this section we study the linear stability of the N-spot quasi-equilibrium solution of §2 to $\mathcal{O}(1)$ time-scale instabilities. The $\mathcal{O}(1)$ time-scale of such instabilities is fast in comparison with the expected slow dynamics of the spots with speed $\mathcal{O}(\varepsilon^2)$. Therefore, in the stability analysis we "freeze" the locations of the spots and analyze whether the resulting quasi-equilibrium pattern is linearly stable to fast $\mathcal{O}(1)$ time-scale instabilities. If the quasi-equilibrium pattern is stable to these fast instabilities, the pattern will be quasi-steady and evolve slowly on an asymptotically long time-scale as $\varepsilon \to 0$. Our analysis shows that there are are three distinct types of instabilities that can occur in different parameter regimes. Criteria for the onset of these instabilities will be derived. We remark that our stability analysis is accurate to all powers of the logarithmic gauge $\nu = -1/\log\varepsilon$.

We first linearize around the quasi-equilibrium solution of Principal Result 2.1 by writing

$$u = u_{qe} + e^{\lambda t}\psi\,, \qquad v = v_{qe} + e^{\lambda t}\eta\,.$$

Upon substituting this into (1.2) and linearizing, we obtain the eigenvalue problem

$$\varepsilon^2\Delta_s\psi - \psi + 2fu_{qe}v_{qe}\psi + fu_{qe}^2\eta = \lambda\psi\,, \qquad \mathcal{D}\Delta_s\eta + \frac{1}{\varepsilon^2}(\psi - 2u_{qe}v_{qe}\psi - u_{qe}^2\eta) = \tau\lambda\eta\,. \tag{3.1}$$

In the inner region near the j-th spot, we introduce the local coordinates

$$\hat{\phi} = \varepsilon^{-1}\left(\phi - \phi_j\right)\,, \qquad \hat{\theta} = \varepsilon^{-1}\left(\theta - \theta_j\right)\,, \qquad y_1 = \hat{\phi}\sin\theta_j\,, \qquad y_2 = \hat{\theta}\,.$$

Since $\Delta_s\psi = \psi_{y_1y_1} + \psi_{y_2y_2} + \mathcal{O}(\varepsilon)$ and $u_{qe}v_{qe} \simeq u_jv_j$, as obtained from (2.15), (3.1) on $y \in \mathbb{R}^2$ becomes

$$\begin{aligned} &\psi_{j_{y_1y_1}} + \psi_{j_{y_2y_2}} - \psi_j + 2fu_jv_j\psi_j + f\mathcal{D}u_j^2\eta_j + \mathcal{O}(\varepsilon) = \lambda\psi_j\,,\\ &\mathcal{D}(\eta_{j_{y_1y_1}} + \eta_{j_{y_2y_2}}) + \psi_j - 2u_jv_j\psi_j - \mathcal{D}u_j^2\eta + \mathcal{O}(\varepsilon) = \tau\lambda\eta_j\varepsilon^2\,. \end{aligned} \tag{3.2}$$

We neglect the $\mathcal{O}(\varepsilon)$ term, define $N_j \equiv \mathcal{D}\eta_j$, and assume that $\tau\lambda \ll \mathcal{O}(\varepsilon^{-2})$. Then, from (3.2) we obtain the limiting problem

$$\psi_{j_{y_1y_1}} + \psi_{j_{y_2y_2}} - \psi_j + 2fu_jv_j\psi_j + fu_j^2N_j = \lambda\psi_j\,, \qquad N_{j_{y_1y_1}} + N_{j_{y_2y_2}} + \psi_j - 2u_jv_j\psi_j - u_j^2N_j = 0\,, \tag{3.3}$$

on $-\infty < y_1, y_2 < \infty$. In (3.3), u_j and v_j are the radially symmetric solutions to the core problem (2.3), and they depend on S_j and f. Finally, we note that due to the $-\psi_j$ term in the ψ_j equation of (3.2), it is consistent to impose that $\psi_j \to 0$ as $y_1^2 + y_2^2 \to \infty$, provided that $\mathrm{Re}\lambda > -1$.

We seek a separation of variable solution of (3.3) of the form

$$\psi_j = \hat{\psi}_j(\rho)e^{i\omega m}, \qquad N_j = \hat{N}_j(\rho)e^{iwm},$$

where $(y_1, y_2) = \rho(\cos\omega, \sin\omega)$, and $m = 0, 1, 2, \ldots$. From (3.3), we obtain on $0 < \rho < \infty$ that

$$\Delta_\rho\hat{\psi}_j - \frac{m^2}{\rho^2}\hat{\psi}_j - (1+\lambda)\hat{\psi}_j + 2fu_jv_j\hat{\psi}_j + fu_j^2\hat{N}_j = 0\,, \qquad \Delta_\rho\hat{N}_j - \frac{m^2}{\rho^2}\hat{N}_j + \hat{\psi}_j - 2u_jv_j\hat{\psi}_j - u_j^2\hat{N}_j = 0\,, \tag{3.4}$$

with $\hat{\psi}_j'(0) = \hat{N}_j'(0) = 0$ and $\hat{\psi}_j \to 0$ as $\rho \to \infty$. The appropriate asymptotic boundary condition for $\hat{N}_j$ will depend on the range of m, and is discussed below. Finally, we need only consider the modes $m = 0, 2, 3, 4, \ldots$, since $m = 1$ corresponds to the translation mode associated with the neutral eigenvalue $\lambda = 0$.

3.1 Case I: Non-Radially Symmetric Local Perturbations ($m = 2, 3, \ldots$)

We now look for solutions to (3.4) with $m = 2, 3, \ldots$ corresponding to non-radially symmetric perturbations near the j-th spot. Due to the non-vanishing $-m^2\hat{N}_j/\rho^2$ term in the $\hat{N}_j$ equation of (3.4), we can impose an algebraic decay as $\hat{N}_j \to \infty$ as $\rho \to \infty$ for (3.4). This implies that the non-radially symmetric eigenfunctions are largely local instabilities, and the coupling arises only through the nonlinear algebraic system (2.14 *a*) for $S_1, \ldots, S_N$.

The numerical method to solve (3.4) when $m \geq 2$ is as follows. For a specific value of f, we compute u_j and v_j from the core problem (2.3), and discretize (3.4) with 400 meshpoints using centered differences on $0 < \rho < 15$. The eigenvalue λ of (3.4) with the largest real part is computed from the resulting generalized matrix eigenvalue problem. Our numerical results show that this principal eigenvalue is real.

In the left panel of Fig. 4 we plot the principal eigenvalue as a function of S_j for modes $m = 2, 3, 4$ for the specific choice $f = 0.7$. Qualitatively similar results are obtained for different values of f. In the right panel of Fig. 4 we plot two curves $\Sigma_m(f)$ versus f corresponding to the critical values of S_j where $\lambda = 0$ for the $m = 2$ mode and the $m = 3$ mode. Our numerical results show that, for each f, the $m = 2$ mode is the first mode to go unstable as S_j is increased. Therefore, if $S_j > \Sigma_2(f)$, the spot will be unstable to a mode $m = 2$ linear instability. This linear instability is of peanut-splitting type and is found in full numerical computations to initiate a nonlinear spot self-replication event.

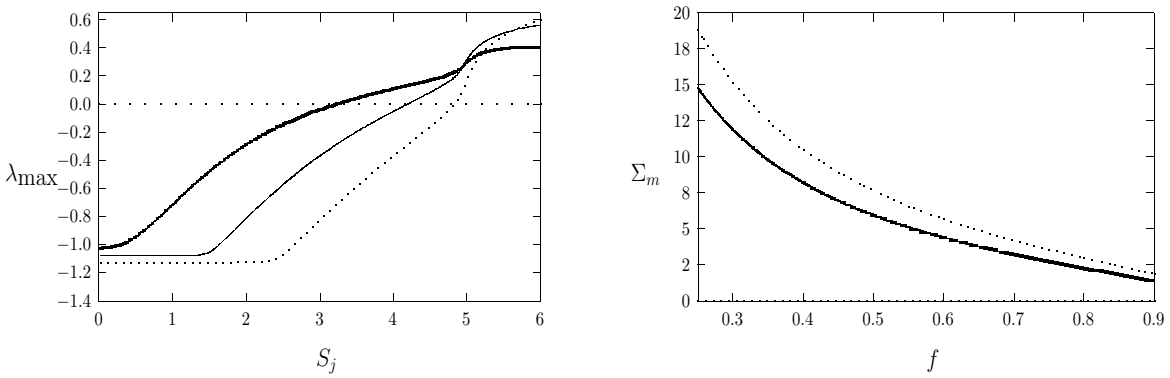

FIGURE 4. Left panel: plot of the principal eigenvalue $\lambda_{\max}$ of (3.4) as a function of S_j when $f = 0.7$ for $m = 2$ (heavy solid curve), $m = 3$ (solid curve), and $m = 4$ (dotted curve). Right panel: plot of the threshold $S_j \equiv \Sigma_m$ versus f corresponding to the threshold condition $\lambda = 0$ for $m = 2$ (heavy solid curve) and $m = 3$ (dotted curve). For $f = 0.7$, the peanut-splitting ($m = 2$) threshold occurs first as S_j is increased. Qualitatively similar results are obtained for other values of f.

To illustrate this phenomena, in Fig. 5 we show a spot self-replication event as computed from the full PDE system (1.2) for a one-spot initial condition for the parameter values $f = 0.7$, $\mathcal{D} = 0.75$, $\tau = 1/(0.7)^2$, and $\varepsilon = 0.1$. The initial condition was taken to have the form in (2.15) of Principal Result 2.1. This experiment suggests that the peanut-splitting instability is subcritical and leads to a nonlinear spot self-replication event. In our computations, we took $\mathrm{E} = 1.3$ for $0 \leq t \leq 5$. At $t = 5$, when the initial transient has died out, a 2% random perturbation was given to the numerical solution and E was then allowed to increase slowly as $\mathrm{E} = \min(1.3 + 0.01(t-5), 1.6)$ for $t \geq 5$. For $f = 0.7$, we have $\Sigma_2 \approx 3.23$ from the right panel of Fig. 4. At $t = 0$, where $\mathrm{E} = 1.3$, we have $S = 2(1.3)/\sqrt{0.75} \approx 3.0 < \Sigma_2$, and $S \approx 3.7 > \Sigma_2$ when $\mathrm{E} = 1.6$. When $\mathrm{E} = 1.6$, we obtain from the data used to generate the left panel of Fig. 4 that the growth rate for the peanut-splitting mode is $\lambda \approx 0.055$. This small growth rate for the unstable peanut-splitting mode at $E = 1.6$ is likely the the principal reason why the spot in Fig. 5 takes a rather long time to split.

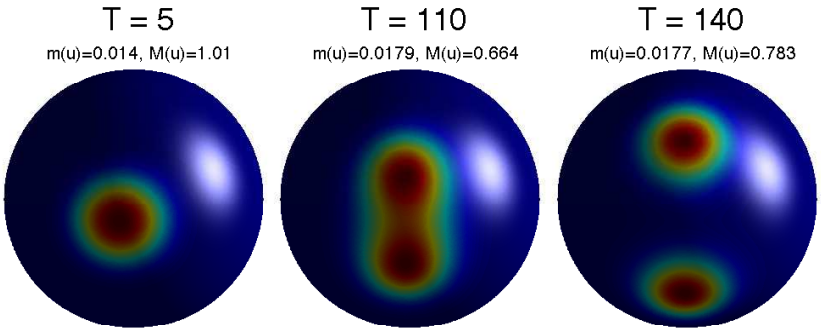

FIGURE 5. Full numerical simulation of (1.2) on the unit sphere illustrating a spot self-replication instability for a one-spot pattern. The parameter values are $f = 0.7$, $\mathcal{D} = 0.75$, $\tau = 1/(0.7)^2$, and $\varepsilon = 0.1$. We take E = 1.3 for $t \le 5$. At $t = 5$ a 2% random perturbation is given to the solution and E is increased slowly in time as $\mathrm{E} = \min(1.3 + 0.01(t-5), 1.6)$ for $t \ge 5$. Here $m(u)$ and $M(u)$ are the min and max of u on the sphere.

3.2 Case II: Radially Symmetric Local Perturbations ($m = 0$)

The case $m = 0$ corresponds to a locally radially symmetric perturbation near the j-th spot. The key difference, as compared with the $m \ge 2$ case, is that without the $-m^2 N_j/\rho^2$ term in (3.4), we cannot impose that $N_j \to 0$ as $\rho \to \infty$. Instead, we must allow for logarithmic growth in the far-field for N_j. Therefore, for (3.4), we impose the far-field behaviour $N_j \sim c_j \log\rho$ as $\rho \to \infty$. The constants c_j for $j = 1, \ldots, N$ will be determined later from a global matrix problem that effectively couples all of the local problems near the spots.

Since (3.3) is linear and homogeneous, we can write

$$\psi = c_j \tilde{\psi}_j(\rho), \qquad N = c_j \tilde{N}_j(\rho),$$

so that, on $0 < \rho < \infty$, (3.4) becomes

$$\begin{aligned} &\Delta_\rho \tilde{\psi}_j - (1+\lambda)\tilde{\psi}_j + 2f u_j v_j \tilde{\psi}_j + f u_j^2 \tilde{N}_j = 0\,, \qquad \Delta_\rho \tilde{N}_j + \tilde{\psi}_j - 2u_j v_j \tilde{\psi}_j - u_j^2 \tilde{N}_j = 0\,, \\ &\tilde{\psi}_j'(0) = \tilde{N}_j'(0) = 0\,; \qquad \tilde{\psi}_j \to 0 \quad \text{and} \quad \tilde{N}_j \to \log\rho + \tilde{B}_j + o(1) \quad \text{as} \quad \rho \to \infty\,, \end{aligned} \tag{3.5}$$

where the term $\tilde{B}_j = \tilde{B}_j(\lambda; S_j, f)$ must be computed numerically. Upon integrating the $\tilde{N}_j$ equation in (3.5) over $0 < \rho < \infty$, and using $\tilde{\psi}_j = \psi_j/c_j$ and $\tilde{N}_j = N_j/c_j$, we obtain an identity for c_j,

$$c_j = -\int_0^\infty \left(\psi_j(1 - 2u_j v_j) - u_j^2 N_j\right) \rho\, d\rho\,. \tag{3.6}$$

We remark that since $\tilde{N}_j$ does not tend to zero at infinity, the local problems near each spot are all coupled together through some outer problem for η that has singularities at $x = x_j$ for $j = 1, \ldots, N$. This is in contrast to the $m \ge 2$ case for non-radially symmetric perturbations studied earlier, which are (largely) local instabilities. To obtain the matching condition for this outer problem for η, we need the far-field behavior of the inner solution near the j-th spot. Since $\eta_j = N_j/\mathcal{D} = c_j \tilde{N}_j/\mathcal{D}$ and $\tilde{N}_j \sim \log\rho + \tilde{B}_j + o(1)$ as $\rho \to \infty$ from (3.5), the asymptotic matching condition,

written in terms of the outer x variable, is that the outer solution for η must satisfy

$$\eta_j \sim \frac{c_j}{\mathcal{D}}\left[\log|x-x_j| + \frac{1}{\nu} + \tilde{B}_j\right] \quad \text{as} \quad x \to x_j\,, \quad j=1,\dots,N\,; \qquad \text{where} \quad \nu \equiv -1/\log\varepsilon\,. \tag{3.7}$$

In the outer region, we obtain from the ψ equation in (3.1) that the outer solution for ψ satisfies $\psi_{out}(-1+2fu_ev_e) + fu_e^2\eta_{out} = \lambda_{out}\psi_{out}$. Since $u_e = \mathcal{O}(\varepsilon^2)$, $v_e = \mathcal{O}(1)$ and $\eta_{out} = \mathcal{O}(1)$ in the outer region, we obtain that $\psi_{out} = \mathcal{O}(\varepsilon^4) \ll 1$. Similarly, from the η equation in (3.1), the outer approximation for η satisfies

$$\mathcal{D}\Delta_s\eta + \frac{1}{\varepsilon^2}\left(\psi + 2u_ev_e\psi - u_e^2\eta\right) = \tau\lambda\eta\,. \tag{3.8}$$

To estimate the coefficient of ε^{-2} in (3.8) in the outer region we use $u_e = \mathcal{O}(\varepsilon^2)$, $v_e = \mathcal{O}(1)$, $\eta_{out} = \mathcal{O}(1)$, and $\psi_{out} = \mathcal{O}(\varepsilon^4) \ll 1$, to estimate $\varepsilon^{-2}(-u_e^2\eta_{out}) = \mathcal{O}(\varepsilon^2\eta)$ and $\varepsilon^{-2}\left(\psi + 2u_ev_e\psi\right) = \varepsilon^{-2}\left(\mathcal{O}(\varepsilon^4) - \mathcal{O}(\varepsilon^2 v_e\psi_{out})\right) = \mathcal{O}(\varepsilon^2) + \mathcal{O}(\varepsilon^4)$. Therefore, both of these terms are negligible in the outer region.

This estimate shows that the global contribution from the non-trivial background state of u_e is negligible with regards to its effect on the outer solution for η. As such, we need only consider the local contributions near each spot. In the sense of distributions, we use (3.6) to calculate this local contribution near the j-th spot as

$$\frac{1}{\varepsilon^2}\left(\psi + 2u_ev_e\psi - u_e^2\eta\right) \to 2\pi\sum_{j=1}^{N}\left(\int_0^\infty\left(\psi_j(1-2u_jv_j) - u_j^2\eta_j\right)\rho\,d\rho\right)\delta(x-x_j) = -2\pi\sum_{j=1}^{N}c_j\delta(x-x_j)\,.$$

In this way, we obtain from (3.7) and (3.8) that the outer solution for η satisfies

$$\Delta_s\eta - \frac{\tau\lambda}{\mathcal{D}}\eta = \frac{2\pi}{\mathcal{D}}\sum_{j=1}^{N}c_j\delta(x-x_j)\,, \quad x\in\Omega\,; \qquad \eta \sim \frac{c_j}{\mathcal{D}}\left(\log|x-x_j| + \frac{1}{\nu} + \tilde{B}_j\right) \quad \text{as } x\to x_j\,, \quad j=1,\dots,N\,. \tag{3.9}$$

In the next two subsections we consider two separate cases for (3.9). For $\tau > 0$ and $\lambda \neq 0$, the solution to (3.9) involves the reduced-wave Green's function, which is given explicitly in terms of Legendre functions. However, for the case $\tau = 0$, or for the problem of calculating stability thresholds resulting from eigenvalues entering $\mathrm{Re}(\lambda) > 0$ through the origin $\lambda = 0$, the source-neutral Green's function is used to solve (3.9). Either case leads to a linear algebraic system of the form

$$\mathcal{M}\mathbf{c} = \mathbf{0}, \qquad \text{where} \qquad \mathcal{M} = \mathcal{M}(S_1,\dots,S_N,\lambda,f,\mathcal{D})\,.$$

The condition for the existence of a non-trivial solution for $\mathbf{c} = (c_1,\dots,c_N)^T$ is that

$$\det\mathcal{M} = 0\,.$$

This condition effectively leads to a transcendental equation for any discrete eigenvalues λ of the linearized problem that correspond to locally radially symmetric perturbations near each spot.

Before calculating $\mathcal{M}$, we derive a key identity needed in §3.3 for obtaining stability thresholds that result from eigenvalues crossing through the origin $\lambda = 0$. If we differentiate the core problem (2.3) with respect to S_j, and compare the resulting problem with (3.5), we conclude at $\lambda = 0$ that

$$\tilde{B}_j(\lambda = 0; S_j, f) = \partial_{s_j}\chi(S_j;f) \equiv \chi'(S_j;f)\,. \tag{3.10}$$

3.3 Case A: Locally Radially Symmetric Perturbations: Zero Eigenvalue Crossings

In this subsection we consider the case where $\tau\lambda/\mathcal{D} = 0$ in (3.9). For $\tau > 0$, this occurs when we look for stability thresholds corresponding to zero eigenvalue crossings. It also occurs for the case where $\tau = 0$ for all λ. Although this

latter case is not directly relevant to the Brusselator model where $\tau = 1/f^2$, we will still consider the possibility of this distinguished limit below.

When $\tau\lambda/\mathcal{D} = 0$ in (3.9), the solution is given in terms of the source-neutral Green's function of (2.8) and (2.9) as

$$\eta = -\frac{2\pi}{\mathcal{D}}\sum_{j=1}^{N} c_j G(x;x_j) + \frac{\bar{\eta}}{\mathcal{D}}\,, \tag{3.11}$$

where $\bar{\eta}$ is a constant to be found. From the divergence theorem we get $\sum_{j=1}^{N} c_j = 0$. We then let $x \to x_i$ in (3.11) and compare the resulting expression with the required matching condition (3.7). This yields a linear system of the form

$$-2\pi\nu\left(c_i R + \sum_{j\neq i}^{N} c_j G_{ij}\right) + \nu\bar{\eta} = c_i\left(1+\nu\tilde{B}_i\right)\,, \qquad i = 1,\ldots,N\,.$$

We then set $G_{ij} = -L_{ij}/(2\pi)+R$, where $L_{ij} \equiv \log|x_i - x_j|$ and $R \equiv (\log 4 - 1)/(4\pi)$, and use the condition $\sum_{j=1}^{N} c_j = 0$ to write this linear system in matrix form as

$$\nu\mathcal{G}\mathbf{c} + \nu\bar{\eta}\mathbf{e} = \mathbf{c} + \nu\mathcal{B}\mathbf{c}\,, \qquad \mathbf{e}^T\mathbf{c} = 0\,, \tag{3.12}$$

for the $N+1$ unknowns $\bar{\eta}$ and c_j for $j = 1,\ldots,N$. Here we have defined $\mathcal{B}$, $\mathbf{e}$, $\mathbf{c}$, and $\mathcal{G}$, as

$$\mathcal{B} \equiv \begin{pmatrix} \tilde{B}_1 & & 0 \\ & \ddots & \\ 0 & & \tilde{B}_N \end{pmatrix}\,, \qquad \mathbf{e} \equiv \begin{pmatrix} 1 \\ \vdots \\ 1 \end{pmatrix}\,, \qquad \mathbf{c} \equiv \begin{pmatrix} c_1 \\ \vdots \\ c_N \end{pmatrix}\,, \qquad \mathcal{G} \equiv \begin{pmatrix} 0 & L_{12} & \cdots & L_{1N} \\ L_{21} & \ddots & & \vdots \\ \vdots & & & \\ L_{N1} & \cdots & & 0 \end{pmatrix}\,. \tag{3.13}$$

Upon pre-multiplying (3.12) by $\mathbf{e}^T$, we obtain $\bar{\eta} = \left(\mathbf{e}^T\mathcal{B}\mathbf{c} - \mathbf{e}^T\mathcal{G}\mathbf{c}\right)/N$. Upon re-substituting $\bar{\eta}$ into (3.12) we get

$$\nu\mathcal{G}\mathbf{c} + \nu\mathcal{E}_0\left(\mathcal{B}-\mathcal{G}\right)\mathbf{c} = \mathbf{c} + \nu\mathcal{B}\mathbf{c}\,, \qquad \text{where} \qquad \mathcal{E}_0 \equiv \frac{1}{N}\mathbf{e}\mathbf{e}^T = \frac{1}{N}\begin{pmatrix} 1 & \cdots & 1 \\ \vdots & & \vdots \\ 1 & \cdots & 1 \end{pmatrix}\,.$$

From a simple re-arrangement of this system, we obtain the following result:

Principal Result 3.1 *Let $\varepsilon \to 0$ and $\tau = 0$. Then, with respect to locally radially symmetric perturbations near each spot, the stability of the quasi-equilibrium solution of Principal Result 2.1 is determined by the roots λ of*

$$\det\mathcal{M} = 0\,, \qquad \textit{where} \qquad \mathcal{M} \equiv \left(\frac{1}{\nu}I + (I-\mathcal{E}_0)(\mathcal{B}-\mathcal{G})\right)\,. \tag{3.14}$$

The solution of $\det\mathcal{M} = 0$, which yields the discrete eigenvalues λ of the linearization for the case $\tau = 0$, requires the determination of $\tilde{B}_j = \tilde{B}_j(\lambda; S_j, f)$ as defined in (3.5). Moreover, for $\tau \geq 0$, the zero eigenvalue crossings occur at parameter values for which $\det\mathcal{M} = 0$, where $\mathcal{B} = diag(\chi'(S_j;f))$. In (3.14), the source strengths $S_1,\ldots,S_N$ must be determined from the nonlinear algebraic system (2.14 a). When $\det\mathcal{M} = 0$ the spatial mode for the onset of the instability of the spot amplitudes is determined by the eigenvector $\mathbf{c}$ of $\mathcal{M}\mathbf{c} = \mathbf{0}$. We refer to (3.14) as the globally coupled eigenvalue problem (GCEP) for $\tau = 0$.

The identity (3.10) is critical for easily calculating the stability threshold for any eigenvalue entering $\mathrm{Re}(\lambda) > 0$ through the origin $\lambda = 0$. More specifically, since $\mathcal{B} = \mathrm{diag}(\chi'(S_j;f))$ at $\lambda = 0$, we need only provide a numerical estimation of $\chi'(S_j;f)$ to determine $\mathcal{B}$. The stability threshold in terms of parameters in the Brusselator model for zero eigenvalue crossings is then obtained by simply solving $\det\mathcal{M} = 0$ together with (2.14 *a*) for the source strengths.

For the special case where the spots have a common source strength, i.e., $S_c \equiv S_1 = \ldots = S_N$, we now show that the stability threshold is determined in terms of the roots of $N-1$ scalar nonlinear algebraic equations. A quasi-equilibrium pattern having a common source strength will occur whenever the matrix $\mathcal{G}$ has a constant row sum, so that $\mathbf{e} = (1, \ldots, 1)^T$ is an eigenvector of $\mathcal{G}$, i.e. $\mathcal{G}\mathbf{e} = \kappa_1 \mathbf{e}$. In particular, such a constant row sum matrix structure will always occur for a two-spot pattern with arbitrarily located spots, since $\mathcal{G}$ is a symmetric matrix with zero diagonal entries. It also occurs for other symmetric arrangements of spots, such as when spots are located at the vertices of any of the 5 platonic solids, or when N equally-spaced spots lie on a ring of constant latitude on the sphere. For this latter arrangement, the matrix $\mathcal{G}$ is circulant. The constant row sum property of $\mathcal{G}$ also holds in an approximate sense when the spot locations are at the elliptic Fekete points, i.e. at the spot configuration that minimizes the interaction energy $-\sum_{i=1}^{N}\sum_{\substack{j=1\\ j\neq i}}^{N} \log|x_i - x_j|$. Such "symmetric" spot arrangements are discussed in detail in §5.

Assuming that $\mathcal{G}$ has a constant row sum, there is a solution to (2.14 *a*) of the form $\mathbf{S} = S_c\mathbf{e}$. For this solution, we get from (2.14 *a*) that $S_c = 2\mathrm{E}/\sqrt{\mathcal{D}}N$. The corresponding matrix $\mathcal{M}$ is simply

$$\mathcal{M} = \frac{1}{\nu} I + \chi'(S_c; f)(I - \mathcal{E}_0) - (I - \mathcal{E}_0)\mathcal{G}\,.$$

Since $\mathcal{G}$ has a constant row sum and is symmetric, the matrix eigenvalue problem $\mathcal{G}\mathbf{b} = k\mathbf{b}$ has eigenpairs

$$\mathcal{G}\mathbf{e} = k_1\mathbf{e}\,; \qquad \mathcal{G}\mathbf{b_j} = k_j\mathbf{b_j}\,, \quad \text{with} \quad \mathbf{b_j}^T\mathbf{e} = 0\,, \quad \text{for} \quad j = 2, \ldots, N\,, \qquad \mathbf{b_j}^T\mathbf{b_k} = 0\,, \quad j \neq k\,. \tag{3.15}$$

Our main result for the stability threshold corresponding to zero eigenvalue crossings is as follows:

Principal Result 3.2 *Suppose that $S_c \equiv S_1 = \ldots = S_N$. Then, for radially symmetric perturbations near each spot, the stability threshold $\lambda = 0$ occurs when*

$$\frac{1}{\nu} + \chi'(S_c; f) - k_j = 0\,, \qquad j = 2, \ldots, N\,; \qquad S_c = \frac{2\mathrm{E}}{\sqrt{\mathcal{D}}N}\,, \tag{3.16}$$

where k_j for $j = 2, \ldots, N$ are any of the eigenvalues of $\mathcal{G}$ corresponding to the $N-1$ dimensional subspace perpendicular to $\mathbf{e}$, i.e. $\mathcal{G}\mathbf{b_j} = k_j\mathbf{b_j}$ with $\mathbf{b_j}^T\mathbf{e} = 0$ for $j = 2, \ldots, N$. These zero eigenvalue crossings occur at the bifurcation points where the Jacobian of the nonlinear algebraic system (2.14 a) for the source strengths is non-invertible.

Proof Suppose that $\mathbf{S} = S_c\mathbf{e}$ and that $\lambda = 0$. Then, we show that the eigenvectors $\mathbf{e}$ and $\mathbf{b_j}$, for $j = 2, \ldots, N$, of $\mathcal{G}$ are also eigenvectors of $\mathcal{M}$. Since $\mathcal{E}_0\mathbf{b_j} = 0$ and $\mathcal{G}\mathbf{b_j} = k_j\mathbf{b_j}$ for $j = 2, \ldots, N$, we calculate that

$$\mathcal{M}\mathbf{b_j} = \frac{1}{\nu}\mathbf{b_j} + \chi'(S_c; f)(I - \mathcal{E}_0)\mathbf{b_j} - (I - \mathcal{E}_0)\mathcal{G}\mathbf{b_j} = \left(\frac{1}{\nu} + \chi'(S_c; f) - k_j\right)\mathbf{b_j}\,.$$

In addition, since $(I - \mathcal{E}_0)\mathbf{e} = 0$, and $\mathcal{G}\mathbf{e} = k_1\mathbf{e}$, the other eigenvector of $\mathcal{M}$ is

$$\mathcal{M}\mathbf{e} = \frac{1}{\nu}\mathbf{e} + \chi'(S_c; f)(I - \mathcal{E}_0)\mathbf{e} - (I - \mathcal{E}_0)\mathcal{G}\mathbf{e} = \frac{1}{\nu}\mathbf{e}\,.$$

Thus, the eigenvalues μ_j of $\mathcal{M}$ are $\mu_1 = 1/\nu$ and $\mu_j = \left(\frac{1}{\nu} + \chi'(S_c; f) - k_j\right)$ for $j = 2, \ldots, N$. The first eigenvalue μ_1 is non-vanishing, implying that there are no zero eigenvalue crossings for the synchronous instability mode. In contrast, setting $\mu_j = 0$ for $j = 2, \ldots, N$ yields (3.16) for the competition modes. Finally, the Jacobian $\mathcal{J}$ of the nonlinear algebraic system in (2.14 *a*) associated with the linearization around the common source strength solution $S_c \equiv S_1 = \ldots S_N$ is $\mathcal{J} \equiv I - \nu\,(I - \mathcal{E}_0)\,\mathcal{G} + \nu\chi'(S_c; f)(I - \mathcal{E}_0)$. The eigenpairs of $\mathcal{J}$ are $\mathcal{J}\mathbf{e} = \mathbf{e}$ and $\mathcal{J}\mathbf{b_j} = (1 - \nu k_j + \nu\chi'(S_c; f))\mathbf{b_j}$ where $\mathbf{b_j}^T\mathbf{e} = 0$ for $j = 2, \ldots, N$. Therefore, $\mathcal{J}$ is not invertible at the roots of (3.16). □

These roots of (3.16) correspond to values of $\mathcal{D}$ where asymmetric quasi-equilibrium patterns, characterized by spots with different source strengths, bifurcate from the common source strength solution branch. For such asymmetric spot patterns the spot amplitudes are different for each spot. A leading-order theory to construct these asymmetric branches for the regime $\mathcal{D} = \mathcal{O}(\nu^{-1})$ is discussed at the end of §4.1.

For the competition instability modes, the perturbation ψ of the quasi-equilibrium solution for u near the j-th spot has the form $\psi = c_j\tilde{\psi}_j(\rho)$, where $\mathbf{c} = (c_1, \ldots, c_N)^T$ satisfies $\mathbf{c}^T\mathbf{e} = 0$. In this sense, a competition instability mode represents a sign-fluctuating perturbation of the spot amplitudes.

Next, we show that (3.16) must have a solution for any $\varepsilon \ll 1$ fixed as $\mathcal{D}$ is increased. Our numerical results in the right panel of Fig. 3 indicate that $\chi'(S_c; f) < 0$ with $\chi'(S_c; f) \to -\infty$ as $S_c \to 0^+$ and $\chi''(S_c; f) > 0$ when S_c is sufficiently small. Explicit asymptotic results for $\chi(S_c; f)$ are given below in (4.20) of §4.1 to analytically confirm these numerical results. We then define $\sigma_j \equiv \frac{1}{\nu} + \chi'(S_c; f) - k_j$, with $\nu = -1/\log\varepsilon$. For $\mathcal{D} = \mathcal{O}(1)$, and for any $\nu \ll 1$ fixed, we have $\sigma_j > 0$ for all $j = 2, \ldots, N$. However, as $\mathcal{D} \to \infty$, $S_c = 2\mathrm{E}/\sqrt{\mathcal{D}}N \to 0^+$, and thus $\chi'(S_c; f) \to -\infty$. Therefore, for $\mathcal{D}$ large enough with ν small and fixed, the first crossing of $\sigma_j = 0$ in the set $j = \{2, \ldots, N\}$ will occur for the maximum eigenvalue $k_{j^\star} \equiv \max_{2\le j\le N}\{k_j\}$. The uniqueness of this root for $S_c \ll 1$ follows from $\chi''(S_c; f) > 0$.

Corollary 3.1 *Under the conditions of Principal Result 3.2, as $\mathcal{D}$ is increased the smallest value of $\mathcal{D}$ for which $\lambda = 0$ is given by the root of the transcendental equation*

$$\frac{1}{\nu} - k_{j^\star} = -\chi'(S_c; f)\,, \qquad \text{where} \quad S_c = \frac{2\mathrm{E}}{\sqrt{\mathcal{D}}N}\,. \tag{3.17}$$

Here $k_{j^\star} \equiv \max_{2\le j\le N} k_j$ with $\mathcal{G}\mathbf{b_j} = k_j\mathbf{b_j}$, with $\mathbf{b_j}^T\mathbf{e} = 0$. This criterion defines a competition instability threshold $S_c^\star \equiv S_c^\star(f, N)$, or equivalently a threshold $\mathcal{D}_c^\star \equiv \mathcal{D}_c^\star(f, N)$ of the diffusivity $\mathcal{D}$.

The competition instability threshold can be written in terms of the ratio $\mathcal{D}/\mathrm{E}^2$. Since S_c decreases as the number of spots N increases, this instability will also occur when there are too many spots. Therefore, the competition instability can be interpreted as an over-crowding instability.

Remark 3.1 *The result (3.17) determines the smallest value $\mathcal{D}_c^\star$ of $\mathcal{D}$ for which $\lambda = 0$ is an eigenvalue when $\tau \ge 0$ corresponding to locally radially symmetric perturbations near each spot. Since multi-spot patterns are well-known to be unstable in the near shadow limit when $\mathcal{D} \gg 1$ (see [**48**]), we conjecture that a multi-spot pattern is stable to a competition instability when $\mathcal{D} < \mathcal{D}_c^\star$ and is unstable when $\mathcal{D} > \mathcal{D}_c^\star$.*

The key quantity determining the competition instability threshold for the equal source strength case is the largest eigenvalue of $\mathcal{G}$ in the subspace perpendicular to $\mathbf{e}$. For two spots, the two eigenvalues of $\mathcal{G}$ can be calculated analytically. In Fig. 6 we plot the numerically computed competition instability threshold $\mathcal{D}/\mathrm{E}^2$ for two spots with a common spot-strength S_c. In the left panel, where the two spots are at antipodal points on the sphere, we plot the threshold versus f for three values of ε. In the right panel, we plot the threshold for two spots at varying distances from each other, for fixed values of f and for $\varepsilon = 0.025$. These results show that the competition instability threshold for $\mathcal{D}/\mathrm{E}^2$ decreases as the distance between the spots decreases, confirming the over-crowding nature of the instability. For parameter values above any of the curves in these figures, we predict that a competition instability will occur.

We summarize our stability results so far as follows: Suppose that the spot locations are such that $\mathcal{G}\mathbf{e} = k_1\mathbf{e}$, so

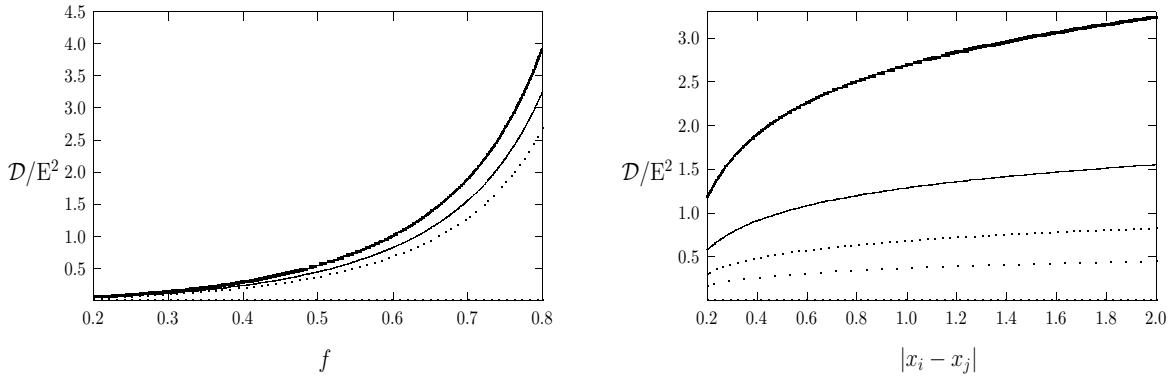

FIGURE 6. Left panel: the competition stability threshold $\mathcal{D}/\mathrm{E}^2$ versus f for two spots located at antipodal points on the sphere for $\varepsilon = 0.01$ (heavy solid curve), $\varepsilon = 0.025$ (solid curve) and $\varepsilon = 0.05$ (dotted curve). Right panel: the competition stability threshold as a function of the distance between two spots when $\varepsilon = 0.025$ for $f = 0.8$ (heavy solid curve), $f = 0.7$ (solid curve), $f = 0.6$ (dotted curve), and $f = 0.5$ (widely spaced dots).

that the nonlinear algebraic system (2.14 *a*) admits a solution with a common source strength $S_c \equiv S_1 = \ldots = S_N$. Then, if $S_c > \Sigma_2(f)$, which corresponds to $\mathcal{D}/\mathrm{E}^2$ below a threshold, the quasi-equilibrium solution is unstable to a local mode peanut-splitting instability near each spot. Here Σ_2 is the critical value of S_c where $\lambda = 0$ for the locally non-radially symmetric $m = 2$ mode (see the right panel of Fig. 4). Numerical evidence suggests that this instability is subcritical and leads to a spot self-replication event. Alternatively, if $S_c < S_c^\star(f; N)$ and $N \geq 2$, which corresponds to $\mathcal{D}/\mathrm{E}^2$ above a threshold, we predict that the quasi-equilibrium solution is linearly unstable as a result of an unstable eigenvalue associated with locally radially symmetric perturbations near each spot. The global eigenfunction is of sign-fluctuating type in that the sum of the perturbations of the spot amplitudes vanishes. Numerical evidence suggests that a competition instability is the trigger of a spot annihilation event.

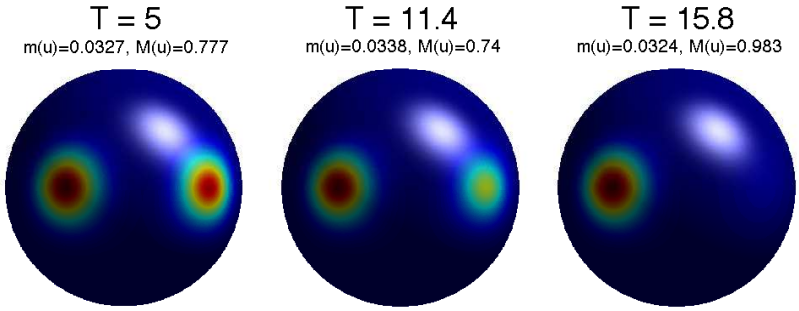

FIGURE 7. Full numerical simulation of (1.2) on the unit sphere for $f = 0.5$, $\mathrm{E} = 3$, $\tau = 1/(0.5)^2$, and $\varepsilon = 0.1$, showing a competition instability for a two-spot pattern with initial spots at $(1, 0, 0$ and $(0, 1, 0)$. We take $\mathcal{D} = 1.6$ for $t \leq 5$. At $t = 5$ a 2% random perturbation is given to the solution and $\mathcal{D}$ is increased slowly in time as $\mathcal{D} = \min(1.6 + 0.01(t - 5), 3)$ for $t \geq 5$. The competition instability threshold from (3.17) is $\mathcal{D}_c^\star \approx 1.8$. Here $m(u)$ and $M(u)$ are the min and max of u on the sphere.

In the full numerical computations of the Brusselator (1.2) shown in Fig. 7 we exhibit a competition instability that occurs for a two-spot pattern when $\mathcal{D}$ is large enough. The details of the experiment, and the parameter values used, are given in the caption of this figure. The competition instability threshold, as computed from (3.17), is $\mathcal{D}_c^\star \approx 1.8$.

3.4 Case B: Locally Radially Symmetric Perturbations For $\tau > 0$

For $\tau\lambda \neq 0$, the solution to (3.9) is

$$\eta = -\frac{2\pi}{\mathcal{D}} \sum_{j=1}^{N} c_j G_\lambda(x; x_j)\,, \tag{3.18}$$

where $G_\lambda(x; x_0)$ is the reduced-wave Green's function on the unit sphere, satisfying

$$\Delta_s G_\lambda - \frac{\tau\lambda}{\mathcal{D}} G_\lambda = -\delta(x - x_0)\,, \quad x \in \Omega\,; \qquad G_\lambda(x; x_0) \sim -\frac{1}{2\pi}\log|x - x_0| + R_\lambda + o(1) \quad \text{as} \quad x \to x_0\,. \tag{3.19}$$

Here G_λ is 2π periodic in ϕ and smooth at $\theta = 0, \pi$, and the regular part R_λ of the G_λ is independent of x_0.

The explicit solution to (3.19) can be obtained in terms of the well-known Green's function $G_h(x; x_0)$ to

$$\Delta_s G_h + \sigma(\sigma + 1) G_h = -\delta(x - x_0)\,. \tag{3.20}$$

When σ is not a non-negative integer, the explicit solution to (3.20) is (cf. [**36**],[**37**],[**11**])

$$G_h(x; x_0) = -\frac{1}{4\sin(\pi\sigma)} P_\sigma(-x \cdot x_0)\,, \tag{3.21}$$

where $P_\sigma(z)$ is the Legendre function of the first kind of complex order σ. The limiting behavior as $z \to -1$, corresponding to $x \to x_0$, is (cf. [**11**])

$$P_\sigma(z) \sim \frac{\sin(\pi\sigma)}{\pi}\left[\log\left(\frac{1+z}{2}\right) + 2\gamma + 2\Phi(\sigma+1) + \pi\cot(\pi\sigma)\right] \quad \text{as} \quad z \to -1\,,$$

where γ is Euler's constant and $\Phi(z) = \Gamma'(z)/\Gamma(z)$ is the Psi or digamma function and $\Gamma(z)$ is the gamma function. Therefore, as $x \to x_0$, we have

$$G_h(x; x_0) \sim -\frac{1}{2\pi}\log|x - x_0| + R_h\,, \qquad R_h = R_h(\sigma) \equiv \frac{1}{4\pi}\left[\log 4 - 2\gamma - 2\Phi(\sigma+1) - \pi\cot(\pi\sigma)\right]\,. \tag{3.22}$$

Upon comparing (3.20) with (3.19), we identify $\sigma(\sigma+1) = -\tau\lambda/D$, so that

$$\sigma = \sigma(\lambda) \equiv -\frac{1}{2} + \frac{i}{2}\sqrt{\frac{4\lambda\tau}{\mathcal{D}} - 1}\,. \tag{3.23}$$

Here we have chosen the branch of the square root for which $\sqrt{z-1} = |z-1|^{1/2} e^{i\arg(z-1)/2}$ with $-\pi/2 < \arg(z-1) < 3\pi/2$. In this way, $\mathrm{Re}(\sigma) < 0$ and $\mathrm{Im}(\sigma) > 0$ when $\lambda = |\lambda| e^{i\omega}$ with $0 \le \omega < \pi$. Moreover, $\sigma(\lambda)$ is analytic in $\mathrm{Im}(\lambda) > 0$, and satisfies $\lambda \to 0$ then $\sigma \to -1$. By comparing (3.21) and (3.22) with (3.19), we conclude that

$$G_\lambda(x; x_0) = -\frac{1}{4\sin\left[\pi\sigma(\lambda)\right]} P_{\sigma(\lambda)}(-x \cdot x_0)\,, \qquad R_\lambda = R_h\left[\sigma(\lambda)\right]\,, \tag{3.24}$$

where $R_h(\sigma)$ is defined in (3.22).

The limiting asymptotics of R_λ for $\tau|\lambda|/\mathcal{D} \gg 1$ and for $\tau|\lambda|/\mathcal{D} \ll 1$ is characterized as follows:

Lemma 3.1 *For $\tau|\lambda|/\mathcal{D} \gg 1$ and with $\lambda = |\lambda| e^{i\omega}$ for $0 \le \omega < \pi$, the asymptotics of R_λ, as defined by (3.22), (3.23), and (3.24), is*

$$R_\lambda \sim \frac{1}{2\pi}\left[-\gamma + \log 2 - \frac{1}{2}\log\left(\frac{\tau|\lambda|}{\mathcal{D}}\right) - \frac{i}{2} Arg\lambda\right] + o(1)\,. \tag{3.25}$$

Alternatively, for $\tau|\lambda|/\mathcal{D} \ll 1$, we have

$$R_\lambda \sim \frac{\mathcal{D}}{4\pi\tau\lambda} + \frac{1}{4\pi}(\log 4 - 1) + o(1)\,. \tag{3.26}$$

Proof The result (3.26) follows readily from either expanding (3.22) for $\sigma \to -1$, or by seeking an expansion of the solution to (3.19) in the form $G_\lambda = A\mathcal{D}/(\tau\lambda) + G + o(1)$, for some constant A. We readily obtain $A = 1/|\Omega| = (4\pi)^{-1}$ and that G is the source-neutral Green's function of (2.8) and (2.9). This establishes (3.26).

Next we derive (3.25). For $\tau|\lambda|/\mathcal{D} \gg 1$ with $\lambda = |\lambda|e^{i\omega}$ for $0 \le \omega < \pi$, we have $|\sigma| \to \infty$ with $\mathrm{Im}(\sigma) > 0$. In this limit, $\cot(\pi\sigma) \to -i$. In addition, for $|\sigma| \to \infty$, we have $\Phi(\sigma+1) \sim \log\sigma + 1/2\sigma$, where $\log\sigma$ is the principal branch of the logarithm (cf. [**1**]). Moreover, from (3.23), we obtain $\sigma \sim \left[\tau|\lambda|\mathcal{D}^{-1}\right]^{1/2} e^{i(\pi+\mathrm{Arg}(\lambda))/2}$. Thus, from (3.22) we get

$$R_\lambda \sim \frac{1}{4\pi}\left[2\log 2 - 2\log\sigma + i\pi - 2\gamma\right] \sim \frac{1}{2\pi}\left[\log 2 - \gamma - \frac{1}{2}\log\left(\frac{\tau|\lambda|}{\mathcal{D}}\right) - \frac{i}{2}\mathrm{Arg}\lambda\right],$$

which agrees with (3.25). As an alternate, but formal, derivation of (3.25), a simple boundary layer analysis for $\tau|\lambda|/\mathcal{D} \gg 1$ shows that the solution to (3.19) can be approximated by the free-space Green's function solution $G_f = (2\pi)^{-1}K_0(\beta|x - x_0|)$, where $\beta \equiv \sqrt{\tau\lambda/\mathcal{D}}$, which satisfies $\Delta G_f - \tau\lambda G_f/\mathcal{D} = -\delta(x - x_0)$ on the infinite tangent-plane to the sphere centered at x_0. The regular part of this modified Bessel function solution yields (3.25). □

Next, we expand η in (3.18) as $x \to x_i$ and impose the matching condition that the resulting limiting behavior must agree with that in (3.9). In this way, we obtain that

$$c_i + 2\pi\nu\left(c_i R_\lambda + \sum_{j\neq i}^{N} c_j G_{\lambda ij}\right) + \nu\tilde{B}_i c_i = 0\,, \qquad \text{for} \quad i = 1,\dots,N\,. \tag{3.27}$$

Upon writing (3.27) in matrix form, we conclude that any discrete eigenvalues of the GCEP for $\tau > 0$ must be such that the matrix problem

$$\mathcal{M}\mathbf{c} = 0\,, \qquad \text{where} \qquad \mathcal{M} \equiv I + 2\pi\nu\mathcal{G}_\lambda + \nu\tilde{B}\,, \tag{3.28}$$

has a non-trivial solution, i.e., that $\det\mathcal{M} = 0$. Here we have defined $\mathbf{c}$, $\mathcal{G}_\lambda$, and $\mathcal{B}_\lambda$ by

$$\mathbf{c} \equiv \begin{pmatrix} c_1 \\ \vdots \\ c_N \end{pmatrix}, \qquad \mathcal{G}_\lambda \equiv \begin{pmatrix} R_\lambda & & G_{\lambda ij} \\ & \ddots & \\ G_{\lambda ij} & & R_\lambda \end{pmatrix}, \qquad \mathcal{B} \equiv \begin{pmatrix} \tilde{B}_1 & & 0 \\ & \ddots & \\ 0 & & \tilde{B}_N \end{pmatrix}, \tag{3.29}$$

where $G_{\lambda ij} \equiv G_\lambda(x_i; x_j)$, and $\tilde{B}_i \equiv \tilde{B}_i(\lambda; S_i, f)$ is to be calculated from (3.5). We remark that the Green's matrix $\mathcal{G}_\lambda$ has common entries along its diagonal that are independent of the spot locations. However, in contrast to the case where $\tau = 0$, the difference $G_\lambda(x_i; x_j) + \frac{1}{2\pi}\log|x_i - x_j|$ now depends on the distance $|x_i - x_j|$.

Now suppose that $\mathcal{G}$, and consequently $\mathcal{G}_\lambda$, has a constant row sum. Then, the nonlinear algebraic system (2.14 *a*) admits a solution for which the spots have a common source strength $S_c \equiv S_1 = \ldots = S_N$ so that $\tilde{B}_c(\lambda; S_c, f) = \tilde{B}_j(\lambda; S_j, f)$ for $j = 1,\dots,N$. Since $\mathcal{B} = \tilde{B}_c(\lambda; S_c, f)I$, the matrix $\mathcal{M}$ in (3.28) reduces to

$$\mathcal{M} = I + 2\pi\nu\mathcal{G}_\lambda + \nu\tilde{B}_c I\,.$$

In terms of the matrix spectrum of $\mathcal{G}_\lambda$ given by $\mathcal{G}_\lambda\mathbf{b_j} = k_{j\lambda}\mathbf{b_j}$ for $j = 1,\dots,N$, it follows that

$$\mathcal{M}\mathbf{b_j} = \left(1 + 2\pi\nu k_{j\lambda} + \nu\tilde{B}_c\right)\mathbf{b_j}\,.$$

We conclude that $\det \mathcal{M} = 0$ when

$$1 + 2\pi\nu k_{j\lambda} + \nu\tilde{B}_c = 0\,, \qquad j = 1, \ldots, N\,. \tag{3.30}$$

We summarize this result as follows:

Principal Result 3.3 *Let $\tau > 0$ and suppose that $S_c \equiv S_1 = \ldots = S_N$. Corresponding to radially symmetric perturbations near each spot, there is a complex conjugate pair of pure imaginary eigenvalues at any critical pair $(\tau, \lambda) = (\tau_H, i\lambda_{IH})$, with $\lambda_{IH} > 0$, that is a root of the coupled system*

$$\nu^{-1} + 2\pi Re[k_{j\lambda}] + Re[\tilde{B}_c(i\lambda_I; S_c, f)] = 0\,, \qquad 2\pi Im[k_{j\lambda}] + Im[\tilde{B}_c(i\lambda_I; S_c, f)] = 0\,, \qquad j = 1, \ldots, N\,. \tag{3.31}$$

Here $k_{j\lambda}$ for $j = 1, \ldots, N$ are the eigenvalues of $\mathcal{G}_\lambda$. Since $\mathcal{G}_\lambda$ is symmetric with a constant row sum, its matrix spectrum is

$$\mathcal{G}_\lambda \mathbf{e} = k_{1\lambda}\mathbf{e}\,; \qquad \mathcal{G}_\lambda \mathbf{b_j} = k_{j\lambda}\mathbf{b_j}\,, \quad \textit{with} \quad \mathbf{b_j}^T\mathbf{e} = 0 \quad \textit{for} \quad j = 2, \ldots, N\,. \tag{3.32}$$

In (3.31), we recall that $\tilde{B}_c(i\lambda_I; S_c, f)$ is to be calculated from

$$\begin{aligned} &\Delta_\rho\tilde{\psi} - \tilde{\psi} + 2fu_cv_c\tilde{\psi} + fu_c^2\tilde{N} = i\lambda_I\tilde{\psi}\,; \qquad \tilde{\psi}'(0) = 0\,; \qquad \tilde{\psi} \to 0 \quad as \quad \rho \to \infty\,, \\ &\Delta_\rho\tilde{N} + \tilde{\psi}(1 - 2u_cv_c) = u_c^2\tilde{N}\,; \qquad \tilde{N}'(0) = 0\,; \qquad \tilde{N} \sim \log\rho + \tilde{B}_c(i\lambda_I; S_c, f) + o(1) \quad as \quad \rho \to \infty\,. \end{aligned} \tag{3.33}$$

We remark that as $\tau/\mathcal{D}$ increases it is impossible for eigenvalues to enter $\mathrm{Re}(\lambda) > 0$ along the real axis by crossing through $\lambda = 0$. This follows since $\mathcal{G}_\lambda$ depends only on the product $\tau\lambda/\mathcal{D}$, which vanishes when $\lambda = 0$. We further remark that $\mathcal{G}_\lambda$ is symmetric, but not Hermitian when $\lambda = i\lambda_I$, since $G_{\lambda ij} \neq \overline{G_{\lambda ji}}$. Thus, the eigenvalues $k_{\lambda j}$ of $\mathcal{G}_\lambda$ are in general complex-valued. In the special case where the spot locations $\{x_1, \ldots, x_N\}$ are such that $\mathcal{G}_\lambda$ is both circulant and symmetric, its eigenvalues and real eigenvectors can be found explicitly (see Appendix D).

For a fixed f and a given ε with $\varepsilon \ll 1$, the formulation of Principal Result 3.3 is used to compute the curve E versus $\mathcal{D}$ at which a Hopf bifurcation occurs. To do so, it is convenient to introduce new variables $\tilde{\tau}$ and $\tilde{\mathcal{D}}$ defined by

$$\tilde{\tau} \equiv \frac{\tau}{D} = \frac{1}{f^2\mathrm{E}^2\tilde{\mathcal{D}}}\,, \qquad \tilde{\mathcal{D}} \equiv \frac{\mathcal{D}}{\mathrm{E}^2}\,. \tag{3.34}$$

Then, for a pattern with a common source strength we have $S_c = 2/(N\sqrt{\tilde{\mathcal{D}}})$, and in the computation of both the Green's function in (3.24) and the eigenvalues of the Green's matrix in (3.30) we simply replace $\tau/\mathcal{D}$ by $\tilde{\tau}$. A Hopf bifurcation curve $\tilde{\tau}$ versus $\tilde{\mathcal{D}}$ is computed from a 2×2 matrix Newton solve on the nonlinear system (3.31) for $\tilde{\tau}$ and λ_I. In this procedure, the real and imaginary parts of $\tilde{B}_c(i\lambda_I; S_c, f)$ are calculated from the linear complex-valued BVP (3.33) with $S_c = 2/(N\sqrt{\tilde{\mathcal{D}}})$ by first separating the solution to (3.33) into real and imaginary parts. Finally, the Hopf bifurcation curve E versus $\mathcal{D}$ is given parametrically in terms of $\tilde{\tau}$ and $\tilde{\mathcal{D}}$ by

$$\mathrm{E} = \frac{1}{f}\left(\tilde{\tau}\tilde{\mathcal{D}}\right)^{-1/2}\,, \qquad \mathcal{D} = \frac{1}{\tilde{\tau}f^2}\,. \tag{3.35}$$

To implement this numerical procedure, it is essential to obtain a good initial guess for the Newton solve. For the synchronous mode, such an initial guess is available in the near-shadow limit $\tilde{\mathcal{D}} \gg 1$. For $\tilde{\tau} \ll 1$, we readily obtain from (3.26) that the Green's matrix can be approximated by (see (4.40) below)

$$\mathcal{G}_\lambda \sim -\left(\frac{iN}{4\pi\tilde{\tau}\lambda_I}\right)\mathcal{E}_0 + \frac{N}{4\pi}\left(\log 4 - 1\right)\mathcal{E}_0 - \frac{1}{2\pi}\mathcal{G} + \cdots\,. \tag{3.36}$$

Here $\mathcal{E}_0 \equiv \mathbf{e}\mathbf{e}^T/N$ is given in (2.14 *a*), and $\mathcal{G}$ is the matrix of logarithmic interactions as defined in (2.13). Therefore,

for the eigenvalue $k_{1\lambda}$ corresponding to the synchronous mode we have

$$\mathrm{Re}(k_{1\lambda}) = \frac{N}{4\pi}(\log 4 - 1) - \frac{\kappa_0}{2\pi}\,, \qquad \mathrm{Im}(k_{1\lambda}) = -\frac{N}{4\pi\tilde{\tau}\lambda_I}\,, \tag{3.37}$$

where $\mathcal{G}\mathbf{e} = \kappa_0\mathbf{e}$. Since $\mathrm{Re}(k_{1\lambda})$ is independent of $\tilde{\tau}$ when $\tilde{\mathcal{D}} \gg 1$, the first equation of (3.31) is asymptotically independent of $\tilde{\tau}$ and can be solved numerically for λ_I. With λ_I known, the second equation in (3.31) determines $\tilde{\tau}$. This procedure provides a good initial guess for the synchronous mode when $\tilde{\mathcal{D}}$ is large. Upon convergence of the Newton iterates at the initial value of $\tilde{\mathcal{D}}$, an Euler continuation strategy is used to compute the Hopf curve as $\tilde{\mathcal{D}}$ is decreased.

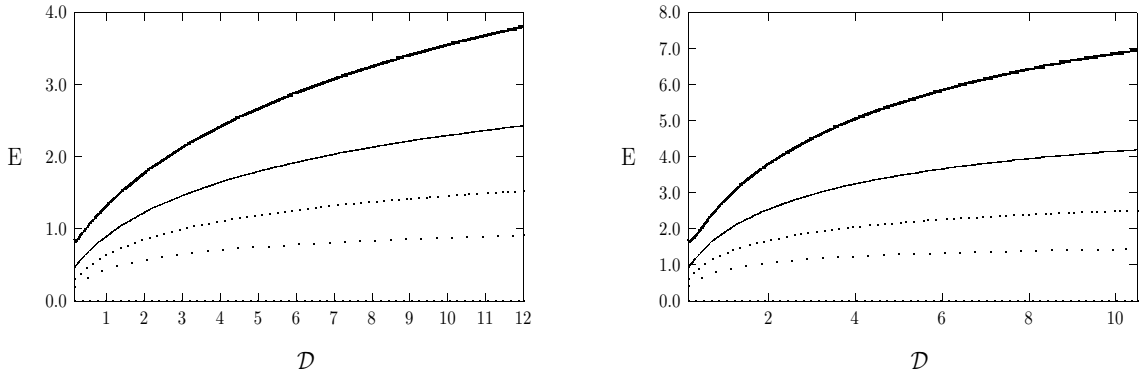

FIGURE 8. The Hopf bifurcation threshold E versus $\mathcal{D}$ when $\varepsilon = 0.06$ for $f = 0.4$ (heavy solid curve), $f = 0.5$ (solid curve), $f = 0.6$ (dotted curve), and $f = 0.7$ (widely spaced dots). Left panel: a one-spot solution. Right panel: a two-spot solution with spots at antipodal points on the sphere. The threshold in the right panel corresponds to the synchronous mode.

In the left panel of Fig. 8 we plot the numerically computed Hopf bifurcation threshold E versus $\mathcal{D}$ for a one-spot solution when $\varepsilon = 0.06$ at four different values of f. We predict that an oscillatory instability of a one-spot pattern occurs when E is below any of the curves in the left panel of Fig. 8. Similarly, for $\varepsilon = 0.06$ and the same four values of f, in the right panel of Fig. 8 we plot the numerically computed Hopf bifurcation threshold for the synchronous mode for a two-spot pattern with spots at anti-podal points on the sphere. In §4.3 and 4.4 below, we will show for $\mathcal{D} \gg 1$ that, to leading order in $\nu = -1/\log\varepsilon$, an approximate Hopf bifurcation threshold for the synchronous mode can be determined from a class of nonlocal eigenvalue problem (NLEP).

For the two-spot pattern, with spots at anti-podal points on the sphere, there is also a Hopf bifurcation threshold associated with the competition instability mode provided that $\mathcal{D}$ is below a threshold. To numerically compute this threshold, the initial condition for the Newton iteration on (3.31) is taken to correspond to the large $\tilde{\tau}$ approximation, for which the Green's matrix reduces to $\mathcal{G}_\lambda \sim R_\lambda I$, where I is the identity and R_λ is approximated as in (3.25). In the left panel of Fig. 9 the solid curves are the numerically computed Hopf bifurcation thresholds for the competition mode for the same four values of f as in the right panel of Fig. 8. The Hopf bifurcation threshold for the synchronous mode is superimposed in this figure. Since the Hopf bifurcation curves for the competition mode lie below those for the synchronous mode, it follows that a synchronous oscillatory instability is triggered first as E decreases below a threshold. As seen in the right panel of Fig. 9, the Hopf bifurcation curve for the competition mode terminates at the value of $\mathcal{D}$ for which the corresponding Hopf bifurcation frequency λ_I approaches zero. This termination of the Hopf bifurcation for the competition mode at finite $\mathcal{D}$ is further examined in §4.3 and §4.4, where we derive and then analyze an NLEP, which is valid to leading order in ν when $\mathcal{D} \gg 1$, that determines any Hopf bifurcations for the

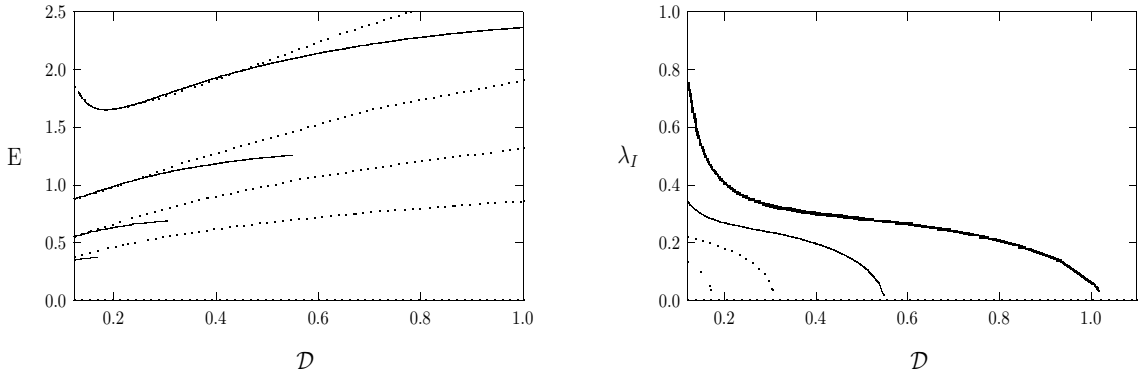

FIGURE 9. Left panel: the competition (solid curves) and synchronous (dashed curves) Hopf instability thresholds E versus $\mathcal{D}$ when $\varepsilon = 0.06$. The pair of curves from top to bottom are for $f = 0.4$, $f = 0.5$, $f = 0.6$, and $f = 0.7$. The synchronous mode is seen to set the instability threshold. Right panel: the modulus λ_I of the complex eigenvalue for the competition Hopf instability threshold for $f = 0.4$ (heavy solid), $f = 0.5$ (solid), $f = 0.6$ (dotted curve), and $f = 0.7$ (widely spaced dots). For each f, $\lambda_I \to 0^+$ at some critical value of $\mathcal{D}$.

competition mode in this limit. In Principal Result 4.6 we will prove that there are no Hopf bifurcations associated with this NLEP. We remark that the competition and synchronouus Hopf bifurcation curves shown in the left panel of Fig. 9 are qualitatively similar to those that occur for spike patterns in the 1-D Gierer-Meinhardt RD system (see Fig. 18 of [**43**]).

4 The Limit of Small Source Strength: Two-Term Asymptotics

In this section we obtain explicit analytical results for an N-spot quasi-equilibrium solution in the small source-strength limit $S_j \to 0$. In §4.2 we derive asymptotic results for the competition instability thresholds in this limit. One distinguished limit for the small S_j asymptotics corresponds to the parameter range $\mathcal{D} = \mathcal{O}(\nu^{-1})$ with $\mathrm{E} = \mathcal{O}(1)$, and so we write $\mathcal{D} = \mathcal{D}_0/\nu \gg 1$ with $\mathcal{D}_0 = \mathcal{O}(1)$. For the case $\tau > 0$, $\mathcal{D} = \mathcal{O}(\nu^{-1})$, and $\mathrm{E} = \mathcal{O}(1)$, in §4.3 we derive a nonlocal eigenvalue problem (NLEP) governing the stability of an N-spot quasi-equilibrium pattern. This NLEP is analyzed rigorously in §4.4. In addition, in §4.5 we consider the limit $\mathcal{D} \ll 1$ but with E sufficiently small so that the source-strength is still asymptotically small, i.e. $S_c = 2\mathrm{E}/(\sqrt{\mathcal{D}}N) \ll 1$. For the stability analysis this parameter range leads to a new type of NLEP that has a Hopf bifurcation with an anomalous scaling in ε.

We first must calculate an asymptotic solution to the core problem (2.3), which is valid for $S_j \to 0$. This analysis yields a two-term asymptotic result for $\chi(S_j; f)$ when $S_j \ll 1$, which is needed to determine the stability thresholds.

4.1 Core problem: Small S-Asymptotics

In the limit $S \to 0$, we now derive a two-term approximation to the radially symmetric solution on $0 < \rho < \infty$ to

$$\Delta_\rho u - u + f u^2 v = 0\,, \quad u \to 0 \quad \text{as} \quad \rho \to \infty\,; \qquad \Delta_\rho v + u - u^2 v = 0\,, \quad v \sim S\log\rho + \chi \quad \text{as} \quad \rho \to \infty\,, \tag{4.1}$$

with $u'(0) = v'(0) = 0$ and $\Delta_\rho \equiv \partial_{\rho\rho} + \frac{1}{\rho}\partial_\rho$. We write $u = S\tilde{u}$, $v = \tilde{v}/S$, and $\chi = \tilde{\chi}/S$ to obtain

$$\Delta_\rho \tilde{u} - \tilde{u} + f\tilde{u}^2\tilde{v} = 0\,, \quad \tilde{u} \to 0 \quad \text{as} \quad \rho \to \infty\,; \qquad \Delta_\rho \tilde{v} + S^2(\tilde{u} - \tilde{u}^2\tilde{v}) = 0\,, \quad \tilde{v} \sim S^2\log\rho + \tilde{\chi} \quad \text{as} \quad \rho \to \infty\,. \tag{4.2}$$

The form of (4.2) suggests that we should seek an asymptotic solution for $S \ll 1$ as

$$\tilde{u} = \tilde{u}_0 + S^2\tilde{u}_1 + S^4\tilde{u}_2 + \cdots\,, \qquad \tilde{v} = \tilde{v}_0 + S^2\tilde{v}_1 + S^4\tilde{v}_2 + \cdots\,, \qquad \tilde{\chi} = \tilde{\chi}_0 + S^2\tilde{\chi}_1 + S^4\tilde{\chi}_2 + \ldots\,.$$

Upon substituting this expansion into (4.2), and collecting powers of S^2, we obtain that

$$\Delta_\rho \tilde{u}_0 - \tilde{u}_0 + f\tilde{u}_0^2\tilde{v}_0 = 0\,, \qquad \tilde{u}_0 \to 0 \quad \text{as} \quad \rho \to \infty\,; \qquad \Delta_\rho \tilde{v}_0 = 0\,, \qquad \tilde{v}_0 \to \tilde{\chi}_0 \quad \text{as} \quad \rho \to \infty\,. \tag{4.3}$$

At order $\mathcal{O}(S^2)$, we get

$$\begin{aligned} \Delta_\rho \tilde{u}_1 - \tilde{u}_1 + 2f\tilde{u}_0\tilde{v}_0\tilde{u}_1 &= -f\tilde{u}_0^2\tilde{v}_1, \qquad \tilde{v}_1 \to 0 \quad \text{as} \quad \rho \to \infty, \\ \Delta_\rho \tilde{v}_1 &= -\tilde{u}_0 + \tilde{u}_0^2\tilde{v}_0, \qquad \tilde{v}_1 \to \log\rho + \tilde{\chi}_1 \quad \text{as} \quad \rho \to \infty\,, \end{aligned} \tag{4.4}$$

while at order $\mathcal{O}(S^4)$ we obtain that $\tilde{v}_2$ is bounded as $\rho \to \infty$ and satisfies

$$\Delta_\rho \tilde{v}_2 = -\tilde{u}_1 + 2\tilde{u}_0\tilde{v}_0\tilde{u}_1 + \tilde{u}_0^2\tilde{v}_1\,. \tag{4.5}$$

The solution to (4.3) is

$$\tilde{u}_0 = \frac{1}{f\tilde{v}_0}w\,, \qquad \tilde{v}_0 = \tilde{\chi}_0\,, \tag{4.6}$$

where $w(\rho)$ is the unique ground-state solution satisfying

$$\Delta_\rho w - w + w^2 = 0\,, \quad 0 < \rho < \infty\,; \qquad w(0) > 0\,, \quad w'(0) = 0\,; \qquad w \to 0 \quad \text{as} \quad \rho \to \infty\,. \tag{4.7}$$

Upon integrating this ground-state problem we obtain the identity $\int_0^\infty w\rho\,d\rho = \int_0^\infty w^2\rho d\rho$.

Since $\tilde{v}_{1\rho} \sim 1/\rho$ as $\rho \to \infty$, we obtain upon integrating the $\tilde{v}_1$ equation in (4.4), and then using (4.6), that

$$\lim_{\rho\to\infty} \rho\tilde{v}_{1\rho} = 1 = \int_0^\infty \left(\tilde{u}_0^2\tilde{v}_0 - \tilde{u}_0\right)\rho\,d\rho = \frac{(1-f)}{f^2\tilde{v}_0}\int_0^\infty w^2\rho\,d\rho\,,$$

which determines $\tilde{v}_0$. From a numerical quadrature, $\tilde{v}_0$ and $\tilde{\chi}_0$ are calculated as

$$\tilde{v}_0 = \tilde{\chi}_0 = \frac{b(1-f)}{f^2}\,, \qquad \text{where} \qquad b \equiv \int_0^\infty w^2\rho\,d\rho \approx 4.9343\,. \tag{4.8}$$

With the leading-order terms determined, the problem (4.4) for $\tilde{u}_1$ and $\tilde{v}_1$ becomes

$$\begin{aligned} \Delta_\rho \tilde{u}_1 - \tilde{u}_1 + 2w\tilde{u}_1 &= -\frac{1}{f\tilde{v}_0^2}w^2\tilde{v}_1\,, \qquad \tilde{u}_1 \to 0 \quad \text{as} \quad \rho \to \infty\,, \\ \Delta_\rho \tilde{v}_1 &= \frac{1}{\tilde{v}_0}\left(\frac{w^2}{f^2} - \frac{w}{f}\right)\,, \qquad \tilde{v}_1 \sim \log\rho + \tilde{\chi}_1 \quad \text{as} \quad \rho \to \infty\,. \end{aligned} \tag{4.9}$$

Moreover, the boundedness condition for the solution to the $\tilde{v}_2$ equation (4.5) yields, upon using (4.6), that

$$\int_0^\infty \tilde{u}_1\rho\,d\rho = \int_0^\infty 2\tilde{u}_0\tilde{v}_0\tilde{u}_1\rho\,d\rho + \int_0^\infty \tilde{u}_0^2\tilde{v}_1\rho\,d\rho = \frac{2}{f}\int_0^\infty w\tilde{u}_1\rho\,d\rho + \frac{1}{f^2\tilde{v}_0^2}\int_0^\infty w^2\tilde{v}_1\rho\,d\rho\,. \tag{4.10}$$

Upon integrating the $\tilde{u}_1$ equation in (4.9) we obtain that $\int_0^\infty \tilde{u}_1\rho\,d\rho = 2\int_0^\infty w\tilde{u}_1\rho\,d\rho + \left[f\tilde{v}_0^2\right]^{-1}\int_0^\infty w^2\tilde{v}_1\rho\,d\rho$. By comparing this expression with (4.10), we conclude that

$$\int_0^\infty \tilde{u}_1\rho\,d\rho = 0\,. \tag{4.11}$$

We now show how (4.11) determines $\tilde{\chi}_1$. We return to (4.9). The solution for $\tilde{v}_1$ is decomposed as

$$\tilde{v}_1 = \tilde{\chi}_1 + \frac{1}{\tilde{v}_0 f^2}\tilde{v}_{1p}\,, \tag{4.12}$$

where $\tilde{v}_{1p}$ is the unique solution on $0 < \rho < \infty$ to

$$\Delta_\rho \tilde{v}_{1p} = w^2 - fw\,, \quad 0 < \rho < \infty\,; \qquad \tilde{v}_{1p}'(0) = 0\,; \qquad \tilde{v}_{1p} \sim \tilde{v}_0 f^2\log\rho + o(1) \quad \text{as} \quad \rho \to \infty\,. \tag{4.13}$$

The condition that $\tilde{v}_{1p} - \tilde{v}_0 f^2\log\rho \to 0$ as $\rho \to \infty$ ensures that $\tilde{v}_{1p}$ is unique. In terms of $\tilde{v}_{1p}$, $\tilde{u}_1$ from (4.9) satisfies

$$L_0\tilde{u}_1 \equiv \Delta_\rho \tilde{u}_1 - \tilde{u}_1 + 2w\tilde{u}_1 = -\frac{\tilde{\chi}_1}{f\tilde{v}_0^2}w^2 - \frac{w^2}{\tilde{v}_0^3 f^3}\tilde{v}_{1p}\,.$$

Now, since $L_0 w = w^2$, as seen from $L_0 w = \Delta_\rho w - w + 2w^2 = -w^2 + 2w^2 = w^2$, we can decompose $\tilde{u}_1$ as

$$\tilde{u}_1 = -\frac{\tilde{\chi}_1}{f\tilde{v}_0^2} w - \frac{1}{\tilde{v}_0^3 f^3}\tilde{u}_{1p}\,, \qquad \text{where} \qquad L_0\tilde{u}_{1p} = w^2\tilde{v}_{1p}\,. \tag{4.14}$$

Next, we determine $\tilde{\chi}_1$. We substitute $\tilde{u}_1$ from (4.14) into the solvability condition (4.11) to obtain

$$\tilde{\chi}_1 \int_0^\infty w\rho\, d\rho = -\frac{1}{\tilde{v}_0 f^2}\int_0^\infty \tilde{u}_{1p}\,\rho\, d\rho\,.$$

Upon using $\int_0^\infty w\rho\, d\rho = \int_0^\infty w^2\rho\, d\rho \equiv b$, and (4.8) for $\tilde{v}_0$, we determine $\tilde{\chi}_1$ in terms of $\tilde{u}_{1p}$ as

$$\tilde{\chi}_1 = -\frac{1}{b^2(1-f)}\int_0^\infty \tilde{u}_{1p}\,\rho\, d\rho\,. \tag{4.15}$$

We can simplify (4.15) to obtain a formula for $\tilde{\chi}_1$ where the dependence on f appears explicitly rather than implicitly through $\tilde{u}_{1p}$. To obtain such a result, we use $w^2 = w - \Delta_\rho w$ to write the problem (4.13) for $\tilde{v}_{1p}$ as

$$\Delta_\rho(\tilde{v}_{1p} + w) = (1-f)w\,, \quad 0 < \rho < \infty\,; \qquad \tilde{v}_{1p}'(0) = 0\,; \qquad \tilde{v}_{1p} \sim (1-f)b\log\rho + o(1) \quad \text{as} \quad \rho\to\infty\,,$$

which motivates introducing $\tilde{v}_{1Q}$ as $\tilde{v}_{1p} + w = (1-f)\tilde{v}_{1Q}$. Here $\tilde{v}_{1Q}$ is the unique solution of the parameter-free problem

$$\Delta_\rho\tilde{v}_{1Q} = w\,, \quad 0 < \rho < \infty\,; \qquad \tilde{v}_{1Q}'(0) = 0\,; \qquad \tilde{v}_{1Q} \to b\log\rho + o(1) \quad \text{as} \quad \rho\to\infty\,. \tag{4.16}$$

Now, with $\tilde{v}_{1p} = -w + (1-f)\tilde{v}_{1Q}$, the problem (4.14) for $\tilde{u}_{1p}$ becomes $L_0\tilde{u}_{1p} = -w^3 + (1-f)w^2\tilde{v}_{1Q}$. Therefore, we decompose $\tilde{u}_{1p}$ as $\tilde{u}_{1p} = -\tilde{u}_{1pI} + (1-f)\tilde{u}_{1pII}$, where $\tilde{u}_{1pI}$ and $\tilde{u}_{1pII}$ are the unique solutions of

$$L_0\tilde{u}_{1pI} = w^3 \qquad \text{and} \qquad L_0\tilde{u}_{1pII} = w^2\tilde{v}_{1Q}\,, \tag{4.17}$$

with $\tilde{u}_{1pI} \to 0$ and $\tilde{u}_{1pII} \to 0$ as $\rho\to\infty$. Then, an expression for $\tilde{\chi}_1$, in which the dependence on f is explicit, is obtained by substituting this decomposition for $\tilde{u}_{1p}$ into (4.15). We summarize our results as follows:

Principal Result 4.1 *In the limit $S\to 0$, a two-term expansion for the solution to the core problem (4.1) is*

$$u \sim S\left[\tilde{u}_0 + S^2\tilde{u}_1 + \cdots\right]\,, \qquad v \sim \frac{1}{S}\left[\tilde{v}_0 + S^2\tilde{v}_1 + \cdots\right]\,, \qquad \chi \sim \frac{\tilde{\chi}_0}{S} + S\tilde{\chi}_1 + \cdots\,, \tag{4.18}$$

where

$$\begin{aligned}
&\tilde{u}_0 = \frac{1}{f\tilde{v}_0}w\,, \qquad \tilde{u}_1 = -\frac{\tilde{\chi}_1}{f\tilde{v}_0^2}w - \frac{1}{\tilde{v}_0^3 f^3}\left[-\tilde{u}_{1pI} + (1-f)\tilde{u}_{1pII}\right]\,,\\
&\tilde{v}_0 = \frac{b(1-f)}{f^2}\,, \qquad \tilde{v}_1 = \tilde{\chi}_1 + \frac{1}{\tilde{v}_0 f^2}\left[-w + (1-f)\tilde{v}_{1Q}\right]\,,\\
&\tilde{\chi}_0 = \frac{b(1-f)}{f^2}, \qquad \tilde{\chi}_1 = \frac{1}{b^2(1-f)}\int_0^\infty \tilde{u}_{1pI}\,\rho\, d\rho - \frac{1}{b^2}\int_0^\infty \tilde{u}_{1pII}\rho\, d\rho\,.
\end{aligned} \tag{4.19}$$

Here $b = \int_0^\infty w^2\rho\, d\rho$, and $w(\rho)$ is the solution of (4.7). Moreover, $\tilde{v}_{1Q}$ is the unique radially symmetric solution to (4.16), while $\tilde{u}_{1pI}$ and $\tilde{u}_{1pII}$ are the unique radially symmetric solutions to (4.17).

Since $\tilde{v}_{1Q}$, $\tilde{u}_{1pI}$, and $\tilde{u}_{1pII}$ do not depend on the parameter f, we only need to compute the two integrals in the expression (4.19) for $\tilde{\chi}_1$ once. By evaluating them numerically, we obtain an explicit two-term result for χ of the form

$$\chi \sim \frac{d_0}{S} + d_1 S + \mathcal{O}(S^3)\,, \quad \text{as} \quad S\to 0\,; \quad \text{where} \quad d_0 \equiv \frac{b(1-f)}{f^2}\,, \quad b \approx 4.9343\,, \quad d_1 \approx \frac{0.4893}{(1-f)} - 0.4698\,. \tag{4.20}$$

For a few values of f, in Fig. 10 we show a favorable comparison between the two-term asymptotic result (4.20) and the full numerical result for $\chi(S;f)$, as computed from (4.1), up to $S = 1$. These results show that the range of S where (4.20) accurately determines $\chi(S;f)$ decreases as f increases.

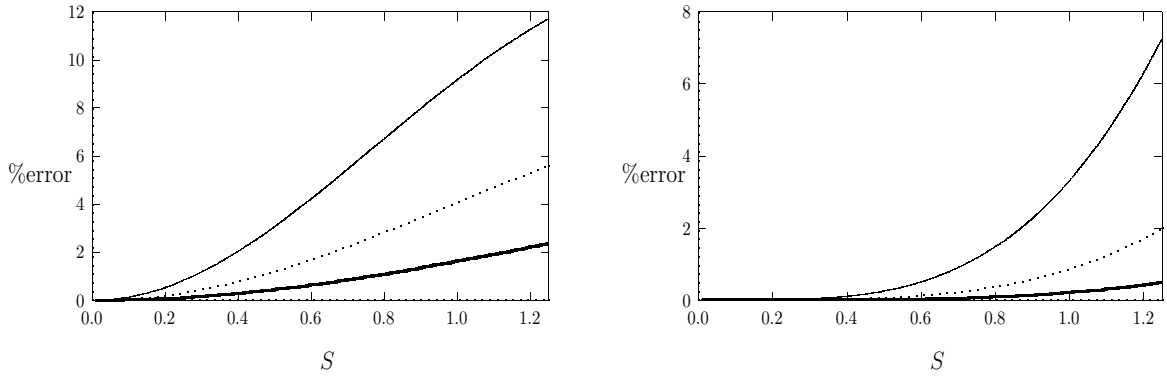

FIGURE 10. The percentage error between the numerical result for $\chi(S;f)$, as computed from the core problem (4.1), and the asymptotic result (4.20) is plotted versus S for $f=0.4$ (heavy solid curves), $f=0.5$ (dotted curves) and $f=0.6$ (solid curves). The left and right panels are the one-term and two-term asymptotic results, respectively. The two-term asymptotic result from (4.20), derived in the limit $S\to 0$, is seen to agree rather favorably with full numerics even up to $S=1$.

Next, we use the leading-order asymptotic result for $\chi(S_i;f)$ to simplify the nonlinear algebraic system (2.12) in the limit $\mathcal{D}=\mathcal{O}(\nu^{-1})$ for which $S_i \ll 1$. Upon substituting $\chi(S_i;f)\sim b(1-f)/(f^2S_i)$ and $\mathcal{D}=\mathcal{D}_0/\nu$ into (2.12), where $\mathcal{D}_0=\mathcal{O}(1)$, we obtain that

$$S_i - \mathcal{O}(\nu) + \frac{\nu b(1-f)}{f^2 S_i} \sim \nu\bar{v}\,, \quad \text{for} \quad i=1,\dots,N\,; \qquad \sum_{j=1}^{N} S_j = \frac{2\mathrm{E}\,\nu^{1/2}}{\sqrt{\mathcal{D}_0}}\,.$$

We then put $S_i=\nu^{1/2}\tilde{S}_i$ and $\bar{v}=\nu^{-1/2}\bar{v}_0$ to obtain the reduced problem

$$\mathcal{H}(\tilde{S}_i)\equiv \tilde{S}_i + \frac{\gamma}{\tilde{S}_i} = \bar{v}_0\,, \quad \text{for} \quad i=1,\dots,N\,; \qquad \sum_{j=1}^{N}\tilde{S}_j = \frac{2\mathrm{E}}{\sqrt{\mathcal{D}_0}}\,; \qquad \gamma \equiv \frac{b(1-f)}{f^2}\,. \tag{4.21}$$

On $\xi>0$, the function $\mathcal{H}(\xi)$ in (4.21) is convex and satisfies $\mathcal{H}(\xi)\to+\infty$ as $\xi\to 0$ and as $\xi\to\infty$. It has a global minimum at $\xi=\sqrt{\gamma}$ with minimum value $\mathcal{H}(\sqrt{\gamma})=2\sqrt{\gamma}$.

With these properties of $\mathcal{H}(\xi)$, the limiting system (4.21) can be used to construct asymmetric quasi-equilibrium spot patterns where each spot can have one of two possible source strengths $\tilde{S}_-$ and $\tilde{S}_+$ on the interval $0<\tilde{S}_-\le\sqrt{\gamma}\le\tilde{S}_+$. Suppose that there are M spots with source strength $\tilde{S}_-$ and $(N-M)$ spots of source strength $\tilde{S}_+$. Then, from (4.21), $\tilde{S}_\pm$ satisfy the nonlinear scalar nonlinear algebraic problem

$$\mathcal{H}(\tilde{S}_-)=\mathcal{H}(\tilde{S}_+)\,, \qquad M\tilde{S}_- + (N-M)\tilde{S}_+ = \frac{2\mathrm{E}}{\sqrt{\mathcal{D}_0}}\,. \tag{4.22}$$

The bifurcation point where asymmetric quasi-equilibria emerge from the common source strength solution branch is obtained by setting $M=0$ and $\tilde{S}_-=\tilde{S}_+=\sqrt{\gamma}$. This yields $N\sqrt{\gamma}=2\mathrm{E}/\sqrt{\mathcal{D}_0}$. Upon using (4.21) for γ, we get $\mathcal{D}_0=4f^2\mathrm{E}^2/\left[N^2b(1-f)\right]$ and $\mathcal{D}=\mathcal{D}_0/\nu$. This critical value of $\mathcal{D}$ is shown below in (4.25) to coincide with the leading-order-in-ν competition instability threshold of $\mathcal{D}$.

To leading order in ν, similar asymmetric quasi-equilibrium spot patterns in the limit $\mathcal{D}=\mathcal{O}(\nu^{-1})$ have been constructed for related RD models in [**45**] and [**47**] and their stability properties determined through the analysis of certain NLEPs. However, in our stability analysis, we will only focus on quasi-equilibrium patterns with a common source strength.

In the next two sub-sections we simplify our stability theory of § 3 in the small common source strength limit, corresponding to $\mathcal{D}=\mathcal{O}(1/\nu)$ and $\mathrm{E}=\mathcal{O}(1)$, for two specific cases. In §4.2 we will derive an explicit two-term

asymptotic result in powers of ν for the competition instability threshold. For $\tau > 0$, in §4.3 we will derive an NLEP that characterizes, to leading order in ν, both competition and oscillatory instabilities. In comparison to the NLEP's derived for other RD models (see [**44**], [**46**], and [**48**]) the multiplier of the nonlocal term in the NLEP for the Brusselator is a bi-quadratic, rather than bi-linear, function of the eigenvalue parameter.

4.2 Small Source Strength Asymptotics: Competition Instabilities

For the case of equal source strengths $S_c \equiv S_1 = \ldots = S_N$, the competition instability threshold corresponding to a zero eigenvalue crossing is the root of (3.17) of Corollary 3.1. Using the small S asymptotics of $\chi(S;f)$, as given in (4.20), we now calculate a two-term asymptotic result in powers of ν for the critical value of $\mathcal{D}$ at which (3.17) has a root when $\mathcal{D} = \mathcal{D}_0/\nu \gg 1$ and $\mathrm{E} = \mathcal{O}(1)$.

When $\mathcal{D} = \mathcal{D}_0/\nu$, we get $S_c = 2\mathrm{E}\nu^{1/2}/\sqrt{\mathcal{D}_0 N} \ll 1$ and $\chi'(S_c;f) \sim -d_0/S_c^2 + d_1 + \mathcal{O}(S_c^2)$ for $S_c \ll 1$, where d_0 and d_1 are given in (4.20). Therefore, (3.17) becomes $\nu^{-1} - k_{j^\star} = -d_1 + d_0/S_c^2 + \cdots$, which determines S_c as $S_c^2 = \nu d_0/\left[1 + \nu\left(d_1 - k_{j^\star}\right)\right]$. The competition instability threshold in terms of $\mathcal{D}_0$ is obtained by substituting $S_c^2 = 4\nu\mathrm{E}^2/(\mathcal{D}_0 N^2)$ into this expression and solving for $\mathcal{D}_0$. We summarize our result as follows:

Principal Result 4.2 *Suppose that $S_c \equiv S_1 = \ldots = S_N$. Then, for radially symmetric perturbations near each spot, the smallest value of $\mathcal{D}$ for which the linearization has a zero eigenvalue is given for $\varepsilon \to 0$ by*

$$\mathcal{D}_c^\star = \frac{\mathcal{D}_0^\star}{\nu} \qquad \text{where} \qquad \mathcal{D}_0^\star \sim \frac{4\mathrm{E}^2}{N^2 d_0}\left[1 + \nu\left(d_1 - k_{j^\star}\right) + \mathcal{O}(\nu^2)\right]. \tag{4.23}$$

Here $k_{j^\star} \equiv \max_{2\le j\le N} k_j$, where $\mathcal{G}\mathbf{b_j} = k_j\mathbf{b_j}$ with $\mathbf{b_j}^T\mathbf{e} = 0$ for $j = 2,\ldots,N$. In (4.23), d_0 and d_1 are given in (4.20) (see also (4.19) *for $\tilde{\chi}(S;f)$). There are also zero eigenvalue crossings at the other larger critical values of $\mathcal{D}$ given by*

$$\mathcal{D}_j = \frac{\mathcal{D}_{0j}}{\nu} \quad \text{where} \quad \mathcal{D}_{0j} \sim \frac{4\mathrm{E}^2}{N^2 d_0}\left[1 + \nu(d_1 - k_j) + \mathcal{O}(\nu^2)\right], \quad j = 2,\ldots,N, \quad \text{with} \quad j \neq j^\star. \tag{4.24}$$

The leading-order result from (4.23) is

$$\mathcal{D}_c^\star \sim \frac{4f^2\mathrm{E}^2}{N^2 b(1-f)\nu}, \qquad b = \int_0^\infty w^2\rho\,d\rho. \tag{4.25}$$

We observe that $\mathcal{D}_c^\star$ decreases as the number N of spots increases. Therefore, as N increases, there is a larger range of $\mathcal{D}$ where the pattern is unstable to a competition instability.

The novelty of (4.23) is that it is an explicit two-term asymptotic result for the competition instability threshold in terms of both the spot locations, the parameter f, and certain correction terms to the solution to the core problem inherited from the term d_1. These correction terms are at one higher order beyond the leading-order ground-state solution w, which plays a central role in the NLEP theory of [**44**], [**46**], and [**48**] for related RD systems. In §4.3 below we will derive the leading-order NLEP for the Brusselator model indirectly from the small source strength limit.

For a four-spot pattern with spots located at the vertices of a tetrahedron, in Fig. 11 we compare the full numerical result for the competition instability threshold of $\mathcal{D}/\mathrm{E}^2$ versus ν when $f = 0.3$, as computed from (3.17) of Corollary 3.1, with both the two-term and the one-term asymptotic results (4.23) and (4.25), respectively, which are valid for $\nu \ll 1$. On the left end of this figure, where ν is small, the two-term asymptotic result agrees very closely with full numerical results. Even at the right end of this figure, where $\nu \approx 0.33$ ($\varepsilon = 0.05$), both asymptotic approximations are still reasonably close to the full numerical result.

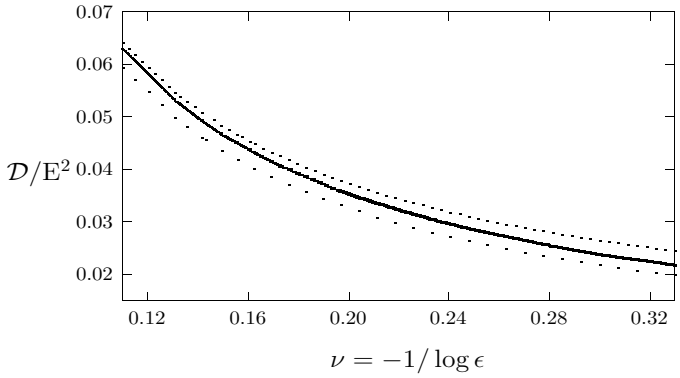

FIGURE 11. The competition instability threshold $\mathcal{D}/\mathrm{E}^2$ versus $\nu = -1/\log\varepsilon$ on $0.0001 < \varepsilon < 0.05$ with $f = 0.3$ for a four-spot pattern with spots located at the vertices of a tetrahedron. The heavy solid curve is the full numerical result computed from (3.17) of Corollary 3.1, the dotted curve is the two-term asymptotic result from (4.23), and the widely spaced dots is the leading-order result (4.25).

4.3 Small Source Strength Asymptotics: Derivation of an NLEP

Next, we assume that $\tau > 0$ and we derive an NLEP that characterizes competition and oscillatory instabilities to leading order in ν when $\mathcal{D} = \mathcal{O}(\nu^{-1}) \gg 1$ and $\mathrm{E} = \mathcal{O}(1)$. We again consider the constant row sum case where $\mathcal{G}\mathbf{e} = k_1\mathbf{e}$ for which there is a quasi-equilibrium spot pattern with a common source strength $S_c \equiv S_1 = \ldots S_N = 2\mathrm{E}/\sqrt{\mathcal{D}}N \ll 1$.

From (3.30), the discrete eigenvalues of the GCEP are the roots of

$$\nu^{-1} + 2\pi k_{j\lambda} + \tilde{B}_c = 0\,, \qquad \text{for} \quad j = 1, \ldots, N\,; \qquad \nu \equiv -1/\log\varepsilon\,. \tag{4.26}$$

Here $\mathcal{G}_\lambda\mathbf{e} = k_{1\lambda}\mathbf{e}$ and $\mathcal{G}_\lambda\mathbf{b_j} = k_{j\lambda}\mathbf{b_j}$, where $\mathbf{b_j}^T\mathbf{e} = 0$ for $j = 2, \ldots, N$. The matrix entries of $\mathcal{G}_\lambda$ are obtained from the solution to (3.24). In (4.26), $\tilde{B}_c = \tilde{B}_c(\lambda; S_c, f)$ is obtained from the complex-valued radially symmetric solution to

$$\begin{aligned} \Delta_\rho\tilde{\psi} - \tilde{\psi} + 2fuv\tilde{\psi} + fu^2\tilde{N} = \lambda\tilde{\psi}\,; \qquad \tilde{\psi}'(0) = 0\,; \qquad \tilde{\psi} \to 0 \quad \text{as} \quad \rho \to \infty\,, \\ \Delta_\rho\tilde{N} - u^2\tilde{N} = -\tilde{\psi}\,(1 - 2uv)\,; \qquad \tilde{N}'(0) = 0\,; \qquad \tilde{N} \sim \log\rho + \tilde{B}_c + o(1) \quad \text{as} \quad \rho \to \infty\,, \end{aligned} \tag{4.27}$$

on $0 < \rho < \infty$, where u, v are solutions to the core problem defined by setting $S = S_c$ in (4.1).

Since $\mathcal{D} = \mathcal{O}(-\log\varepsilon)$, we have $S_c \ll 1$. In the limit $S_c \to 0$, we will first determine an NLEP in terms of $\tilde{B}_c$, as defined from (4.27). For $S_c \to 0$, we recall from (4.18) and (4.19) that

$$u_c \sim \frac{S_c}{f\tilde{v}_0}w\,, \qquad v_c \sim \frac{\tilde{v}_0}{S_c}\,, \qquad \text{where} \quad \tilde{v}_0 \equiv \frac{b(1-f)}{f^2}\,, \tag{4.28}$$

where $w(\rho)$ satisfies (4.7). Upon substituting (4.28) into (4.27), we obtain that

$$\begin{aligned} \Delta_\rho\tilde{\psi} - \tilde{\psi} + 2w\tilde{\psi} - \lambda\tilde{\psi} = -\frac{S_c^2}{f\tilde{v}_0^2}w^2\tilde{N}\,; \qquad \tilde{\psi}'(0) = 0\,; \qquad \tilde{\psi} \to 0 \quad \text{as} \quad \rho \to \infty\,, \\ \Delta_\rho\tilde{N} - \frac{S_c^2}{f^2\tilde{v}_0^2}w^2\tilde{N} = -\tilde{\psi}\left(1 - \frac{2w}{f}\right)\,; \qquad \tilde{N}'(0) = 0\,; \qquad \tilde{N} \sim \log\rho + \tilde{B}_c\,, \quad \text{as} \quad \rho \to \infty\,. \end{aligned} \tag{4.29}$$

Next, for $S_c \ll 1$, we re-scale $\hat{B}_c$ and $\hat{N}$, and expand $\hat{N}$ as

$$\tilde{B}_c = \hat{B}_c/S_c^2\,, \qquad \tilde{N} = \hat{N}/S_c^2\,, \qquad \hat{N} = \hat{B}_c + S_c^2\hat{N}_1 + \mathcal{O}(S_c^4)\,. \tag{4.30}$$

Upon substituting (4.30) into (4.29), we obtain

$$\begin{aligned} &\Delta_\rho\tilde{\psi}-\tilde{\psi}+2w\tilde{\psi}-\lambda\tilde{\psi}=-\frac{w^2}{f\tilde{v}_0^2}\hat{B}_c\,; \qquad \tilde{\psi}'(0)=0\,; \qquad \tilde{\psi}\to 0 \quad \text{as} \quad \rho\to\infty\,,\\ &\Delta_\rho\tilde{N}_1=\tilde{\psi}\left(\frac{2w}{f}-1\right)+\frac{w^2}{f^2\tilde{v}_0^2}\hat{B}_c\,; \qquad \tilde{N}_1'(0)=0\,; \qquad \tilde{N}_1\sim\log\rho+\mathcal{O}(1) \quad \text{as} \quad \rho\to\infty\,. \end{aligned} \tag{4.31}$$

By integrating the equation for $\tilde{N}_1$ over $0<\rho<\infty$, we obtain that

$$\frac{2}{f}\int_0^\infty \tilde{\psi}w\rho\,d\rho-\int_0^\infty\tilde{\psi}\rho\,d\rho+\frac{\hat{B}_c b}{f^2\tilde{v}_0^2}=1\,, \qquad \text{where} \quad b\equiv\int_0^\infty w^2\rho\,d\rho\,. \tag{4.32}$$

Next, upon integrating the equation for $\tilde{\psi}$ in (4.31) over $0<\rho<\infty$, we get

$$-\int_0^\infty\tilde{\psi}\rho\,d\rho+2\int_0^\infty w\tilde{\psi}\rho\,d\rho-\lambda\int_0^\infty\tilde{\psi}\rho\,d\rho=-\frac{\hat{B}_c b}{f\tilde{v}_0^2}\,,$$

which determines $\int_0^\infty\tilde{\psi}\rho\,d\rho$ as

$$\int_0^\infty\tilde{\psi}\rho\,d\rho=\frac{2}{\lambda+1}\int_0^\infty w\tilde{\psi}\rho\,d\rho+\frac{\hat{B}_c b}{f\tilde{v}_0^2(\lambda+1)}\,. \tag{4.33}$$

Then, by combining (4.32) and (4.33), we can eliminate $\int_0^\infty\tilde{\psi}\rho\,d\rho$ to obtain

$$\frac{1}{f}\int_0^\infty w\tilde{\psi}\rho\,d\rho+\frac{\hat{B}_c b}{2f^2\tilde{v}_0^2}=\frac{\lambda+1}{2(\lambda+1-f)}\,. \tag{4.34}$$

In the class of radially symmetric solutions, we can write the solution $\tilde{\psi}$ to (4.31) in terms of the inverse of a local operator L_0 as

$$\tilde{\psi}=-\frac{\hat{B}_c f}{b\alpha}\left(L_0-\lambda\right)^{-1}w^2\,, \qquad \text{where} \quad L_0\tilde{\psi}\equiv\Delta_\rho\tilde{\psi}-\tilde{\psi}+2w\tilde{\psi}\,, \qquad \alpha\equiv\frac{f^2\tilde{v}_0^2}{b}=\frac{b(1-f)^2}{f^2}\,. \tag{4.35}$$

Upon substituting (4.35) into (4.34), we obtain after a short calculation that the discrete eigenvalues λ are the roots of a function $g(\lambda)=0$, where $g(\lambda)$ is defined by

$$g(\lambda)=\frac{(\lambda+1)\left(1-\alpha/\hat{B}_c\right)-f}{2(\lambda+1-f)}-\mathcal{F}(\lambda)\,, \qquad \mathcal{F}(\lambda)\equiv\frac{\int_0^\infty w\left[\left(L_0-\lambda\right)^{-1}w^2\right]\rho\,d\rho}{\int_0^\infty w^2\rho\,d\rho}\,. \tag{4.36}$$

It is easy to show that the roots of (4.36) are the discrete eigenvalues of an NLEP for $\Phi(\rho)$ on $0<\rho<\infty$ given by

$$L_0\Phi-\beta(\lambda)w^2\frac{\int_0^\infty w\Phi\rho\,d\rho}{\int_0^\infty w^2\rho\,d\rho}=\lambda\Phi\,, \qquad \Phi\to 0 \quad \text{as} \quad \rho\to\infty\,; \qquad \beta(\lambda)\equiv\frac{2(\lambda+1-f)}{(\lambda+1)\left(1-\alpha/\hat{B}_c\right)-f}\,. \tag{4.37}$$

The final step in the derivation of the NLEP is to calculate the term $\hat{B}_c$ in the multiplier $\beta(\lambda)$ of (4.37). To do so, we consider (4.26) for $\mathcal{D}=\mathcal{D}_0/\nu$ with $\mathcal{D}_0=\mathcal{O}(1)$ for which $S_c\ll 1$. For $S_c\ll 1$, we have from (4.30) that $\tilde{B}_c=\hat{B}_c/S_c^2$ where $S_c=2\mathrm{E}\nu^{1/2}/\sqrt{\mathcal{D}_0}N\ll 1$. In this limit, (4.26) reduces asymptotically to

$$\frac{1}{\nu}+2\pi k_{j\lambda}\sim-\frac{\mathcal{D}_0N^2}{4\nu\mathrm{E}^2}\hat{B}_c\,. \tag{4.38}$$

From (4.37), we then obtain that the multiplier $\beta(\lambda)$ of the NLEP is given in terms of the eigenvalues $k_{j\lambda}$ of $\mathcal{G}_\lambda$ as

$$\beta(\lambda)\equiv\frac{2(\lambda+1-f)}{(\lambda+1)\left(1+\mathcal{D}_0\varphi/(1+2\pi\nu k_{j\lambda})\right)-f}\,; \qquad \varphi\equiv\frac{N^2\alpha}{4\mathrm{E}^2}=\frac{N^2b(1-f)^2}{4f^2\mathrm{E}^2}\,. \tag{4.39}$$

To analyze (4.37) with (4.39), we must calculate the eigenvalues $k_{j\lambda}$ of the Green's matrix $\mathcal{G}_\lambda$ when $\mathcal{D}\gg 1$. This is done by first determining an approximation to the Green's function $G_\lambda(x;x_0)$ and its regular part R_λ satisfying (3.19)

when $\mathcal{D} \gg 1$. For $\mathcal{D} = \mathcal{D}_0/\nu \gg 1$, $\tau = \mathcal{O}(1)$, and $\lambda \neq 0$, we readily obtain that

$$G_\lambda(x;x_0) \sim \frac{\mathcal{D}_0}{4\pi\tau\lambda\nu} + G(x;x_0) + \mathcal{O}(\nu)\,, \qquad R_\lambda \sim \frac{\mathcal{D}_0}{4\pi\tau\lambda\nu} + R + \mathcal{O}(\nu)\,, \qquad R \equiv \frac{1}{4\pi}\left(\log 4 - 1\right)\,,$$

where G is the source-neutral Green's function of (2.8)-(2.9) with regular part R. Therefore, for $\mathcal{D} = \mathcal{D}_0/\nu \gg 1$, $\tau = \mathcal{O}(1)$, and $\lambda \neq 0$, a two-term approximation for the Green's matrix $\mathcal{G}_\lambda$ is

$$\mathcal{G}_\lambda = \frac{1}{\nu}\left(\frac{\mathcal{D}_0 N}{4\pi\tau\lambda}\right)\mathcal{E}_0 + \frac{N}{4\pi}\left(\log 4 - 1\right)\mathcal{E}_0 - \frac{1}{2\pi}\mathcal{G} + \mathcal{O}(\nu)\,. \tag{4.40}$$

Here $\mathcal{E}_0 \equiv \mathbf{e}\mathbf{e}^T/N$ is given in (2.14 a), and $\mathcal{G}$ is the matrix of logarithmic interactions as defined in (2.13).

With this approximation for $\mathcal{G}_\lambda$, the eigenpairs of $\mathcal{G}_\lambda$ for $\nu \ll 1$ are

$$\mathcal{G}_\lambda \mathbf{e} = k_{1\lambda}\mathbf{e}\,, \qquad k_{1\lambda} \sim \frac{\mathcal{D}_0 N}{4\pi\tau\lambda\nu} + \mathcal{O}(1)\,, \tag{4.41 a}$$

$$\mathcal{G}_\lambda \mathbf{b_j} = k_{j\lambda}\mathbf{b_j}\,, \qquad k_{j\lambda} \sim -\frac{1}{2\pi}k_j + \mathcal{O}(\nu)\,, \qquad \mathbf{b_j}^T\mathbf{e} = 0\,, \quad j = 2,\ldots,N\,. \tag{4.41 b}$$

Here k_j for $j = 2,\ldots,N$ are the eigenvalues of $\mathcal{G}$ corresponding to the $N-1$ dimensional subspace perpendicular to $\mathbf{e}$. A key observation is that $k_{1\lambda} = \mathcal{O}(\nu^{-1})$ whereas $k_{j\lambda} = \mathcal{O}(1)$ as $\nu \to 0$ for $j = 2,\ldots,N$.

For the synchronous mode of instability, we simply substitute $k_{1\lambda}$ from (4.41 a) into (4.39). Alternatively, for the competition modes for which $k_{j\lambda} = \mathcal{O}(1)$ for $j = 2,\ldots,N$ when $\mathcal{D} = \mathcal{O}(\nu^{-1})$ and $0 < \tau|\lambda| = \mathcal{O}(1)$, to leading-order we simply neglect the $k_{j\lambda}$ term in (4.39). In this way, we obtain two different NLEP's corresponding to either synchronous or competition instabilities. We summarize our result as follows:

Principal Result 4.3 *For $\varepsilon \to 0$, suppose that the spot locations are such that the Green's matrix $\mathcal{G}$ of (3.13) has a constant row sum. Then, there is an N-spot quasi-equilibrium solution with spots of a common source strength $S_c = 2\mathrm{E}/\sqrt{\mathcal{D}}N$. For $\mathcal{D} = \mathcal{D}_0/\nu \gg 1$ and $\tau = \mathcal{O}(1)$ then, to leading-order in $\nu = -1/\log\varepsilon$, the linear stability of this quasi-equilibrium solution to $\mathcal{O}(1)$ time-scale instabilities is determined by the spectrum of the NLEP (4.37), where $\beta(\lambda)$ in (4.37) has either of the two possible forms*

$$\beta(\lambda) = \beta_s(\lambda) \equiv \frac{2(\lambda+1-f)}{(\lambda+1)\mu(\tau\lambda) - f}\,, \qquad \text{or} \qquad \beta(\lambda) = \beta_c(\lambda) \equiv \frac{2(\lambda+1-f)}{(\lambda+1)\left(1+\mathcal{D}_0\varphi\right) - f}\,, \tag{4.42}$$

corresponding to either the synchronous or competition modes of instability. Here $\mu(\tau\lambda)$ and φ are defined by

$$\mu(\xi) \equiv \frac{N\mathcal{D}_0 + 2\xi\left(\mathcal{D}_0\varphi + 1\right)}{N\mathcal{D}_0 + 2\xi} \qquad \text{and} \quad \varphi \equiv \frac{N^2\alpha}{4\mathrm{E}^2} = \frac{N^2 b(1-f)^2}{4f^2\mathrm{E}^2}\,. \tag{4.43}$$

The discrete eigenvalues of these two NLEP's are the roots of $g(\lambda) = 0$ where

$$g(\lambda) = \mathcal{C}(\lambda) - \mathcal{F}(\lambda)\,, \qquad \mathcal{F}(\lambda) \equiv \frac{\int_0^\infty w\left[\left(L_0-\lambda\right)^{-1}w^2\right]\rho\,d\rho}{\int_0^\infty w^2\rho\,d\rho}\,, \tag{4.44}$$

where $\mathcal{C}(\lambda) \equiv 1/\beta_s(\lambda)$ for the synchronous mode and $\mathcal{C}(\lambda) \equiv 1/\beta_c(\lambda)$ for the competition modes.

Remark 4.1 *The key assumption for the validity of (4.40) is that $0 < \tau|\lambda|\nu/\mathcal{D}_0 \ll 1$. In §4.5 we derive a new NLEP corresponding to the limit $\tau|\lambda|/\mathcal{D} \gg 1$.*

4.4 Analysis of an NLEP

In this sub-section, we give results for the discrete spectrum of the NLEP in (4.37). A primary basic result, proved in Theorem 1.4 in [**44**], is that if $\beta > 0$ is a constant, independent of λ, then $\mathrm{Re}(\lambda) > 0$ if and only if $\beta < 1$. Therefore,

when β is a constant, the stability threshold is precisely $\beta = 1$. However, in our case, $\beta = \beta(\lambda)$ and so determining necessary and sufficient conditions for stability is more challenging.

In Lemma C.1 of Appendix C we prove that if $0 < \beta(0) < 1$ and $1/\beta(\lambda)$ is analytic in $\mathrm{Re}(\lambda) \geq 0$, then the NLEP (4.37) must have a real positive eigenvalue, which establishes instability. Since $\beta_s(0) = 2 > 1$, the instability criterion of Lemma C.1 does not apply to the synchronous mode. However, since $\beta_c(0) < 1$ when $\mathcal{D}_0$ is large enough, we can obtain the following sufficient condition for the instability of the competition modes.

Principal Result 4.4 *For $N > 1$, and under the conditions of Principal Result 4.3, then to leading-order in ν the $N-1$ competition modes are all unstable when*

$$\mathcal{D} > \frac{\mathcal{D}_{0c}}{\nu}\,, \qquad \mathcal{D}_{0c} \equiv \frac{4f^2\mathrm{E}^2}{N^2 b(1-f)}\,, \qquad b \equiv \int_0^\infty w^2 \rho\, d\rho\,. \tag{4.45}$$

Proof To obtain (4.45), we set $\beta_c(0) < 1$ where β_c is defined in (4.42). This yields $\varphi\mathcal{D}_0 > 1 - f$. Upon using (4.43) for φ, we readily obtain (4.45). We remark that since $0 < f < 1$, then $1/\beta_c(\lambda)$ in (4.42) is analytic in $\mathrm{Re}(\lambda) \geq 0$. □

The threshold in (4.45) agrees with the leading-order term in (4.23) as written in (4.25). To leading order in ν, there is a common stability threshold in terms of $\mathcal{D}_0$ for each of the $N-1$ competition modes. As was shown in the explicit two-term result (4.23) and (4.24) of Principal Result 4.2, this degeneracy in the competition instability threshold is, at least partially, broken by the second order term in the expansion. For the case where the Green's matrix has a constant row sum, the second order term in the expansion, which involves the eigenvalues k_j of $\mathcal{G}$ in the subspace orthogonal to $\mathbf{e}$, depends on the locations of the spots. However, for many symmetric quasi-equilibrium patterns such as when spots are centered at the vertices of platonic solids, these eigenvalues typically are also degenerate (see the last column in Table 1 of §5 below).

The NLEP of (4.37), where β has either of the two forms in (4.42), has a bi-quadratic dependence on λ instead of the bi-linear dependence as derived in the pioneering NLEP analyses of [**44**], [**46**], and [**48**], for the Gierer-Meinhardt, Gray-Scott, and Schnakenburg RD systems in two space dimensions. As such, we need to extend this previous NLEP stability theory. The following new result is central to the analysis of (4.37).

Principal Result 4.5 *Consider the discrete eigenvalues λ of the NLEP (4.37), where the multiplier $\beta(\lambda)$ of the nonlocal term is a rational function in λ of at most degree 2 given by*

$$\beta(\lambda) = \frac{a_1 + b_1\lambda + c_1\lambda^2}{a_2 + b_2\lambda + c_2\lambda^2}\,, \tag{4.46}$$

where a_1, a_2, b_1, and b_2, are positive constants and $c_1 \geq 0$ and $c_2 \geq 0$. Then,

- *(I) if $c_1 = c_2 = 0$ and $1 < a_1/a_2 < b_1/b_2$, we have $Re(\lambda) < 0$;*
- *(II) if $c_1 = c_2 = 0$, $a_1/a_2 < b_1/b_2$, but $a_1/a_2 < 1$, there is exactly one eigenvalue in $Re(\lambda) > 0$, and it is real;*
- *(III) if $c_1 > 0$, $c_2 > 0$, $a_1/a_2 > 1$, and $a_1/a_2 > c_1/c_2$, together with $T_1 \geq 0$ and $T_2 \geq 0$, where*

$$T_1 \equiv c_1 b_1\,(c_2 b_1 - c_1 b_2) + c_1^2\,(c_1 a_2 - a_1 c_2)\,, \qquad T_2 \equiv a_1 b_1\,(a_1 b_2 - a_2 b_1) + a_1^2\,(c_1 a_2 - a_1 c_2)\,, \tag{4.47}$$

  the number M of eigenvalues in $Re(\lambda) > 0$ for the NLEP (4.37) with (4.46) is either $M = 0$ or $M = 2$.
- *(IV) if $c_1 > 0$, $c_2 > 0$, and $a_1/a_2 > 1 > c_1/c_2$, with $T_2 \geq 0$ and $T_1 < 0$, then the number M of eigenvalues in $Re(\lambda) > 0$ for the NLEP (4.37) with (4.46) is either $M = 0$ or $M = 2$.*

Proof The eigenvalues of the NLEP are the roots of $g(\lambda) = 0$, where $g(\lambda)$ is defined in (4.44). We determine the number M of zeroes of $g(\lambda)$ in $\mathrm{Re}(\lambda) > 0$ by calculating the winding number of g over the counterclockwise contour composed of the imaginary axis $-iR_c \le \mathrm{Im}\lambda \le iR_c$ and the semi-circle Γ_{R_c}, given by $|\lambda| = R_c > 0$, for $-\pi/2 \le \arg\lambda \le \pi/2$. Assuming that there are no zeroes of $g(\lambda)$ on the imaginary axis, we let $R_c \to \infty$ and use the argument principle to determine the number of zeroes of $g(\lambda)$ in the right half-plane. In (4.44), the function $\mathcal{F}(\lambda)$ is analytic in $\mathrm{Re}(\lambda) > 0$, except at the simple pole $\lambda = \sigma_0 > 0$, where σ_0 is the unique positive eigenvalue of the local operator L_0 (see Theorem 2.12 of [**18**]). On the semi-circle Γ_{R_c}, we have $|\mathcal{F}(\lambda)| = \mathcal{O}\left(1/|\lambda|\right)$. Moreover, $|\mathcal{C}(\lambda)| \equiv |1/\beta(\lambda)|$ is bounded on Γ_{R_c} as $R_c \to \infty$ and is analytic in $\mathrm{Re}(\lambda) > 0$. Therefore, there is no change in the argument of g over Γ_{R_c} as $R_c \to \infty$. Then, using $g(\overline{\lambda}) = \overline{g(\lambda)}$, and assuming that there are no zeros of $g(\lambda)$ on the imaginary axis, we obtain that the number M of zeroes of $g(\lambda) = 0$ in $\mathrm{Re}(\lambda) > 0$ is

$$M = 1 + \frac{1}{\pi}\left[\arg g\right]_{\Gamma_I}\,, \tag{4.48}$$

where $\left[\arg g\right]_{\Gamma_I}$ denotes the change in the argument of g along the semi-infinite imaginary axis $\Gamma_I = i\lambda_I$ with $0 \le \lambda_I < \infty$, traversed in the downwards direction.

To calculate $\left[\arg g\right]_{\Gamma_I}$ we let $\lambda = i\lambda_I$ in (4.44) and decompose $g(i\lambda_I) = g_R(\lambda_I) + ig_I(\lambda_I)$ and $\mathcal{F}(i\lambda_I) = \mathcal{F}_R(\lambda_I) + i\mathcal{F}_I(\lambda_I)$ to obtain

$$\begin{aligned} g_R(\lambda_I) &= \mathcal{C}_R(\lambda_I) - \mathcal{F}_R(\lambda_I)\,, \qquad \mathcal{F}_R(\lambda_I) \equiv \frac{\int_0^\infty \rho w L_0\left[L_0^2 + \lambda_I^2\right]^{-1} w^2\,d\rho}{\int_0^\infty \rho w^2\,d\rho}\,, \\ g_I(\lambda) &= \mathcal{C}_I(\lambda_I) - \mathcal{F}_I(\lambda_I)\,, \qquad \mathcal{F}_I(\lambda_I) \equiv \lambda_I\,\frac{\int_0^\infty \rho w\left[L_0^2 + \lambda_I^2\right]^{-1} w^2\,d\rho}{\int_0^\infty \rho w^2\,d\rho}\,. \end{aligned} \tag{4.49}$$

Since $\mathcal{C}(\lambda) = 1/\beta(\lambda)$, where $\beta(\lambda)$ is given in (4.46), we calculate that

$$\mathcal{C}_R(\lambda_I) \equiv \frac{a_1a_2 + \lambda_I^2\left(b_1b_2 - c_1a_2 - c_2a_1\right) + c_1c_2\lambda_I^4}{\left(a_1 - c_1\lambda_I^2\right)^2 + \lambda_I^2b_1^2}\,, \qquad \mathcal{C}_I(\lambda_I) \equiv \frac{\lambda_I\left[\left(b_2a_1 - b_1a_2\right) + \lambda_I^2\left(c_2b_1 - c_1b_2\right)\right]}{\left(a_1 - c_1\lambda_I^2\right)^2 + \lambda_I^2b_1^2}\,. \tag{4.50}$$

In §2 of [**42**] it was proved that $\mathcal{F}_R(\lambda_I)$ and $\mathcal{F}_I(\lambda_I)$ have the following local behavior as $\lambda_I \to 0$:

$$\mathcal{F}_R(\lambda_I) \sim 1 - \kappa_c\lambda_I^2 + \cdots\,, \qquad \kappa_c \equiv \frac{\int_0^\infty \rho\left[L_0^{-1}w\right]^2\,d\rho}{\int_0^\infty \rho w^2\,d\rho}\,; \qquad \mathcal{F}_I(\lambda_I) \sim \lambda_I/2 + \mathcal{O}(\lambda_I^3)\,. \tag{4.51 a}$$

Moreover, from §2 of [**42**] the following global behavior of $\mathcal{F}_R(\lambda_I)$ and $\mathcal{F}(\lambda_I)$ was established:

$$\mathcal{F}_R'(\lambda_I) < 0\,, \qquad \mathcal{F}_I(\lambda_I) > 0\,, \quad \text{for} \quad \lambda_I > 0\,, \tag{4.51 b}$$

with $\mathcal{F}_R \to 0$ and $\mathcal{F}_I \to 0$ as $\lambda_I \to +\infty$.

We now prove the first statement (I). We calculate $g_R(0) = a_2/a_1 - 1 < 0$, $g_I(0) = 0$ with $g_R > 0$ and $g_I \to 0$ as $\lambda_I \to +\infty$. Then, since $c_1 = c_2 = 0$ and $1 < a_1/a_2 < b_1/b_2$, we conclude from (4.50) that $\mathcal{C}_I(\lambda_I) < 0$ for $\lambda_I > 0$. Since $\mathcal{F}_I(\lambda_I) > 0$ for $\lambda_I > 0$, we obtain that $g_I < 0$ for all $\lambda_I > 0$. It follows that $\left[\arg g\right]_{\Gamma_I} = -\pi$ and so $M = 0$ from (4.48).

The proof of the second statement (II) is identical, except that $g_R(0) = a_2/a_1 - 1 > 0$ and $g_I(0) = 0$. Therefore, $\left[\arg g\right]_{\Gamma_I} = 0$ and so $M = 1$ from (4.48). Lemma C.1 of Appendix C proves that this unique unstable eigenvalue is real.

To prove the third statement (III), we first note that $g(0) = a_2/a_1 - 1 < 0$ with $g_R > 0$ and $g_I \to 0$ as $\lambda_I \to +\infty$. We then derive a condition to ensure that $\mathcal{C}_R(\lambda_I)$ is monotone increasing for $\lambda_I > 0$. Under such a condition, then since $\mathcal{F}_R(\lambda_I)$ is monotone decreasing for $\lambda_I > 0$, it follows that there is a unique root $\lambda_I^\star$ to $g_R(\lambda_I) = 0$. If $g_I\left(\lambda_I^\star\right) < 0$, then $\left[\arg g\right]_{\Gamma_I} = -\pi$, and so $M = 0$ from (4.48). Alternatively, if $g_I\left(\lambda_I^\star\right) > 0$, then $\left[\arg g\right]_{\Gamma_I} = \pi$ and $M = 2$ from (4.48).

From (4.50) a necessary condition for the monotonicity of $\mathcal{C}_R(\lambda_I)$ is that $a_2/a_1 < c_2/c_1$. To derive a sufficient

condition, we let $\lambda_I = \sqrt{\xi}$ and define $\mathcal{T}(\xi) \equiv \mathcal{C}_R(\sqrt{\xi})$. We differentiate (4.50) to obtain that $\mathcal{C}_R'(\sqrt{\xi}) = 2\sqrt{\xi}\mathcal{T}'(\xi)$, where $\mathcal{T}'(\xi)$ is given by

$$\mathcal{T}'(\xi) = \frac{\mathcal{P}(\xi)}{\left[(a_1 - c_1\xi)^2 + \xi b_1^2\right]^2}\,, \qquad \mathcal{P}(\xi) \equiv T_1\xi^2 + 2c_1a_1\left(c_2a_1 - c_1a_2\right)\xi + T_2\,. \tag{4.52}$$

Here T_1 and T_2 are defined in (4.47). Since the coefficient of ξ in $\mathcal{P}(\xi)$ is necessarily positive, it follows that $\mathcal{C}_R'(\lambda_I) > 0$ on $\lambda_I > 0$ if and only if $T_1 \geq 0$ and $T_2 \geq 0$. To establish the necessity of this inequalities, we note that if $T_2 < 0$ then $\mathcal{C}_R'(0) < 0$, which implies that $\mathcal{C}_R'(\lambda_I)$ is locally decreasing on the range $0 < \lambda_I \ll 1$. Moreover, if $T_1 < 0$, then $\mathcal{C}_R(\lambda_I)$ approaches its limiting value c_2/c_1 from above as $\lambda_I \to \infty$, so that $\mathcal{C}_R(\lambda_I)$ is not monotone increasing for all $\lambda_I > 0$.

The proof of the fourth statement (IV) is similar. We have $\mathcal{C}_R(0) = a_2/a_1 < 1$ and $\mathcal{C}_R(\infty) = c_2/c_1 > 1$. Since $T_2 \geq 0$ and $T_1 < 0$, it follows from (4.52) that $\mathcal{P}(0) > 0$, $\mathcal{P}'(0) > 0$ with $\mathcal{P}(\xi) \to -\infty$ as $\xi \to +\infty$. Thus, there is a unique point $\lambda_I^\star > 0$ with $\mathcal{C}_R'(\lambda_I^\star) = 0$ for which $\mathcal{C}_R(\lambda_I^\star) > \mathcal{C}_R(\infty) = c_2/c_1 > 1$, with the property that $\mathcal{C}_R'(\lambda_I) < 0$ for $\lambda_I > \lambda_I^\star$ and $\mathcal{C}_R'(\lambda_I) > 0$ for $0 < \lambda_I < \lambda_I^\star$. Therefore, on the range of λ_I for which $0 < \mathcal{C}_R < 1$, it follows that $\mathcal{C}_R(\lambda_I)$ is monotone increasing in λ_I. Since $\mathcal{C}_R(0) < \mathcal{F}_R(0) = 1$ and $\mathcal{F}_R'(\lambda_I) < 0$ for $\lambda_I > 0$, it is only on the range where $0 < \mathcal{C}_R < 1$ that $g_R(\lambda_I) = 0$ can have a root. Define λ_I^- by $\mathcal{C}_R(\lambda_I^-) = 1$. Then, since $g_R(0) < 0$, $g_R(\lambda_I^-) > 0$, and $g_R'(\lambda_I) > 0$ on $0 < \lambda_I < \lambda_I^-$, it follows that there is a unique root to $g_R(\lambda_I) = 0$ on $0 < \lambda_I < \lambda_I^-$. Hence, from (4.48). we conclude that either $M = 0$ or $M = 2$. □

Upon applying Principal Result 4.5 to the competition instability modes, we obtain the following result:

Principal Result 4.6 *Consider the discrete eigenvalues λ of the NLEP (4.37) for the competition instability modes where $\beta(\lambda) = \beta_c(\lambda)$ is given in (4.42). Then, if $0 < \mathcal{D}_0\varphi < 1 - f$ where φ is defined in (4.43), we conclude that $Re(\lambda) < 0$. Moreover, on the range $\mathcal{D}_0\varphi > 1 - f$, there is exactly one eigenvalue in $Re(\lambda) > 0$ and it is real.*

Proof For the competition multiplier $\beta_c(\lambda)$, we identify in (4.46) that $a_1 = 2(1 - f)$, $a_2 = 1 - f + \mathcal{D}_0\varphi$, $b_1 = 2$, $b_2 = 1 + \mathcal{D}_0\varphi$, and $c_1 = c_2 = 0$. We then calculate that

$$\frac{a_1}{a_2} = \frac{2(1-f)}{(1-f) + \mathcal{D}_0\varphi}\,, \qquad \frac{a_1}{a_2} - \frac{b_1}{b_2} = \frac{-2f\mathcal{D}_0\varphi}{(1 + \mathcal{D}_0\varphi)\,(1 - f + \mathcal{D}_0\varphi)} < 0\,,$$

so that $a_1/a_2 < b_1/b_2$. On the range $0 < \mathcal{D}_0\varphi < 1 - f$, we have $a_1/a_2 > 1$, so that (I) of Principal Result 4.5 yields that $\mathrm{Re}(\lambda) < 0$. On the complementary range where $\mathcal{D}_0\varphi > 1 - f$, we have $a_1/a_2 < 1$ so that from (II) of Principal Result 4.5 there is one unstable eigenvalue and it is real. □

Therefore, the critical value $\mathcal{D}_0\varphi = (1 - f)$ provides a distinct threshold between the stability and instability of the competition modes. There can be no Hopf bifurcations associated with these modes on the range $\mathcal{D} = \mathcal{O}(\nu^{-1})$. Next, we analyze the discrete eigenvalues of the NLEP for the synchronous mode. We obtain the following result:

Principal Result 4.7 *Consider the discrete eigenvalues λ of the NLEP (4.37) for the synchronous instability mode where $\beta(\lambda) = \beta_s(\lambda)$ is given in (4.42). If $N\mathcal{D}_0 > \tau f\left[1 + \sqrt{-3 + 4/f}\right]$, then the number M of unstable eigenvalues is either $M = 0$ or $M = 2$. Moreover, if $N\mathcal{D}_0 < \tau f\left[1 + \sqrt{-3 + 4/f}\right]$ and $\mathcal{D}_0\varphi > 1$, then $M = 0$ or $M = 2$. Finally, $\lambda = 0$ is never an eigenvalue, and so any instability generated by an eigenvalue crossing into $Re(\lambda) > 0$ must be a result of a Hopf bifurcation.*

Proof The fact that $\lambda = 0$ is never an eigenvalue is immediate since $\beta_c(0) = 2 > 1$ for all parameter values. To prove the threshold condition on $N\mathcal{D}_0$, we simply determine the range of parameters for which (III) of Principal Result 4.5 holds. Upon comparing $\beta_c(\lambda)$, as given in (4.42) with the general form (4.46), we identify

$$a_1 = 2(1-f)N\mathcal{D}_0\,, \quad b_1 = 2\zeta\,, \quad c_1 = 4\tau\,, \quad a_2 = N\mathcal{D}_0(1-f)\,, \quad b_2 = \zeta + 2\tau\mathcal{D}_0\varphi\,, \quad c_2 = 2\tau(\mathcal{D}_0\varphi + 1)\,,$$

where we have defined $\zeta \equiv N\mathcal{D}_0 + 2\tau(1-f)$. We calculate that $a_1/a_2 = 2 > 1$ and $c_1/c_2 - a_1/a_2 = -2\mathcal{D}_0\varphi/(\mathcal{D}_0\varphi+1) < 0$, so that $c_1/c_2 < a_1/a_2$. To establish the sign of T_2 in (4.47) we calculate

$$\frac{b_1 b_2}{a_1 c_2}\left(\frac{a_1}{a_2} - \frac{b_1}{b_2}\right) + \left(\frac{c_1}{c_2} - \frac{a_1}{a_2}\right) = \frac{2\mathcal{D}_0\varphi}{\mathcal{D}_0\varphi+1}\left(\frac{\zeta}{(1-f)N\mathcal{D}_0} - 1\right) = \frac{2\mathcal{D}_0\varphi}{\mathcal{D}_0\varphi+1}\left[\frac{f}{1-f} + \frac{2\tau}{N\mathcal{D}_0}\right] > 0\,.$$

This shows that that $T_2 > 0$ unconditionally, and so $\mathcal{C}_R'(0) > 0$. From similar simple algebraic manipulations, we conclude that $T_1 > 0$ if and only if $\mathcal{S}(\xi) > 0$ where

$$\mathcal{S}(\xi) \equiv \xi^2 - 2\tau f\xi + 4\tau^2(-f + f^2)\,, \qquad \xi \equiv N\mathcal{D}_0\,. \tag{4.53}$$

We obtain $\mathcal{S}'(0) < 0$, $\mathcal{S} \to +\infty$ as $\xi \to \infty$, and $\mathcal{S}(0) < 0$ since $0 < f < 1$. Therefore, $\mathcal{S}(\xi) > 0$ if ξ is larger than its unique positive root in $\xi > 0$. In this way, $\mathcal{S}(\xi) > 0$ if $N\mathcal{D}_0 > \tau f\left(1 + \sqrt{-3 + 4/f}\right)$. For $N\mathcal{D}_0$ above this threshold, (III) of Principal Result 4.5 holds and we obtain either $M = 0$ or $M = 2$. To prove that $M = 0$ or $M = 2$ when $N\mathcal{D}_0 < \tau f\left(1 + \sqrt{-3 + 4/f}\right)$ but $\mathcal{D}_0\varphi > 1$ we appeal to (IV) of Principal Result 4.5. Since $T_2 > 0$ and $T_1 < 0$ and $\mathcal{C}_R(\infty) = c_2/c_1 = (\mathcal{D}_0\varphi + 1)/2 > 1$ when $\mathcal{D}_0\varphi > 1$, we obtain from (IV) that $M = 0$ or $M = 2$. □

Next, we determine numerically any Hopf bifurcations associated with the synchronous instability mode as we sweep over the parameters $0 < f < 1$, E > 0, and $\mathcal{D}_0 > 0$ for a fixed integer $N \geq 1$, where $\tau = 1/f^2$. First we compute the functions $\mathcal{F}_R(\lambda_I)$ and $\mathcal{F}_I(\lambda_I)$ numerically as in [**42**]. Then, for the range of $\mathcal{D}_0$ for which Principal Result 4.7 applies, we need only evaluate the sign of $g_I(\lambda_I)$ at the unique root of $g_R(\lambda_I) = 0$ in order to determine whether $M = 0$ or $M = 2$. On the complementary range of $\mathcal{D}_0$ for which $C_R'(0) < 0$ and $C_R(\lambda_I) \to c_2/c_1$ from below as $\lambda_I \to \infty$, we need only numerically ascertain whether $g_R = 0$ has multiple roots and then calculate the sign of g_I at these roots in order to determine the winding number. In this way, the use of the winding number reduces the stability problem to a rather simple numerical problem involving root finding.

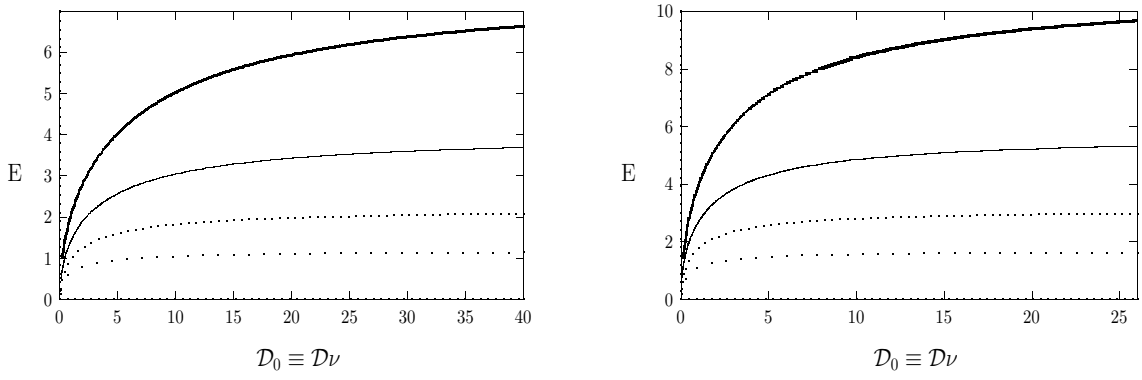

FIGURE 12. Plot of the numerically computed Hopf bifurcation threshold of E versus $\mathcal{D}_0$ for the synchronous instability mode, corresponding to the NLEP (4.37) with $\beta(\lambda) = \beta_s(\lambda)$ as given in (4.42), on the range $\mathcal{D}_0\varphi > 1 - f$. The values of f are $f = 0.4$ (heavy solid curves), $f = 0.5$ (solid curves), $f = 0.6$ (dotted curves), and $f = 0.7$ (widely spaced dots). The left and right panels are for $N = 1$ and $N = 2$ spots, respectively.

Our numerical results from the NLEP show that the synchronous mode does not undergo any Hopf bifurcations on the range $\mathcal{D}_0\varphi < 1-f$ where the competition modes for $N \geq 2$ are stable. However, on the range $\mathcal{D}_0\varphi > 1-f$, there is a Hopf bifurcation for the synchronous mode as E is decreased below a critical threshold. Since there are no competition instabilities for a single spot, this critical threshold sets the instability threshold for a one spot solution on the range $\mathcal{D} = \mathcal{O}(\nu^{-1})$. In Fig. 12 we plot the numerically computed Hopf bifurcation threshold of E versus $\mathcal{D}_0$ at four different values of f for both $N = 1$ (left panel) and $N = 2$ (right panel) spots. If we are below any one of the curves in Fig. 12, then the NLEP (4.37) for the synchronous mode has two unstable eigenvalues. The left end of these curves is for a value of $\mathcal{D}_0$ slightly above the critical threshold $\mathcal{D}_0\varphi > 1-f$. Alternatively, the far right end of these curves approximates the stability threshold for the shadow limit $\mathcal{D} \to +\infty$ of (1.2). A Hopf bifurcation analysis for the shadow limit of the Gierer-Meinhardt RD model in multi-space dimensions was done previously in [**42**].

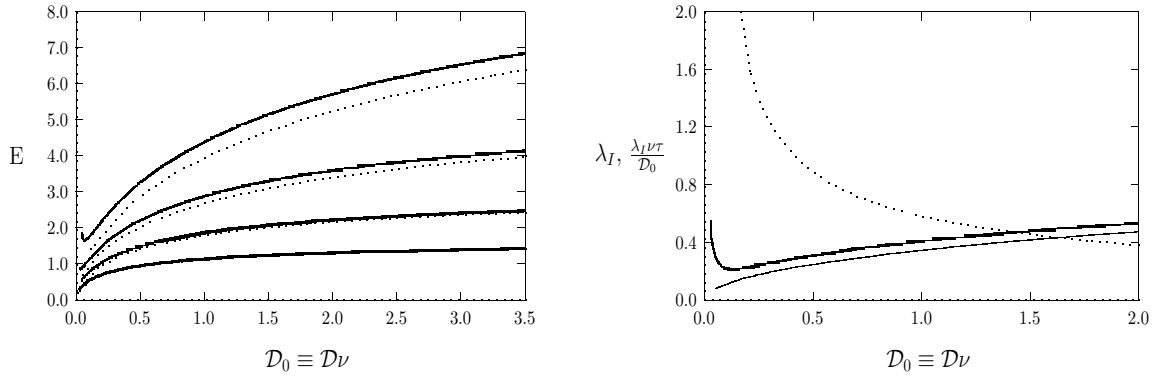

FIGURE 13. Left panel: The Hopf bifurcation threshold E versus $\mathcal{D}_0 = \mathcal{D}\nu$ (dashed curves) for the synchronous mode, as computed from the NLEP, is compared with corresponding full results computed from (3.31) of Principal Result 3.3 (heavy solid curves) for $\varepsilon = 0.06$. The pair of curves from top to bottom are for $f = 0.4$, $f = 0.5$, $f = 0.6$, and $f = 0.7$. The results from the NLEP agree very favorably for $f = 0.5$, $f = 0.6$, and $f = 0.7$, except when $\mathcal{D}_0$ is small, with a less favorable agreement when $f = 0.4$. Right panel: for $\varepsilon = 0.06$ and $f = 0.5$, the NLEP Hopf bifurcation frequency λ_I versus $\mathcal{D}_0$ (solid curve), on the zoomed range $\mathcal{D}_0 < 2$, is compared with the corresponding Hopf frequency as computed from (3.31) of Principal Result 3.3 (heavy solid curve). The two curves agree rather well except when $\mathcal{D}_0$ is small. The dashed curve is $\lambda_I\nu\tau/\mathcal{D}_0$ as computed from (3.31). Recall that the NLEP is formally valid only when $\lambda_I\nu\tau/\mathcal{D}_0$ is asymptotically small.

For $\varepsilon = 0.06$ and for the four values of f as in the right panel of Fig. 12, in the left panel of Fig. 13 we compare the 2-spot NLEP Hopf bifurcation threshold with corresponding results for the synchronous Hopf threshold, as computed from (3.31) of Principal Result 3.3 (heavy solid curves), which is accurate to all orders in ν. Although the NLEP theory is based on a leading order in ν analysis under the assumption that $\tau\lambda_I\nu/\mathcal{D}_0 \ll 1$, the left panel of Fig. 13 shows that the NLEP Hopf bifurcation threshold at $\varepsilon = 0.06$ still agrees rather well with results computed from (3.31) up to $\mathcal{D}_0 = 0.5$. For $\varepsilon = 0.06$ and $f = 0.5$, in the right panel of Fig. 13 we compare the NLEP Hopf bifurcation frequency λ_I versus $\mathcal{D}_0$ with corresponding results computed from (3.31) (heavy solid curve). The two curves agree rather well except when $\mathcal{D}_0$ is small. The discrepancy between results from the NLEP theory and from (3.31) as $\mathcal{D}_0$ decreases is a result of the fact that $\tau\lambda_I\nu/\mathcal{D}_0$ is no longer small, which invalidates the NLEP analysis.

4.5 A New NLEP and an Anomalous Scaling Law for a Hopf Bifurcation

The derivation of the leading-order-in-ν NLEP of Principal Result 4.3 is valid in the small source-strength limit $S_c = 2\mathrm{E}/(\sqrt{\mathcal{D}}N) \ll 1$ only when $\tau|\lambda|/\mathcal{D} \ll 1$. For $\mathcal{D} = \mathcal{D}_0/\nu$ and $\mathrm{E} = \mathcal{O}(1)$, where these two conditions are

satisfied, the numerical computations in §4.4 of the spectrum of this leading-order NLEP showed that there are no Hopf bifurcations on the parameter range $0 < \mathcal{D}_0\theta < 1 - f$.

In this subsection, we derive a new NLEP that is still valid in the small source strength limit $S_c = 2\mathrm{E}/(\sqrt{\mathcal{D}}N) \ll 1$, but which applies to the regime $\tau|\lambda|/\mathcal{D} \gg 1$. This limit will correspond to $\mathcal{D} = \mathcal{D}_0/\nu \ll 1$ where $\mathcal{D}_0 = \mathcal{O}(\mathrm{E}^2) \ll 1$ as $\mathrm{E} \to 0$. To analyze this parameter regime it is convenient to introduce the new variables $\hat{\mathcal{D}}_0$ and $\hat{\tau}$ by

$$\hat{\mathcal{D}}_0 \equiv \mathcal{D}_0/\mathrm{E}^2 = \mathcal{O}(1)\,, \qquad \hat{\tau} \equiv \nu\tau/\mathrm{E}^2 = \nu/(f^2\mathrm{E}^2) \gg 1\,. \tag{4.54}$$

Since $\tau|\lambda|/\mathcal{D} = \hat{\tau}|\lambda|/\hat{\mathcal{D}}_0 \gg 1$, the interaction between spots is negligible and the Green's matrix $\mathcal{G}_\lambda$ reduces asymptotically to a multiple of the identity matrix, i.e. $\mathcal{G}_\lambda \sim R_\lambda I$. Therefore, $k_{j\lambda} \sim R_\lambda$ for $j = 1, \ldots, N$, and (4.39) becomes

$$\beta(\lambda) \equiv \frac{2(\lambda + 1 - f)}{(\lambda+1)\left(1 + \hat{\mathcal{D}}_0\varphi_0/(1 + 2\pi\nu R_\lambda)\right) - f}\,; \qquad \varphi_0 \equiv \frac{N^2 b(1-f)^2}{4f^2}\,. \tag{4.55 a}$$

Upon setting $\tau|\lambda|/\mathcal{D} = \hat{\tau}|\lambda|/\hat{\mathcal{D}}_0 \gg 1$ in (3.25) of Lemma 3.1, and labeling γ as Euler's constant, we get

$$2\pi R_\lambda \sim -\frac{1}{2}\log(\lambda\hat{\tau}) + \hat{\alpha}\,, \qquad \hat{\alpha} \equiv \log\left(2\sqrt{\hat{\mathcal{D}}_0}\right) - \gamma\,. \tag{4.55 b}$$

Next, we choose a scaling for $\hat{\tau}$, and hence E, in terms of ε so that $2\pi\nu R_\lambda$ is $\mathcal{O}(1)$ as $\varepsilon \to 0$. It is on such a scaling regime that a Hopf bifurcation is obtained. As such, we consider the anomalous scaling law

$$\hat{\tau} = \varepsilon^{-\tau_c}\,, \tag{4.56}$$

for some $\tau_c = \mathcal{O}(1)$ to be determined. This implies that $\mathrm{E} = \mathcal{O}(\nu^{1/2}\varepsilon^{\tau_c/2})$ and $\mathcal{D} = \hat{\mathcal{D}}_0/\nu = \mathcal{O}(\varepsilon^{\tau_c})$. Since we require that $\mathcal{O}(\varepsilon^2) \ll \mathcal{D} \ll \mathcal{O}(1)$, we must restrict τ_c to the interval $0 < \tau_c < 2$. Then, from (4.37), (4.55), and (4.56), we obtain a new type of NLEP, which we formulate as follows:

Principal Result 4.8 *Let $\varepsilon \to 0$, $\nu = -1/\log\varepsilon$ and suppose that the spots have a common source strength $S_c = 2\mathrm{E}/(\sqrt{\mathcal{D}}N) \ll 1$. Let $\mathcal{D}$ and* E *approach zero as $\varepsilon \to 0$ with the scaling behavior*

$$\mathcal{D} = \frac{\varepsilon^{\tau_c}}{f^2}\hat{\mathcal{D}}_0\,, \qquad \mathrm{E} = \frac{\sqrt{\nu}}{f}\varepsilon^{\tau_c/2}\,, \tag{4.57}$$

in terms of a anomalous scaling parameter τ_c in the interval $0 < \tau_c < 2$. Then, any discrete eigenvalue λ, with $|\lambda| \gg \mathcal{O}(\varepsilon^{\tau_c})$, of the NLEP (4.37) with multiplier (4.55) is a root of $g(\lambda) = 0$, where

$$g(\lambda) = \mathcal{C}_0(\lambda) - \mathcal{F}(\lambda)\,, \qquad \mathcal{F}(\lambda) \equiv \frac{\int_0^\infty w\left[(L_0 - \lambda)^{-1} w^2\right]\rho\,d\rho}{\int_0^\infty w^2\rho\,d\rho}\,, \tag{4.58 a}$$

and

$$\mathcal{C}_0(\lambda) \equiv [\beta(\lambda)]^{-1} \equiv \frac{1}{2} + \frac{(\lambda+1)}{2(\lambda+1-f)}\left[\frac{\hat{\mathcal{D}}_0\varphi_0}{1 - \tau_c/2 + \nu\mathcal{K}_0}\right]\,, \qquad \mathcal{K}_0 \equiv -\frac{1}{2}\log\lambda + \hat{\alpha}\,. \tag{4.58 b}$$

Here $\hat{\alpha}$ and φ_0 are defined in (4.55).

On the positive real λ axis, we recall from (C.1) of Appendix C that $\mathcal{F}(0) = 1$, $\mathcal{F}(\lambda)$ is monotone increasing on $0 < \lambda < \sigma_0$ and $\mathcal{F}(\lambda) \to +\infty$ as $\lambda \to \sigma_0^-$, where σ_0 is the unique positive eigenvalue of L_0. Therefore, since $\mathcal{C}_0(\lambda) > 1$ for $\mathcal{O}(\varepsilon^{\tau_c}) \ll \lambda \ll 1$ when $\tau_c > 2\left(1 - \hat{\mathcal{D}}_0\varphi_0/(1-f)\right)$, it follows that the NLEP of (4.58) must have a positive real eigenvalue in $\lambda > \mathcal{O}(\varepsilon^{\tau_c})$ on this range of τ_c. This observation suggests that the NLEP (4.58) should have a low

frequency Hopf bifurcation with $\lambda = i\lambda_I$ and $0 < \lambda_I \ll 1$ when $\tau_c \approx 2\left(1 - \hat{\mathcal{D}}_0\varphi_0/(1-f)\right)$. This Hopf bifurcation is characterized asymptotically as follows:

Principal Result 4.9 *Under the conditions of Principal Result 4.8, and for the parameter regime $0 < \mathcal{D}_0\varphi < 1 - f$, the NLEP (4.58) has a low frequency Hopf bifurcation at the critical values τ_c and λ given in terms of $\nu = -1/\log\varepsilon$ by*

$$\tau_c \sim \tau_{c0} - \nu\log\nu + \nu\left(2\hat{\alpha} - \log\lambda_{I0}\right) + \mathcal{O}(\nu^2)\,; \qquad \lambda \sim i\nu\lambda_{I0} + \mathcal{O}(\nu^3)\,, \tag{4.59 a}$$

where τ_{c0} and λ_{I0} are given explicitly by

$$\tau_{c0} \equiv 2\left(1 - \frac{\hat{\mathcal{D}}_0\varphi_0}{1-f}\right)\,, \qquad \lambda_{I0} \equiv \frac{\pi}{4\hat{\mathcal{D}}_0\varphi_0}(1-f)^2\,, \qquad \varphi_0 \equiv \frac{N^2 b(1-f)^2}{4f^2}\,. \tag{4.59 b}$$

Here $\hat{\alpha} \equiv \log\left(2\sqrt{\hat{\mathcal{D}}_0}\right) - \gamma$ and γ is Euler's constant.

Proof We need only find a critical value of τ_c for which there is a purely imaginary root to $g(\lambda) = 0$ of the form $\lambda = i\nu\lambda_I$ with $\lambda_I = \mathcal{O}(1)$ as $\nu \to 0$. From the local behavior of $\mathcal{F}(\lambda_I)$, as given in (4.51 *a*), we obtain that $\mathcal{F}(i\nu\lambda_I) \sim 1 + i\nu\lambda_I/2 + \mathcal{O}(\nu^2)$. Upon using this limiting behavior in (4.58), we obtain that $g(\lambda) = 0$ when λ_I and τ_c satisfy the complex-valued equation

$$i\lambda_I\nu\left[\hat{\mathcal{D}}_0\varphi_0 + \left(\frac{\tau_c}{2} - 1\right) - \nu\mathcal{K}_0\right] + \hat{\mathcal{D}}_0\varphi_0 + \left(\frac{\tau_c}{2} - 1\right)(1-f) - (1-f)\nu\mathcal{K}_0 = \\ 2\left(i\lambda_I\nu + 1 - f\right)\left(1 - \frac{\tau_c}{2} + \nu\mathcal{K}_0\right)\left(\frac{i\lambda_I\nu}{2} + \mathcal{O}(\nu^2)\right)\,, \tag{4.60 a}$$

where

$$\mathcal{K}_0 = -\frac{i\pi}{4} - \frac{1}{2}\log\nu - \frac{1}{2}\log\lambda_I + \hat{\alpha}\,. \tag{4.60 b}$$

By taking the real and imaginary parts of (4.60 *a*) we obtain to leading order in ν that $\tau_c \sim \tau_{c0} + o(1)$ and $\lambda_I \sim \lambda_{I0} + o(1)$, where

$$\left(\frac{\tau_{c0}}{2} - 1\right)(1-f) + \hat{\mathcal{D}}_0\theta_0 = 0\,, \qquad \lambda_{I0}\left[\left(\frac{\tau_{c0}}{2} - 1\right)(2-f) + \hat{\mathcal{D}}_0\theta_0\right] = -\frac{\pi}{4}(1-f)\,.$$

The solution to this limiting system yields τ_{c0} and λ_{I0} as given in (4.59 *b*). The calculation of the higher order terms in ν for a root to (4.60) is straightforward but tedious. We expand τ_c and λ_I as

$$\tau_c = \tau_{c0} - \nu\log\nu + \nu\tau_{c2} + \mathcal{O}(\nu^2)\,, \qquad \lambda_I = \lambda_{I0} + \nu\lambda_{I1} + \mathcal{O}(\nu^2)\,,$$

and substitute the expansion into (4.60). By solving the real and imaginary parts of the resulting expressions for $\nu \ll 1$ we obtain after some lengthy algebra that $\lambda_{I1} = 0$ and $\tau_{c2} = 2\hat{\alpha} - \log\lambda_{I0}$. This yields (4.59 *b*). □

From (4.59 *b*), we observe that $\tau_{c0} < 2$ and that $\tau_{c0} > 0$ when $\hat{\mathcal{D}}_0\varphi_0 = \mathcal{D}_0\varphi < 1 - f$. In this regime, (4.57) and (4.59) provide a parametric description of a curve emanating from the origin in the $\mathcal{D}$, E parameter plane for which the linearization of a common source-strength quasi-equilibrium solution has a complex conjugate pair of eigenvalues.

platonic solid	number of vertices	k_1	$k_{j^\star}$	M
tetrahedron	4	1.4712	-0.49041	1
octahedron	6	2.0794	0.0	2
cube/hexahedron	8	2.5959	0.34657	3
icosahedron	12	3.6010	0.38288	3
dodecahedron	20	5.3617	0.76575	5

Table 1. Numerical results for the spectrum of the Green's matrix $\mathcal{G}$ corresponding to a quasi-equilibrium pattern where the spots are located at the vertices of each of the five platonic solids. The eigenvalue k_1 of $\mathcal{G}$ corresponds to the eigenvector $\mathbf{e}$, and $k_{j^\star}$ is the largest eigenvalue of $\mathcal{G}$ in the eigenspace orthogonal to $\mathbf{e}$. This latter eigenvalue sets the competition instability threshold from Corollary 3.1. The last column gives the number M of distinct eigenvalues of $\mathcal{G}$ in the subspace orthogonal to $\mathbf{e}$.

5 The Constant Row Sum Structure of $\mathcal{G}$ and Stability Diagrams for Platonic Solids

Given a collection of N spots centered at $\{x_1, \ldots, x_N\}$, we must determine the source strengths $S_1, \ldots, S_N$ that satisfy

$$\mathbf{S} - \nu(I - \mathcal{E}_0)\mathcal{G}\mathbf{S} + \nu(I - \mathcal{E}_0)\chi = \frac{2\mathrm{E}}{\sqrt{\mathcal{D}}N}\mathbf{e}\,, \qquad \text{where} \quad \mathcal{E}_0 \equiv \frac{1}{N}\mathbf{e}\mathbf{e}^T = \frac{1}{N}\begin{pmatrix} 1 & \cdots & 1 \\ \vdots & & \vdots \\ 1 & \cdots & 1 \end{pmatrix}, \tag{5.1}$$

where $\chi \equiv (\chi(S_1), \ldots, \chi(S_N))^t$ and the Green's matrix $\mathcal{G}$ has entries $\mathcal{G}_{ii} = 0$ and $\mathcal{G}_{ij} = \log|x_i - x_j|$ for $i \neq j$. Since $\mathcal{G}$ is real symmetric, all of its eigenvalues are real.

We would like to classify spot configurations $\{x_1, \ldots, x_N\}$ for which $\mathcal{G}$ has a constant row sum. For such patterns, (5.1) admits a solution for which the spots have a common source strength $S_c = S_1 = \ldots = S_N = 2\mathrm{E}/(\sqrt{\mathcal{D}}N)$. The matrix $\mathcal{G}$ has a constant row sum if and only if the product $\sum_{j\neq i}^{N} |x_i - x_j|$ is independent of each i in $i = 1, \ldots, N$. When this occurs, the eigenvalue k_1 of $\mathcal{G}$ corresponding to the eigenvector $\mathbf{e}$ is

$$k_1 = \log(\mathcal{P})\,, \qquad \text{where} \quad \mathcal{P} \equiv \prod_{\substack{j=1 \\ j\neq i}}^{N} |x_i - x_j|\,. \tag{5.2}$$

When $\mathcal{G}$ has a constant row sum, Corollary 3.1 shows that the competition instability threshold is set by the largest eigenvalue $k_{j^\star} \equiv \max_{2\leq j\leq N} k_j$ in the eigenspace of $\mathcal{G}$ orthogonal to $\mathbf{e}$, i.e. $\mathcal{G}\mathbf{b_j} = k_j\mathbf{b_j}$, with $\mathbf{b_j}^T\mathbf{e} = 0$ for $j = 2, \ldots, N$.

The condition that $\mathbf{e}$ is an eigenvector of $\mathcal{G}$ provides a geometrical restriction on the locations of the spots. The matrix $\mathcal{G}$ has $\mathbf{e}$ as an eigenvector for two-spot patterns with arbitrary spot locations, and for equally-spaced spots along a latitudinal ring. Moreover, for the case of equally-spaced spots along a latitudinal ring the matrix $\mathcal{G}$ is circulant-symmetric, and its spectrum can be obtained analytically as in Appendix D.

Next, consider the five platonic solids whose vertices lie on the unit sphere. It is readily shown that $\mathcal{G}$ has a constant row sum when the spots are located at the vertices of each of these regular polyhedra. In Table 1 we give numerical results for the eigenvalues k_1 and $k_{j^\star}$ of $\mathcal{G}$ corresponding to each of the five platonic solids. Other configurations leading to a constant row sum structure for $\mathcal{G}$ include a rotated cube, where the upper plane is rotated 45° with respect to the bottom plane. For this configuration, we calculate numerically that $k_1 \approx 2.606$ and $k_{j^\star} = 0.2027$. However, it appears to be a rather challenging geometric problem to classify all spot configurations for which $\mathbf{e}$ is an eigenvector of $\mathcal{G}$.

In general, for points that are equi-distributed on the surface of the sphere with respect to some cost function, $\mathbf{e}$ will cease to be an eigenvector of $\mathcal{G}$. One classical way of equi-distributing points on the surface of the sphere is to determine locations x_j for $j = 1, \ldots, N$, with $|x_j| = 1$, that minimize the discrete Coulomb energy $V(x_1, \ldots, x_N) \equiv$

Number of points N	$\|\|\xi - \mathbf{e}\|\|_2$
8	$6.0301e-16$
10	0.0216
20	0.0050
50	0.0029
100	0.0029
120	0.0015
130	0.0027

Table 2. The distance $||\dots||_2$ between the principal eigenvector ξ of $\mathcal{G}$ and $\mathbf{e}$, both normalized, for different elliptic Fekete point configurations. For $N = 8$, for which the elliptic Fekete point set is a rotated cube, the first row in this table shows that, up to machine precision, $\mathbf{e}$ is an eigenvector of $\mathcal{G}$ (as was to be expected). For comparison, a random distribution of 100 points on the sphere has a norm difference of 0.2512.

$-\sum_{i=1}^{N}\sum_{\substack{j=1\\ j\neq i}}^{N}\log|x_i - x_j|$. Such points are known as elliptic Fekete points, with the main interest being to determine precise limiting asymptotics of the minimal energy as $N \to \infty$ (see [**6**], [**32**], [**35**], and the references therein). For small values of N, the locations of elliptic Fekete points points can be found by the detailed geometrical constructions of [**12**] for $N = 4$ and $N = 5$, [**16**] for $N = 6$, and [**2**] for $N = 12$. However, for larger values of N, numerical optimization strategies are required to determine the global minimum. This is a challenging computational problem since V has many local minima with nearly the same energy as at the global minimum point (cf. [**32**], [**35**]).

We remark that the the discrete energy $V(x_1, \dots, x_N)$ corresponds to the sum of all the entries of the matrix $-\mathcal{G}$. In general, the point set $\{x_1, \dots, x_N\}$ that globally minimizes V, does not necessarily lead to a Green's matrix $\mathcal{G}$ having a constant row sum. An example of this is for $N = 5$, where the elliptic Fekete point set consists of points at the two poles of the sphere and three equally spaced points on the equator (cf. [**12**]). For this configuration, $\mathcal{G}$ does not have a constant row sum. Conversely, spot configurations for which $\mathcal{G}$ has a constant row sum are clearly not necessarily elliptic Fekete points. In particular, N equally-spaced points on an equator of the sphere are not Fekete points, but they do correspond to critical points of V. Within the class of platonic solids the vertices of the tetrahedron with $N = 4$ (see Corollary 3 of [**12**]), the octahedron with $N = 6$ (see [**16**]), and the icosahedron with $N = 12$ (see [**2**]), are all both elliptic Fekete point sets and point configurations for which $\mathcal{G}$ has a constant row sum. We remark that the elliptic Fekete points with $N = 8$ do not form a cube structure. In fact, a rotated cube where the upper plane is rotated 45° with respect to the bottom plane gives a smaller value of V.

However, what we have observed is that for an elliptic Fekete point set there is an eigenvector of $\mathcal{G}$ that is in some sense rather close to $\mathbf{e}$. For various elliptic Fekete point set configurations, in Table 2 we give numerical results for the norm of the difference between the eigenvector ξ corresponding to the largest eigenvalue of $\mathcal{G}$ and $\mathbf{e}$. A theoretical explanation for this is, however, lacking.

Next, we compute phase diagrams in parameter space for the stability of quasi-equilibrium patterns when the spots are at the vertices of platonic solids. In the left panel of Fig. 14 we plot competition instability thresholds of $\mathcal{D}/\mathrm{E}^2$ versus f for $\varepsilon = 0.05$ when the spots are located at the vertices of the first four platonic solids of Table 1. The competition instability threshold was computed numerically by determining the root of (3.17) of Corollary 3.1, where $k_{j^\star}$ in (3.17) is given in the fourth column of Table 1. In the right panel of Fig. 14 we plot the corresponding spot self-replication threshold of $\mathcal{D}/\mathrm{E}^2$ versus f for each of these four solids.

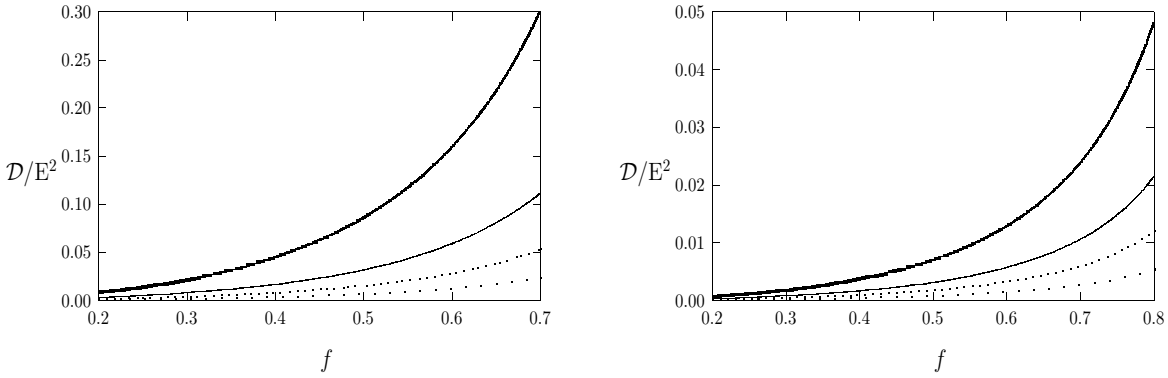

FIGURE 14. Left panel: Competition instability thresholds of $\mathcal{D}/\mathrm{E}^2$ versus f when $\varepsilon = 0.05$ for four spots (heavy solid curves), six spots (solid curves), eight spots (dotted curves), and twelve spots (widely spaced dots), located at the vertices of the corresponding platonic solids. For parameter values above these curves we predict a competition instability. Right panel: Spot self-replication thresholds of $\mathcal{D}/\mathrm{E}^2$ for the platonic solids described in the left panel. For parameter values below these curves we predict a simultaneous spot-splitting event.

6 Comparison of Asymptotic and Numerical Results

In this section we validate our stability results by comparing our theoretical predictions against full numerical results computed from (1.2). The numerical method used to compute RD patterns on surfaces is described in §6.1.

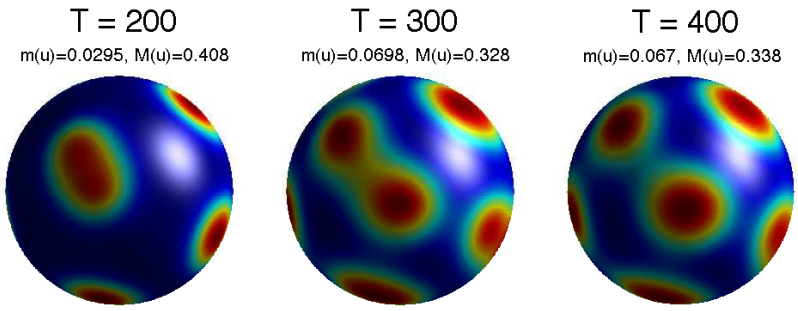

FIGURE 15. **Experiment 1 (Localized Spot Patterns):** Full numerical computations for (1.2) on the unit sphere for $f = 0.8$, $\varepsilon = 0.075$, $\mathcal{D} = 0.2$, $\tau = 1/f^2$, with initial data (6.1). For $t \le 70$ we take $\mathrm{E} = 4$ and obtain the transient dynamics shown in Fig. 2. For $t \ge 70$, we increase E slowly as $\mathrm{E} = \min(4 + 0.05(t - 70), 6)$ and plot the solution at $t = 200, 300, 400$. Spot self-replication events occur over a rather long time-scale. Here $m(u)$ and $M(u)$ are the min and max of u on the sphere.

Experiment 1 (Localized Spot Patterns): We choose $f = 0.8$, $\varepsilon = 0.075$, $\mathcal{D} = 0.2$, $\tau = 1/(0.8)^2$, and $\mathrm{E} = 4.0$. We take the initial data

$$u(x,0) = \frac{\varepsilon^2 \mathrm{E}}{(1-f)}\,(1 + 0.02 \times \mathrm{rand})\,, \qquad v(x,0) = \frac{(1-f)}{(\varepsilon^2 \mathrm{E})}\,(1 + 0.02 \times \mathrm{rand})\,, \tag{6.1}$$

representing a 2% random perturbation of the spatially homogeneous state, Here rand is uniformly distributed in $[0,1]$.

The numerical results in Fig. 2 show the formation of an eight-spot localized pattern from initial data. Since the spots at $t = 70.3$ in Fig. 2 are (roughly) equidistributed, their approximate common source strength is $S_c = 2\mathrm{E}/(\sqrt{\mathcal{D}}N) = 2.23$. The spot self-replication threshold from the right panel of Fig. 4 is $\Sigma_2(0.8) = 2.28 > S_c$, so that the eight-spot pattern is initially stable to spot self-replication. Now for $t \ge 70$, we increase E slowly in time as

$\mathrm{E} = \min(4 + 0.05(t - 70), 6)$, which yields $S_c = 3.35 > \Sigma_2(0.8)$ when $\mathrm{E} = 6$. When $t = 110$, corresponding to $\mathrm{E} = 6$ and $S = 3.35 > \Sigma_2$, we compute from the numerical method described in §3.1 that the peanut splitting mode has a rather small growth rate of $\lambda \approx 0.144$. The theoretical results are consistent with the full numerical results displayed in Fig. 15 showing that spot self-replication occurs, but over a rather long time-scale.

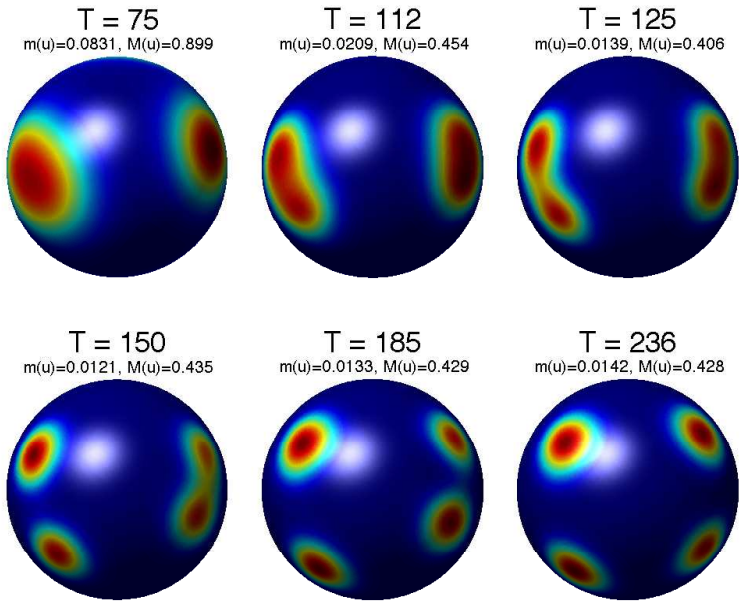

FIGURE 16. **Experiment 2 (A Slowly Growing Sphere):** Full numerical computations for (1.2) on the unit sphere for $f = 0.8$, $\varepsilon = 0.12$, $\mathcal{D} = 1.0$, $\tau = 1/f^2$, and $\mathrm{E} = 4$, with initial data (6.1). The transient dynamics (not shown) leads to a pattern of four equally-spaced spots at $t = 75$. For $t \geq 75$ we effectively increase the radius of the sphere by decreasing ε and $\mathcal{D}$ as $\varepsilon = 0.12/L$ and $\mathcal{D} = 1/L^2$, where we take $L = \min(1.0 + 0.02(t - 75), 2.0)$ for $t \geq 75$. We observe that the four spots undergo (roughly) simultaneous spot self-replication events.

Experiment 2 (A Slowly Growing Sphere): We choose $f = 0.8$, $\varepsilon = 0.12$, $\mathcal{D} = 1.0$, $\tau = 1/(0.8)^2$, and $\mathrm{E} = 4.0$, and take the initial data (6.1). The full numerical results displayed in Fig. 16 show that the transient dynamics leads to a pattern of four equally-spaced spots at $t = 75$. For $t \geq 75$ we then slowly decrease ε and $\mathcal{D}$ as

$$\varepsilon = 0.12/L\,, \qquad \mathcal{D} = 1/L^2\,; \qquad L = \min(1.0 + 0.02(t - 75), 2.0) \quad \text{for} \quad t \geq 75\,.$$

This is adiabatically equivalent to fixing $\varepsilon = 0.12$ and $\mathcal{D} = 1.0$ and slowly doubling the radius $L(t)$ of the sphere from $L = 1$ at $t = 75$ to $L = 2$ at $t = 125$.

For these parameter values, and when $L = 1$, we calculate $S = 2$ for four equally-spaced spots. Since the spot self-replication threshold is $\Sigma_2(0.8) = 2.28 > S$ when $f = 0.8$ (see Fig. 4), the four-spot pattern is initially stable to self-replication. For $N = 4$, the competition instability threshold from (3.17) of Corollary 3.1 is calculated as $\mathcal{D}_c^\star \approx 5.5 > \mathcal{D}$. As the effective sphere radius L grows, S increases at a rate proportional to L, while $\mathcal{D}$ decreases at a rate proportional to L^2. Therefore, we predict that self-replication events will occur, but that competition instabilities are absent. When $t = 100$, corresponding to $L = 1.5$ and $S = 3 > \Sigma_2$, we compute from the numerical method described in §3.1 that the growth rate for the peanut-splitting mode is $\lambda \approx 0.10$. In the numerical results shown in Fig. 16, we observe that (roughly) simultaneous spot self-replication events are initiated at $t = 112$, which is

consistent with the theoretical prediction. For $N = 8$ equally spaced spots on the sphere, and with $L = 2$, we calculate $S = 2\mathrm{E}/(8\sqrt{\mathcal{D}}) = 2 < \Sigma_2$ and so no further spot-splitting events are predicted. This is consistent with the stabilization of the pattern at large times shown in Fig. 16.

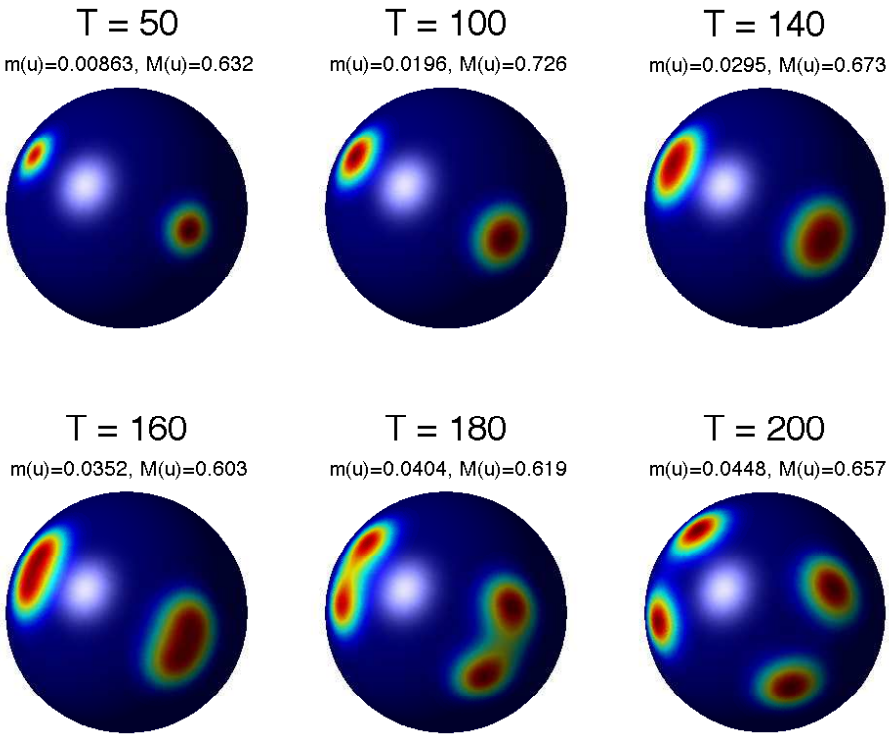

FIGURE 17. **Experiment 3 (Increasing the Fuel E):** Full numerical computations for (1.2) on the unit sphere for $f = 0.7$, $\varepsilon = 0.06$, $\mathcal{D} = 0.7$, $\tau = 1/f^2$, and $\mathrm{E} = 2.5$, with initial data (6.1). At the end of the transient dynamics when $t \approx 50$, we observe a four-spot pattern. For $t \geq 50$, we then slowly increase E as $\mathrm{E} = 2.5 + \sigma(t - 50)$ with $\sigma = 0.05$ for $t \geq 50$. A roughly simultaneous spot self-replication event is initiated when $t \approx 140$, and we obtain a distinct eight-spot pattern at $t \approx 200$. Here $m(u)$ and $M(u)$ are the min and max of u on the sphere.

Experiment 3 (Increasing the Fuel E): We choose $f = 0.7$, $\mathrm{E} = 2.5$, $\tau = 1/(0.7)^2$, $\varepsilon = 0.06$, and $\mathcal{D} = 0.7$, and with initial data (6.1). We choose $\mathrm{E} = 2.5$ for $0 \leq t \leq 50$, and thereafter increase the fuel E slowly as $\mathrm{E} = 2.5 + \sigma(t - 50)$ with $\sigma = 0.05$ for $t \geq 50$.

Our numerical results displayed in Fig. 17 at different times show that a four-spot pattern is formed after the initial transient, with spots aligned (roughly) along an equator. A slightly elongated spot is seen at $t = 140$, with a distinct simultaneous spot self-replication event clearly in progress at $t = 160$. The pattern at $t = 200$ has eight spots.

Assuming that the spots are indeed equally-spaced on an equator, the competition instability threshold for this pattern is calculated from the root of (3.17) of Corollary 3.1. We obtain $k_{j^\star} = 0$ from the circulant Green's matrix $\mathcal{G}$, and from the root of (3.17) with $\mathrm{E} = 2.5$ and $N = 4$, we predict that there is a competition instability when $\mathcal{D} > \mathcal{D}_c^\star \approx 1.45$. Our value of $\mathcal{D} = 0.7$ is well-below this threshold.

Again assuming that the spots are equally-spaced on an equator, the common source strength S_c for this pattern when $\mathrm{E} = 2.5$ and $\mathcal{D} = 0.7$ is $S_c = 2\mathrm{E}/\sqrt{\mathcal{D}}N \approx 1.494$. The self-replication threshold from the left panel of Fig. 4 is

$\Sigma_2(0.7) = 3.235$. As E increases slowly for $t \geq 50$, eventually the common source strength exceeds Σ_2. For $t \approx 108$, where $\mathrm{E} \approx 5.4$, we have $S_c \approx 3.235$, which is the (static) self-replication threshold of four spots on an equator. For $t = 140$, where $\mathrm{E} = 7$, we get $S_c \approx 4.18$. From the left panel of Fig. 4 this corresponds to a relatively slow growth rate of $\lambda \approx 0.13$ for a peanut-splitting instability. This suggests that, even in the absence of delayed bifurcation effects due to the slowly varying control parameter E, there is a relatively slow initiation of a spot self-replication event. This is consistent with what is observed in Fig. 17. From Fig. 17, the spots are beginning to split at $t = 140$, and a distinct 8 spot pattern has emerged by $t = 200$.

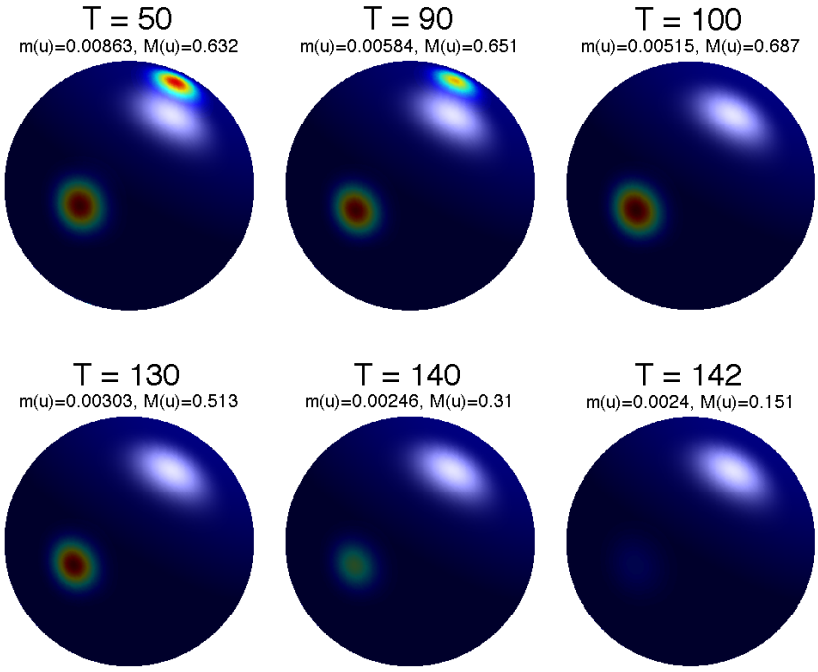

FIGURE 18. **Experiment 4 (Decreasing the Fuel E):** Full numerical computations for (1.2) on the unit sphere for $f = 0.7$, $\varepsilon = 0.06$, $\mathcal{D} = 0.7$, $\tau = 1/f^2$, and $\mathrm{E} = 2.5$, with initial data (6.1). We take $\mathrm{E} = 2.5$ for $0 \leq t \leq 50$, and then slowly decrease E as $\mathrm{E} = 2.5 - \sigma(t - 50)$ with $\sigma = 0.02$ for $t \geq 50$. The four-spot pattern that exists at the end of the transient dynamics undergoes a competition instability in the interval $90 < t < 100$ in which two spots are annihilated. An additional spot is annihilated when $t \approx 140$, leaving one remaining (weak) spot. Here $m(u)$ and $M(u)$ are the min and max of u on the sphere.

Experiment 4 (Decreasing the Fuel E): In Experiment 4 we keep the same parameter values as in Experiment 3, but instead we decrease the fuel E slowly in time with $\mathrm{E} = 2.5 - \sigma(t - 50)$ for $t \geq 50$ with $\sigma = 0.02$. The numerical results displayed in Fig. 18 show that a competition instability occurs in the interval $90 < t < 100$ leading to a two-spot pattern with spots at the two poles of the sphere. As E is decreased further, a second annihilation event is triggered around $t \approx 140$, leaving only one remaining (weak) spot.

As E decreases, we are increasingly below the self-replication threshold as t increases. From a numerical computation of the root of (3.17) of Corollary 3.1, the competition instability thresholds $\mathcal{D}_c^\star$ for a four-spot pattern at different values of E are as follows: $\mathcal{D}_c^\star \approx 0.919$ at $\mathrm{E} = 2.0$ when $t = 75$, $\mathcal{D}_c^\star \approx 0.704$ at $\mathrm{E} = 1.75$ when $t = 87.5$, and $\mathcal{D}_c^\star \approx 0.517$ at $\mathrm{E} = 1.5$ when $t = 100$. Since $\mathcal{D} = 0.7$, we predict (assuming negligible delayed bifurcation effects), that a competition instability for the four-spot pattern will occur in the interval $87.5 < t < 100$. In addition, since the most unstable

eigenvector of the Green's matrix corresponding to $k_{j^\star} = 0$ is the sign fluctuating perturbation $(-1, 1, -1, 1)$ of the spot amplitudes, we predict that the competition instability will lead to the annihilation of two of the spots. This is precisely what is observed in Fig. 18.

Then, for a two-spot equally spaced pattern, we calculate from (3.17) of Corollary 3.1, competition instability thresholds of $\mathcal{D}_c^\star \approx 1.886$ at $\mathrm{E} = 1.25$ when $t = 117.5$, $\mathcal{D}_c^\star \approx 1.207$ at $\mathrm{E} = 1.0$ when $t = 125$, $\mathcal{D}_c^\star \approx 0.6789$ at $\mathrm{E} = 0.75$ when $t = 137.5$, and $\mathcal{D}_c^\star \approx 0.4665$ at $\mathrm{E} = 0.62$ when $t = 144$. Since $\mathcal{D} = 0.7$, we predict that a further competition instability leading to the destruction of one of the two remaining spots will be triggered for t slightly below $t = 140$. This is precisely what is observed in Fig. 18.

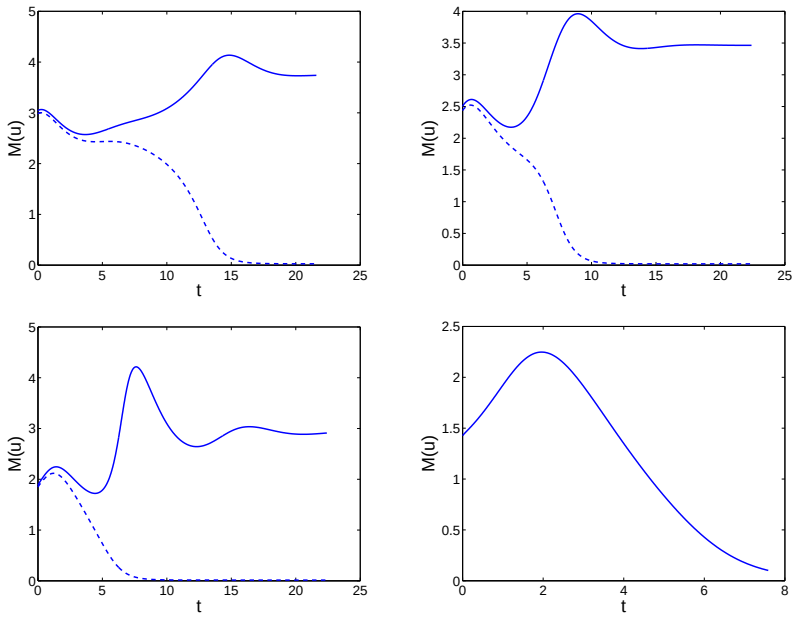

FIGURE 19. **Experiment 5 (The NLEP Regime: Two Spots):** Plot of the two numerically computed spot amplitudes $M(u)$ versus t for a two-spot pattern on the unit sphere with spots at $(1, 0, 0)$ and $(0, 1, 0)$ for the parameter values $f = 0.5$, $\varepsilon = 0.06$, $\mathcal{D} = 28.1$, and $\tau = 1/f^2$, when $\mathrm{E} = 7.0$ (top left), $\mathrm{E} = 5.5$ (top right), $\mathrm{E} = 4.0$ (bottom left), and $\mathrm{E} = 3.0$ (bottom right). The prepared initial condition for (1.2) is given in (6.2). For the three larger values of E, where the initial spot amplitudes are perturbed by $\pm 1\%$, a competition instability leads to the annihilation of one of the spots. For $\mathrm{E} = 3$, where no initial perturbation of the spot amplitudes is imposed, a synchronous instability is seen to lead to simultaneous spot annihilation.

Experiment 5 (The NLEP Regime: Two Spots): For a two-spot pattern with spots at $x_1 = (1, 0, 0)$ and $x_2 = (0, 1, 0)$, we compare our NLEP stability results of §4.4 with full numerical results computed from (1.2) for the parameter values $f = 0.5$, $\varepsilon = 0.06$, $\mathcal{D} = 28.1$, and $\tau = 1/f^2$, and with four different choices of E. The prepared initial condition for the numerical solution of (1.2), given for $N = 2$ by

$$u(x,0) = \varepsilon^2 \mathrm{E} + u_m \sqrt{\mathcal{D}} \sum_{j=1}^{N} \delta_j \operatorname{sech}^2\left(\frac{|x - x_j|}{2\varepsilon}\right), \qquad v(x,0) = \begin{cases} \frac{1}{\sqrt{\mathcal{D}}} v_m & \text{for } |x - x_j| \le 2\varepsilon \\ -\frac{2\pi S}{\sqrt{\mathcal{D}}} \sum_{i=1}^{N} G(x; x_i) + \frac{\bar{v}}{\sqrt{\mathcal{D}}} & \text{for } |x - x_j| \gg 2\varepsilon \end{cases}, \tag{6.2}$$

has a form very similar to that of the quasi-equilibrium solution in (2.15) of Principal Result 2.1. In (6.2), $S = 2\mathrm{E}/\sqrt{\mathcal{D}}N$ with $N = 2$, while u_m and v_m denote the solution to the core problem (2.3) at $\rho = 0$.

For each of $\mathrm{E} = 7.0$, $\mathrm{E} = 5.5$, and $\mathrm{E} = 4.0$, we let $\delta_1 = 1.01$ and $\delta_2 = 0.99$ in (6.2), which corresponds to a $\pm 1\%$ initial perturbation of the spot amplitudes. For $\mathrm{E} = 3.0$ we take $\delta_j = 1$ for $j = 1, 2$, so that no initial spot amplitude

perturbation is imposed. A plot of the two numerically computed maximum spot amplitudes $M(u)$ versus time for each of the four choices of E is shown in Fig. 19.

For each of these four values of E, our choice $\mathcal{D} = 28.1$ exceeds the competition instability threshold $\mathcal{D}_c^*$ of (4.25). Thus, the competition instability mode is always unstable. To determine the Hopf bifurcation threshold we first calculate that $\mathcal{D}_0 = \mathcal{D}\nu \approx 10.07$ when $\nu = -1/\log\varepsilon \approx 0.3554$. Then, from the right panel of Fig. 12 we conclude that there is a synchronous Hopf bifurcation when E = 4.85, with the synchronous mode being unstable when E < 4.85 and stable when E > 4.85. For the two larger values of E, where E > 4.85, Fig. 19 shows a competition instability. For E = 5.5, which is only marginally above the Hopf bifurcation threshold, in Fig. 19 we observe a damped temporal oscillation of one of the spot amplitudes. For E = 4.0, which is below the Hopf threshold, both the synchronous and competition instability modes are present. With the perturbed initial data, which biases the competition mode, we observe a rather large overshoot in one of the spot amplitudes before only one of the two spots is annihilated. Finally, if we take E = 3.0 and impose no perturbation of the spot amplitudes, we observe a synchronous annihilation of the two spot amplitudes. For this value of E, the NLEP of Principal Result 4.3 for the synchronous mode has a complex conjugate pair of eigenvalues that is close to the positive real axis in the λ-plane.

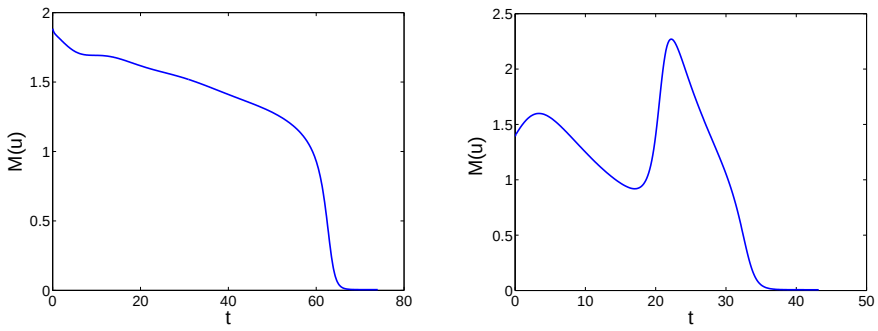

FIGURE 20. **Experiment 6 (The NLEP Regime: One Spot):** Plot of the numerically computed spot amplitude $M(u)$ versus t for a one-spot pattern on the unit sphere when $f = 0.5$, $\varepsilon = 0.06$, $\mathcal{D} = 6.25$, and $\tau = 1/f^2$. The Hopf bifurcation threshold from the left panel of Fig. 12 is E ≈ 1.97 with corresponding eigenvalue $\lambda \approx \pm 0.57\,i$. Left panel: We take E = 2.5 for $0 \le t \le 5$ and E $= 2.5 - 0.02(t-5)$ for $t \ge 5$. The spot is annihilated quickly in time when E dips below the threshold. Right panel: E = 1.8 for $t \ge 0$. There is an overshoot of the spot amplitude before an oscillatory collapse.

Experiment 6 (The NLEP Regime: One Spot): For a one-spot pattern, we compare our NLEP stability results of §4.4 with full numerical results computed from (1.2) when $f = 0.5$, $\varepsilon = 0.06$, $\mathcal{D} = 6.25$, and $\tau = 1/f^2$. We take E = 2.5 for $0 \le t \le 5$ and then slowly decrease E as E $= 2.5 - 0.02(t-5)$ for $t \ge 5$. The one-spot initial condition for (1.2) was taken to be (6.2) with $N = 1$.

From the NLEP stability results of §4.4 shown in the left panel of Fig. 12, we predict a Hopf bifurcation when E ≈ 1.97, with the spot being unstable if E < 1.97. The NLEP computations also yields the corresponding imaginary eigenvalues $\lambda \approx \pm 0.57i$ when E ≈ 1.97. Our full numerical computations of (1.2) show the sudden annihilation of the spot once E is near E ≈ 1.6, which is somewhat below the predicted threshold. The slight discrepancy is probably attributable to a delayed bifurcation effect. To support this claim, in the right panel of Fig. 20 we show full numerical results for the spot amplitude for the same parameter set but with E fixed at E = 1.8, which is only slightly below the Hopf threshold of E ≈ 1.97. The spot amplitude is found to oscillate, and then collapse.

Experiment 7 (Spots on a Manifold): For our final example, we compute Brusselator spot patterns on the manifold

obtained by revolving the curve $y = b + 2(1 - x^2)$ with $b = 0.635$ about the x-axis on $|x| \le 1$. This gives the surface

$$\Omega = \{(x, y, z) \,|\, y^2 + z^2 = \left[b + 2(1 - x^2)^2\right]^2 \,,\ |x| \le 1\}\,, \tag{6.3}$$

which has a surface area $|\Omega| = 2\pi \int_{-1}^{1} \left(b + 2(1 - x^2)\right) \sqrt{1 + 16x^2}\, dx \approx 16\pi$, that is four times larger than that of the unit sphere. In the full numerical computations of (1.2) on Ω we imposed Neumann boundary conditions on the rim of the two sides at $x = \pm 1$. The parameter values are $f = 0.8$, $\mathrm{E} = 1.75$, $\tau = 1/(0.8)^2$, $\varepsilon = 0.18$, and $\mathcal{D} = 2.5$, and we take the initial data (6.1). We choose $\mathrm{E} = 1.75$ for $0 \le t \le 50$, and thereafter increase E slowly as $\mathrm{E} = \min(1.75 + 0.05(t - 50), 4)$ for $t \ge 50$, so that the ramp in E is turned off for $t \ge 95$.

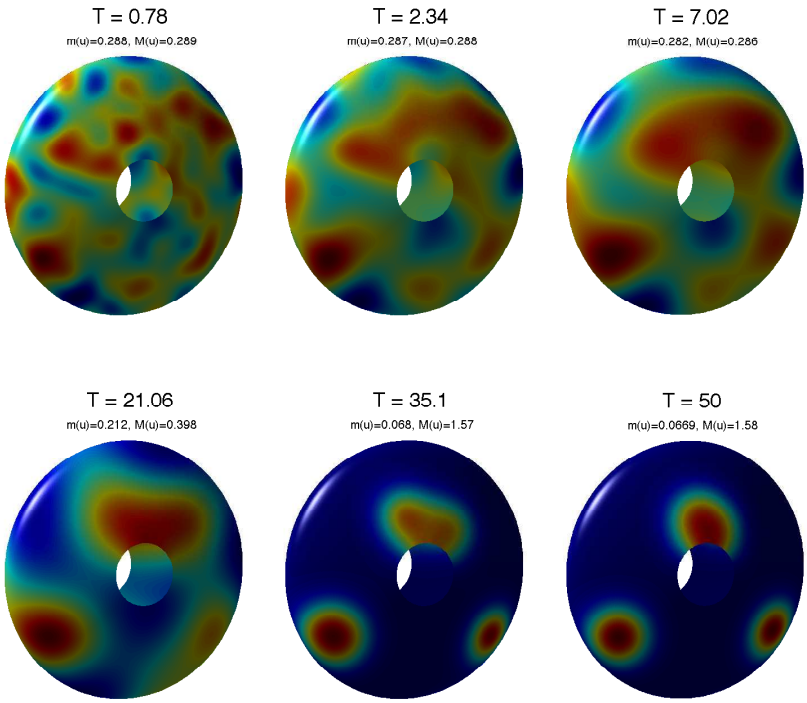

FIGURE 21. **Experiment 7 (Spots on a Manifold: Transient Phase):** Full numerical computations on $0 < t < 50$ for (1.2) on the surface (6.3) with $b = 0.635$ for $f = 0.8$, $\varepsilon = 0.18$, $\mathcal{D} = 2.5$, $\tau = 1/f^2$, and $\mathrm{E} = 1.75$. The initial data is (6.1). There are six localized spots at the end of the transient dynamics. Here $m(u)$ and $M(u)$ are the min and max of u on the surface.

To extend our theoretical stability analysis for spot patterns on a sphere to patterns on this smooth manifold, we would need to determine the source-neutral and reduced-wave Green's function for the manifold, which is not feasible analytically. However, for an N-spot pattern for which the Green's matrix has a constant row sum, we can still predict that a spot self-replication event occurs when the common source-strength S_c satisfies

$$S_c \equiv \frac{|\Omega|\mathrm{E}}{2\pi\sqrt{\mathcal{D}}N} \approx \frac{8\mathrm{E}}{\sqrt{\mathcal{D}}N} > \Sigma_2(0.8) \approx 2.28\,. \tag{6.4}$$

This result for S_c is readily obtained by integrating (2.7) over Ω and then using $|\Omega| \approx 16\pi$.

In the full numerical results shown in Fig. 21 we observe that the transient dynamics has lead to a pattern of $N = 6$ (roughly) equally-spaced spots at $t = 50$. If we use our common S criterion of (6.4) as a guide to predicting spot self-replication, we obtain from (6.4) that $S_c \approx 1.48 < \Sigma_2(0.8) \approx 2.28$ when $\mathrm{E} = 1.75$, $\mathcal{D} = 2.5$, and $N = 6$. As E

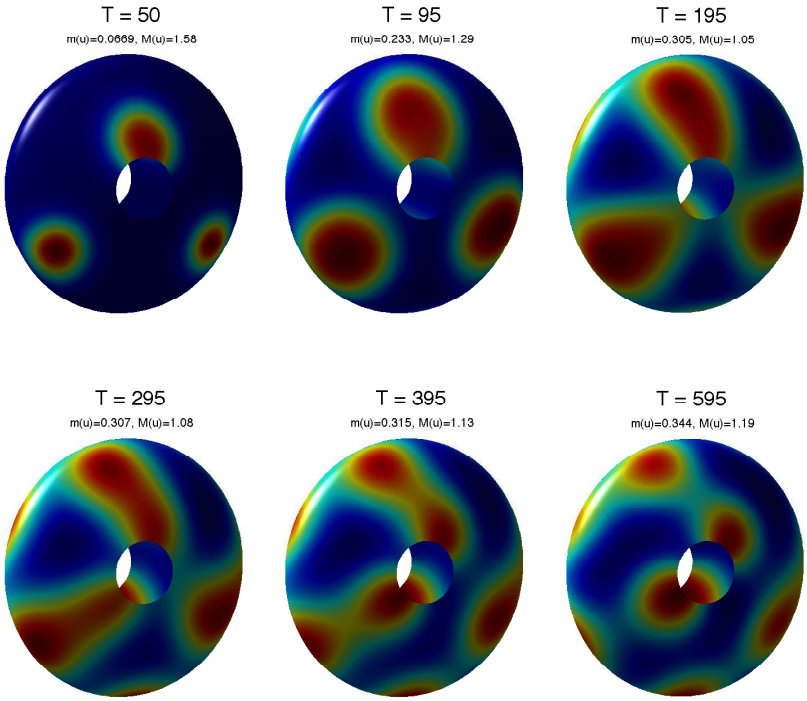

FIGURE 22. **Experiment 7 (Spots on a Manifold: Final Phase):** Full numerical computations on $50 < t < 595$ for (1.2) on the surface (6.3) with $b = 0.635$ for $f = 0.8$, $\varepsilon = 0.18$, $\mathcal{D} = 2.5$, and $\tau = 1/f^2$. For $t \geq 50$, E is slowly increased as $\mathrm{E} = \min(1.75+0.05(t-50), 4)$. Four of the six spots at the end of the transient dynamics at $t = 50$ have undergone self-replication by $t = 595$, leading to a pattern of ten spots. Here $m(u)$ and $M(u)$ are the min and max of u on the surface.

slowly increases, eventually $S_c > \Sigma_2(0.8)$, and so we predict that spot self-replication should occur. In particular, upon setting $\mathrm{E} = 4$, which holds for $t \geq 95$, we get $S_c \approx 3.37 > \Sigma_2(0.8)$ for $N = 6$ spots. When $S_c = 3.37$, the numerical method used in §3.1 predicts a rather slow growth rate of $\lambda \approx 0.147$ for a peanut-splitting instability. The full numerical results in Fig. 22 for $t \geq 50$ showing (roughly) simultaneous spot-splitting is consistent with the theoretical prediction of self-replication. In the last frame in Fig. 22 when $t = 595$, there are 10 spots. Assuming an identical source strength for this pattern, we get $S_c = 8(4)/\left[10\sqrt{2.5}\right] \approx 2.02$, which is now below the spot-splitting threshold.

Although it is unclear whether the pattern at $t = 50$ is such that the source strengths are identical, the simple criterion (6.4), which does not require any knowledge of the Green's functions for the manifold, is still rather effective as a guide to predicting spot self-replication behavior.

6.1 Numerical Method for RD Patterns on the Sphere

Previous numerical work for RD systems on surfaces include [**41**], [**8**], [**17**], [**13**], and [**3**]. For the sphere, in [**41**] a discretization of the Laplacian in spherical coordinates (θ, ϕ) was used together with an explicit Euler integration in time. A related approach, but with an implicit-explicit method, was used in [**13**] for computing RD patterns on a growing sphere. The disadvantage of such methods is that the finite difference method subdivides the (θ, ϕ) domain into equal subsections, and on the full sphere this leads to the majority of the grid points being close to the poles. Since the maximum time step in two dimensions for an explicit time integration scales as $(\Delta x)^2$, with Δx being the

smallest distance between points, the integration time will reflect the scale at the poles, making it very numerically intensive to resolve events that occur elsewhere, such as in the vicinity of localized spots. The work of [**8**] involved simulating a general RD system modelling tumour growth. A method of lines approach with spherical harmonics was used together with fast Fourier transform techniques to calculate the nonlinear reaction kinetics. Although this method has a high degree of accuracy and very fast convergence rates, it requires a large number of modes to resolve any localized structures, and the method is not readily extended to computing RD patterns on arbitrary smooth manifolds. More robust numerical approaches based on finite element methodolgies for calculating RD patterns on evolving surfaces are described recently in [**17**] and [**3**].

For the problem of simulating spot dynamics for the Brusselator on the surface of the sphere, we need to perform very long-time integrations since the time-scale for the motion of the spots is $\mathcal{O}(\varepsilon^{-2})$. Compounding this issue, we also need a fine spatial gridding to resolve the $\mathcal{O}(\varepsilon)$ wide transition layers that define the spatial extent of a localized spot. A von Neumann analysis applied to (1.2) leads to the well-known stability time stepping restriction of $\Delta t = \mathcal{O}(\Delta x^2)$ due to the stiff diffusion terms. To relax this restriction, especially for large $\mathcal{D}$-values, implicit-explicit schemes may be considered [**33**]. While the use of implicit-explicit schemes often enables the use of larger stable step-sizes, they still lead to a restriction of the same asymptotic form due to the $\mathcal{O}(\varepsilon^{-2})$ reaction term for v. Surprisingly little benefit is obtained from a fully implicit treatment of the RD system for pattern formation. In particular, in [**33**] it is shown that qualitatively incorrect results are obtained when time steps larger than those for implicit-explicit methods are taken. In view of these trade-offs, we considered ε in the range of 0.06 to 0.15 and performed our time-stepping with explicit time-stepping schemes. As a consequence of our choice of ε, we were not able to validate any results for the dynamics of spots that occur on an $\mathcal{O}(\varepsilon^{-2})$ time-scale.

Closest Point Method. The approach that we chose to implement is the recently-developed Closest Point Method [**34**]. The method alternates two steps. In the first step of this method, the solution on the surface is extended into the surrounding 3-D space in the normal direction. The second step evolves the system by advancing the corresponding 3-D PDE for one time step. When applied to an RD system, the justification for the method is particularly intuitive: The 3-D Laplacian normal to the surface is zero when applied to the extended function. Thus, the only contribution arising from evaluating the 3-D Laplacian is the Laplacian intrinsic to the surface. For our problem of reaction-diffusion intrinsic to a smooth surface, this is all that is needed to guarantee that the desired surface flow is obtained for any given step. Notice that this approach has the advantage that the problem is solved on the grid using the standard 7-point Laplacian operator in 3-D, and the geometry of the system is introduced using the closest point extension step (a step which is carried out using interpolation). Thus, the approach is implemented via a closest point representation of the surface, entirely standard explicit or implicit 3-D solvers, and an interpolation algorithm in 3-D. See [**20**] for a simple MATLAB implementation of the method for RD systems.

We now give further details related to the algorithms used in this paper. First, observe that our principal shape, the unit sphere, has a particularly simple closest point representation when centered at the origin: $\mathrm{cp}(\mathbf{x}) = \mathbf{x}/||\mathbf{x}||$. An algorithm for determining the closest point function for general triangulated shapes is described in [**21**]. Second, computations were localized by solving the 3-D PDE in a narrow band around the embedded surface. The band must be chosen to be wide enough to accommodate the differencing and interpolation stencils; see [**34**] for details. Finally we note that explicit Euler time-stepping was used under the usual stability time-stepping restriction of $\Delta t \leq \frac{1}{8\tau\mathcal{D}}\Delta x^2$. This choice is simple and adequate for our purposes, although faster results may be possible using implicit-explicit time-stepping and the implicit Closest Point Method described in [**19**].

The discretization step-size Δx was taken to be 1/50 for our NLEP calculations, 1/20 for the solid of revolution (experiment 7) and 1/40 for all other computations. To carry out the closest point extension step, tri-cubic interpolation was implemented via barycentric Lagrange interpolation. In our NLEP simulations the ratio of the diffusion coefficients was particularly large. To account for the widely varying scales and give improved efficiency, several (typically 10) time steps of the v-equation were taken for each of the u-equation. Because each extension step of the Closest Point Method introduces an interpolation error, balancing the computational effort in this way gave the additional benefit of improving the accuracy and stability of our NLEP simulations.

We remark that the Closest Point Method may be applied to rather general PDEs, including those with gradient, divergence and biharmonic operators. See [**34**, **19**] for further details.

7 Discussion

In this concluding section we outline a few directions that warrant further investigation.

One key open problem is to study the dynamics of localized spot patterns for the Brusselator on the sphere. As for the GS model in a planar domain (cf. [**10**]), it should be possible to derive an ODE-DAE system for the slow evolution of the spot locations and their associated source strengths on an anticipated time-scale of $t = \mathcal{O}(\varepsilon^{-2})$. This system characterizes the slow motion of spots on the sphere in the absence of any $\mathcal{O}(1)$ time-scale instabilities. However, depending on the parameter values, such instabilities can be triggered due to dynamic bifurcation events that occur when instability thresholds are exceeded. In particular, our theory would predict that spot self-replication should occur whenever an individual spot source exceeds the peanut-splitting threshold $\Sigma_2(f)$. It is an open problem to provide a quantitative description of the slow spot dynamics punctuated by either spot-annihilation (due to oscillatory collapse or competition) or spot self-replication.

In another direction, the ODE-DAE system for slow spot evolution is likely to share some similarities with the ODE system governing the motion of Eulerian point vortices on the surface of the sphere (cf. [**26**] and the references therein). More recently, [**25**] studied the relationship between circle packing and equilibrium configurations of point vortices on the sphere. In this broader context, it would be interesting to study the existence and stability of fixed points of the ODE-DAE system for spot evolution for the Brusselator. Such fixed points correspond to true equilibrium spot configurations on the sphere. By studying the matrix spectrum resulting from a linearization around the fixed points of the ODE-DAE system, it should be possible to characterize any weak translation instabilities of multi-spot patterns. In particular, for the Brusselator we expect that there should be a result similar to that for Eulerian point vortices (cf. [**4**], [**5**]) characterizing the maximum number of "stable" spots that can be placed on a ring of constant latitude on the sphere. In fact, for the case of a planar unit disk containing a ring of concentric equally-spaced spots, it was observed numerically for the related Schnakenburg RD system in [**14**] that a small eigenvalue instability is triggered when too many spots are located on a ring.

Another open problem, but with a numerical focus, is to quantify the bifurcation structure that links the weakly nonlinear regime associated with perturbations of the spatially uniform equilibrium state (as studied in [**7**], [**9**], [**22**], [**29**], [**41**] and the references therein) to the regime, studied in this paper, of localized spot patterns. In particular, do localized spot patterns arise from subcritical bifurcations of the weakly nonlinear amplitude equations?

Finally, we remark that our theoretical framework is readily extended to the study of the existence and stability of quasi-equilibrium spot patterns on arbitrary compact 2-D smooth surfaces, provided that one can determine the source-neutral and reduced-wave Green's functions, and their associated regular parts, on the given surface. This

remark follows from the observation that, since the spots are localized, the core problem for a localized spot together with the linearized eigenvalue problem for self-replication instabilities are defined on the tangent-plane to the surface at the spot location. The competition and oscillatory instability threshold are determined from a globally coupled eigenvalue problem defined in terms of the reduced-wave Green's function. In order to implement the theory for spot patterns on arbitrary surfaces, efficient numerical methods to compute the required Green's functions are needed.

Acknowledgements

S. R. and M. J. W. are both grateful for the grant support of NSERC.

Appendix A Scaling of the Brusselator

We first give a formal scaling argument to determine the range of parameters in (1.1) with respect to ε_0 for which localized spot patterns exist. We begin by letting $V = \mathcal{O}(V_{\rm g})$ globally. For U we have different scalings near and away from spots; $U = \mathcal{O}(U_{\rm inn})$ near a spot, and $U = \mathcal{O}(U_{\rm out})$ away from the spots.

In the inner region near a spot at x_0, where $y = \varepsilon_0^{-1}(x - x_0)$, we need $\mathcal{O}(U^2V) = \mathcal{O}(U)$ in order to construct a spot profile. Hence $U_{\rm inn}V_{\rm g} = \mathcal{O}(1)$, so that $U_{\rm inn} = \mathcal{O}\left(1/V_{\rm g}\right)$ in the inner region.

In the outer region, from the V equation in (1.1) we need that the nonlinear term, which is localized near the spots, be approximated by a Delta function with the correct strength, which then balances the diffusion term $D\Delta V$. As such, we have $\int_\Omega U^2V\,dx = \mathcal{O}(\varepsilon_0^2 V_{\rm g}U_{\rm inn}^2) = \mathcal{O}(DV_{\rm g})$. This yields, $U_{\rm inn} = \mathcal{O}(\varepsilon_0^{-1})$ and consequently $V_{\rm g} = \mathcal{O}(\varepsilon_0)$. Next, from the balance in the outer region that $D\Delta V = \mathcal{O}(BU)$, we get that $V_{\rm g} = \mathcal{O}(U_{\rm out})$, which yields $U_{\rm out} = \mathcal{O}(\varepsilon_0)$. Finally, in the outer region we obtain from the U equation in (1.1) that E must balance $(B+1)U$, so that $E = \mathcal{O}(U_{\rm out}) = \mathcal{O}(\varepsilon_0)$.

This very rough scaling analysis suggests that $U_{\rm inn} = \mathcal{O}(\varepsilon_0^{-1})$, $U_{\rm out} = \mathcal{O}(\varepsilon_0)$, $V_{\rm g} = \mathcal{O}(\varepsilon_0)$, when $E = \mathcal{O}(\varepsilon_0)$. Next, we use a non-dimensionalization based on these scalings in order to reduce the number of parameters in (1.1) and isolate our key bifurcation parameters. This motivates the introduction of the new variables u, v, and σ, defined by

$$T = \sigma t\,, \qquad U = \frac{\mu}{\varepsilon_0}u\,, \qquad V = \varepsilon_0 v\,, \qquad E = \varepsilon_0 \mathrm{E}_0\,.$$

With this scaling, the amplitude of a spot in the u-variable is $\mathcal{O}(1)$ as $\varepsilon_0 \to 0$ rather than the $\mathcal{O}(\varepsilon_0^{-1})$ scaling in the U-variable. In terms of these new variables, (1.1) becomes

$$\frac{1}{\sigma(B+1)}u_t = \frac{\varepsilon_0^2}{B+1}\Delta u + \frac{\varepsilon_0^2}{B+1}\frac{\mathrm{E}_0}{\mu} - u + \frac{\mu}{B+1}u^2v\,, \qquad \frac{(B+1)}{\mu^2\sigma}v_t = \frac{D(B+1)}{\mu^2}\Delta v + \frac{(B+1)}{\varepsilon_0^2}\left(\frac{B}{\mu}u - u^2v\right)\,. \tag{A.1}$$

Next, we define ε, T, and μ by $\varepsilon \equiv \varepsilon_0/\sqrt{B+1}$, $\sigma \equiv 1/(B+1)$, and $\mu \equiv B$, so that (A.1) transforms to

$$u_t = \varepsilon^2\Delta u + \frac{\mathrm{E}_0\varepsilon^2}{B} - u + \frac{B}{B+1}u^2v\,, \qquad \frac{(B+1)^2}{B^2}v_t = \frac{D(B+1)}{B^2}\Delta v + \frac{1}{\varepsilon^2}\left(u - u^2v\right)\,. \tag{A.2}$$

This is equivalent to (1.2) of §1.

Appendix B A Spherical Coordinate Transformation

Lemma B.1 *In terms of spherical coordinates, consider a point on the unit sphere given by*

$$x_j = (\cos\phi_j \sin\theta_j, \sin\phi_j \sin\theta_j, \cos\theta_j)^T\,,$$

with $0 < \phi_j < 2\pi,\ 0 < \theta_j < \pi$. *Then, as* $x \to x_j$, *we have* $|x - x_j| = |y|(1 + o(1))$ *where* $y = (y_1, y_2)^T = (\hat{\phi}\sin\theta_j\,, \hat{\phi})^T$. *Here* $\hat{\phi} = \phi - \phi_j$, *and* $\hat{\theta} = \theta - \theta_j$, *with* $\hat{\phi} \ll 1$ *and* $\hat{\theta} \ll 1$.

Proof We let $x = (\cos\phi\sin\theta, \sin\phi\sin\theta, \cos\theta)^T$. Upon linearizing with $\phi = \phi_j + \hat{\phi}$ and $\theta = \theta_j + \hat{\theta}$, where $\hat{\phi} \ll 1$ and $\hat{\theta} \ll 1$, we obtain in terms of a 3×2 matrix M_0 that

$$x = x_j + M_0 y + \mathcal{O}(|y|^2)\,, \qquad \text{where} \qquad M_0 \equiv \begin{pmatrix} -\sin\phi_j & \cos\phi_j\cos\theta_j \\ \cos\phi_j & \sin\phi_j\cos\theta_j \\ 0 & -\sin\theta_j \end{pmatrix}\,, \quad \text{and} \quad y \equiv \begin{pmatrix} \hat{\phi}\sin\theta_j \\ \hat{\theta} \end{pmatrix}\,,$$

where $\mathcal{O}(|y|^2)$ indicates quadratic terms in y_1 and y_2. We calculate $|x - x_j|^2 \sim (M_0 y^T)(M_0 y) = y^T M_0^T M_0 y$, and readily verify that $M_0^T M_0 = I$. Therefore, $|x - x_j| = |y|(1 + o(1))$ as $x \to x_j$. □

Appendix C An Instability Criterion for an NLEP

The following result gives a sufficient condition for the NLEP of (4.37) to admit an (unstable) positive real eigenvalue.

Lemma C.1 *The NLEP (4.37) has a a positive real eigenvalue whenever both* $0 < \beta(0) < 1$ *and* $\mathcal{C}(\lambda) \equiv 1/\beta(\lambda)$ *is analytic in* $Re(\lambda) \geq 0$.

Proof The eigenvalues of (4.37) are the roots of $g(\lambda) \equiv \mathcal{C}(\lambda) - \mathcal{F}(\lambda) = 0$, where $\mathcal{C}(\lambda) \equiv 1/\beta(\lambda)$ and $\mathcal{F}(\lambda)$ is defined in (4.44) in terms of the local operator $L_0\Psi \equiv \Delta_\rho\Psi - \Psi + 2w\Psi$ and the ground-state solution w of (4.7). It is well-known that the local problem $L_0\Psi = \sigma\Psi$ has a unique positive eigenvalue $\sigma_0 > 0$ (cf. [**44**]). We will establish that

$$\mathcal{F}(0) = 1\,; \qquad \mathcal{F}(\lambda) \to +\infty \quad \text{as} \quad \lambda \to \sigma_0^-\,; \qquad \mathcal{F}'(\lambda) > 0 \quad \text{for} \quad 0 < \lambda < \sigma_0\,. \tag{C.1}$$

We first use the identity $L_0 w = w^2$ to derive $\mathcal{F}(0) = \int_0^\infty w L_0^{-1} w^2 \rho\, d\rho / \int_0^\infty w^2 \rho\, d\rho = 1$. Then, since $L_0 - \lambda$ is not invertible at $\lambda = \sigma_0$ it follows that $(L_0 - \lambda)^{-1}$ is unbounded as $\lambda \to \sigma_0^-$ and so $\mathcal{F}(\lambda) \to +\infty$ as $\lambda \to \sigma_0^-$. To prove the monotonicity of $\mathcal{F}(\lambda)$, we use $L_0 w = w^2$ to re-write $\mathcal{F}(\lambda)$ as

$$\mathcal{F}(\lambda) = \frac{\int_0^\infty \rho w (L_0 - \lambda)^{-1} L_0 w\, d\rho}{\int_0^\infty \rho w^2\, \rho} = \frac{\int_0^\infty \rho w (L_0 - \lambda)^{-1}\left[(L_0 - \lambda)w + \lambda w\right]\, d\rho}{\int_0^\infty \rho w^2 d\rho} = 1 + \lambda\left(\frac{\int_0^\infty \rho w (L_0 - \lambda)^{-1} w\, d\rho}{\int_0^\infty \rho w^2 d\rho}\right)\,.$$

Upon differentiating this last expression, and then integrating the resulting expression by parts, we calculate that

$$\mathcal{F}'(\lambda) = \frac{h(\lambda)}{\int_0^\infty \rho w^2 d\rho} + \lambda\frac{\int_0^\infty \rho w (L_0 - \lambda)^{-2} w\, d\rho}{\int_0^\infty \rho w^2\, d\rho} = \frac{h(\lambda)}{\int_0^\infty \rho w^2 d\rho} + \lambda\frac{\int_0^\infty \left[(L_0 - \lambda)^{-1} w\right]^2 \rho\, d\rho}{\int_0^\infty \rho w^2 d\rho}\,, \tag{C.2}$$

where $h(\lambda)$ is defined by $h(\lambda) \equiv \int_0^\infty \rho w (L_0 - \lambda)^{-1} w\, d\rho$. The second term in the last equality in (C.2) is positive for $0 < \lambda < \sigma$. Therefore, to prove that $\mathcal{F}'(\lambda) > 0$ on $0 < \lambda < \sigma_0$ it suffices to prove that $h(\lambda) > 0$ on $0 < \lambda < \sigma_0$.

To establish the positivity of $h(\lambda)$ on $0 < \lambda < \sigma_0$ we will prove that $h(0) > 0$ and $h'(\lambda) > 0$ on $0 < \lambda < \sigma_0$. By using the readily-verified identity $L_0^{-1} w = w + \frac{1}{2}\rho w'$, we calculate $h(0)$ as

$$h(0) = \int_0^\infty \rho w \left(w + \frac{1}{2}\rho w'\right)\, d\rho = \int_0^\infty \rho w^2 d\rho + \frac{1}{4}\int_0^\infty \rho^2 \left(w^2\right)'\, d\rho\,.$$

Upon integrating by parts, we get $h(0) = \frac{1}{2}\int_0^\infty \rho w^2 d\rho > 0$. We then calculate $h'(\lambda) = \int_0^\infty \rho w (L_0 - \lambda)^{-2} w\, d\rho = \int_0^\infty \rho \left[(L_0 - \lambda)^{-1} w\right]^2\, d\rho > 0$, so that $h(\lambda) > 0$ on $0 < \lambda < \sigma_0$. Thus, from (C.2), we get $\mathcal{F}'(\lambda) > 0$ on $0 < \lambda < \sigma_0$, which proves the last result in (C.1).

With properties (C.1) for $\mathcal{F}(\lambda)$, it follows that if $\mathcal{C}(0) > 1$ and $\mathcal{C}(\lambda)$ is analytic in $\mathrm{Re}(\lambda) \geq 0$, then $\mathcal{C}(\lambda)$ and $\mathcal{F}(\lambda)$ must cross at some real $\lambda^\star$ in $0 < \lambda^\star < \sigma_0$. Thus, $\lambda^\star$ is an unstable discrete eigenvalue of the NLEP (4.37). □

Appendix D Spectrum of a Circulant-Symmetric Matrix

When $\mathcal{G}$ or $\mathcal{G}_\lambda$ is an $N \times N$ circulant-symmetric matrix with complex-valued entries, its eigenvectors $\mathbf{b_j}$ and eigenvalues k_j can be determined analytically. Let $\mathbf{a} = (a_1, \ldots, a_N)$ denote the first row of this matrix, with the remaining rows obtained by cycling the components of the vector $\mathbf{a}$. In addition, since the matrix is also symmetric it follows that $a_j = a_{N+2-j}$ for $j = 2, \ldots, \lceil N/2 \rceil$, where the ceiling function $\lceil x \rceil$ is the smallest integer not less than x. The well-known spectrum of a circulant matrix is

$$k_j = \sum_{m=0}^{N-1} a_{m+1} e^{2\pi(j-1)m/N}\,, \qquad \mathbf{b_j} = (1, e^{2\pi(j-1)/N}, \ldots, e^{2\pi(j-1)(N-1)/N})^T\,, \qquad j = 1, \ldots, N\,. \tag{D.1}$$

The symmetry of the matrix implies that $a_j = a_{N+2-j}$ and $\mathbf{b_j} = \mathbf{b_{N+2-j}}$, so that $b_{jm} = b_{j(N+2-m)}$ for $m = 2, \ldots, \lceil N/2 \rceil$ and $j = 2, \ldots, \lceil N/2 \rceil$. Here b_{jm} is the m-th component of $\mathbf{b_j}$. Since the eigenvalue is $k_j = \mathbf{b_j} \cdot \mathbf{a}$, we have $k_j = k_{N+2-j}$. This generates $\lceil N/2 \rceil - 1$ eigenvalues with multiplicity two, whose eigenvectors can be obtained by taking any linear combination of two complex conjugate eigenvectors. For instance, for the j-th eigenvalue k_j the corresponding two eigenvectors can be taken as the real and imaginary parts of $\mathbf{b_j}$, respectively. This yields the following result for the spectrum of the $N \times N$ circulant-symmetric matrix whose first row vector is $\mathbf{a} = (a_1, \ldots, a_N)$:

$$\begin{cases} k_1 & = \sum_{m=1}^{N} a_m\,, \quad \mathbf{b_1}^T = (1, \ldots, 1)\,, \\ k_j & = \sum_{m=0}^{N-1} \cos\left(\frac{2\pi(j-1)\,m}{N}\right) a_{m+1}\,, \quad \text{eigenvalues with multiplicity } 2\,, \\ \mathbf{b_j}^T & = \left(1, \cos\left(\frac{2\pi(j-1)}{N}\right), \ldots, \cos\left(\frac{2\pi(j-1)(N-1)}{N}\right)\right)\,, \\ \mathbf{b}_{N+2-j}^T & = \left(0, \sin\left(\frac{2\pi(j-1)}{N}\right), \ldots, \sin\left(\frac{2\pi(j-1)(N-1)}{N}\right)\right)\,, \quad j = 2, \ldots, \lceil N/2 \rceil + 1\,. \end{cases} \tag{D.2}$$

Note that if N is even, then $k_{(\lceil N/2 \rceil + 1)} = \sum_{m=1}^{N} (-1)^{m-1} a_m$ is a simple eigenvalue with eigenvector $(1, -1, \ldots, 1, -1)^T$.

For illustration, let $N = 3$. Then, the eigenvalues are $k_1 = a_1 + a_2 + a_3$ and $k_2 = k_3 = a_1 - a_2$, while the corresponding eigenvectors are $\mathbf{b_1} = (1, 1, 1)^T$, $\mathbf{b_2} = (1, -0.5, -0.5)^T$ and $\mathbf{b_3} = (0, \sqrt{3}/2, -\sqrt{3}/2)^T$.

References

[1] M. Abramowitz, I. Stegun, *Handbook of mathematical functions*, 9th edition, New York, NY, Dover Publications.

[2] N. N. Andreev, *An extremal property of the icosahedron*, East J. Approx., **2**(4), (1996), pp. 459–462.

[3] R. Barreira, C. A. Elliott, A. Madzvamuse, *The surface finite element method for pattern formation on evolving biological surfaces*, J. Math. Biol. **63**, (2011), pp. 1095-1109.

[4] S. Boatto, *Curvature perturbations and stability of a ring of vortices*, DCDS-B, **10**(2-3), (2008), pp. 349–375.

[5] S. Boatto, C. Simo, *Thomson's heptagon: A case of bifurcation at infinity*, Physica D, **237**(14), (2008), pp. 2051–2055.

[6] J. S. Brauchart, D. P. Hardin, E. B. Saff, *The next-order term for minimal Riesz and logarithmic energy asymptotics on the sphere*, Contemp. Math., **578**, (2012), pp. 31–61.

[7] T. K. Callahan, *Turing patterns with O(3) symmetry*, Physica D, **188**(1), (2004), pp. 65–91.

[8] M. A. J. Chaplain, M. Ganesh, I. G. Graham, *Spatio-temporal pattern formation on spherical surfaces: numerical simulation and application to solid tumour growth*, J. Math. Biology, **42**(5), (2001), pp. 387-423.

[9] P. Chossat, R. Lauterbach, I. Melbourne, *Steady-sate bifurcation with $O(3)$ symmetry*, Arch. Rat. Mech. Anal., **113**, (1990), pp. 313–376.

[10] W. Chen, M. J. Ward, *The stability and dynamics of localized spot patterns in the two-dimensional Gray-Scott model*, SIAM J. Appl. Dyn. Sys., **10**(2), (2011), pp. 582–666.

[11] D. Coombs, R. Straube, M. J. Ward, *Diffusion on a sphere with localized traps: mean first passage time, eigenvalue asymptotics, and Fekete points*, SIAM J. Appl. Math., **70**(1), (2009), pp. 302332.

[12] P. D. Dragnev, D. A. Legg, D. W. Townsend, *Discrete logarithmic energy on the sphere*, Pacific J. of Math., **207**(2), (2002), pp. 345–358.

[13] J. Gjorgjieva, J. Jacobsen, *Turing patterns on growing spheres: the exponential case*, DCDS supplement (special issue), (2007), pp. 436-445.

[14] T. Kolokolnikov, M. J. Ward, J. Wei, *Spot self-replication and dynamics for the Schnakenberg Model in a two-dimensional domain*, J. Nonlinear Sci., **19**(1), (2009), pp. 1–56.

[15] S. Kondo, R. Asai, *A reaction–diffusion wave on the skin of the marine angelfish Pomacanthus*, Nature, **376**, (1995), pp. 765-768.

[16] A. V. Kolushov, V. A. Yudin, *Extremal dispositions of points on the sphere*, Anal. Math., **23**, No. 1, (1997), pp. 25–34.

[17] C. Landsberg, A. Voigt, *A multigrid finite element method for reaction-diffusion systems on surfaces*, Comput. Visual Sci., **13**, (2010), pp. 177–185.

[18] C. S. Lin, W. M. Ni, I. Takagi, *Large amplitude stationary solutions to a chemotaxis system*, J. Diff. Eq., **72**(1), (1988), pp. 1-27.

[19] C. B. Macdonald, S. J. Ruuth, *The implicit closest point method for the numerical solution of partial differential equations on surfaces*, SIAM J. Sci. Comp., **31**(6), (2009), pp. 4330-4350.

[20] C. B. Macdonald, B. Merriman, S. J. Ruuth, *Simple computation of reaction-diffusion processes on point clouds*, Proc. Natl. Acad. Sci. U.S.A., **110**(23), (2013), pp. 9209–9214.

[21] C. B. Macdonald, S. J. Ruuth, *Level set equations on surfaces via the closest point method*, J. Sci. Comput., **35**(2–3), (2008), pp. 219–240.

[22] P. C. Matthews, *Pattern formation on a sphere*, Phys. Rev. E., **67**(3), (2003), pp. 036206.

[23] P. C. Matthews, *Transcritical bifurcation with $O(3)$ symmetry*, Nonlinearity, **16**, (2003), pp. 1449-1471.

[24] W. Nagata, L. G. Harrison, S. Wehner, *Reaction-diffusion models of growing plant tips: bifurcations on hemispheres*, Bull. of Math. Biology, **6**(4), (2003), pp. 571–607.

[25] P. K. Newton, T. Sakajo, *Point vortex equilibria and optimal packings of circles on a sphere*, Proc. Roy. Soc. A, **467**, (2011), pp. 1468–1490.

[26] P. K. Newton, *The N-Vortex Problem: Analytical Techniques*, Springer, New York, (2001).

[27] Y. Nishiura, *Far-from equilibrium dynamics, translations of mathematical monographs*, Vol. **209**, (2002), AMS Publications, Providence, Rhode Island.

[28] K. J. Painter, *Modelling of pigment patterns in fish: book chapter in mathematical models for biological pattern formation. editors P. K. Maini, H. G. Othmer*, IMA Vol. in Math and its Applications, **121**, (2000), pp. 59–82. Springer-Verlag.

[29] B. Peña, C. Pérez-Garcia, *Stability of Turing patterns in the Brusselator model*, Phys. Rev. E., **64**(5), (2001), pp. 056213.

[30] R. G. Plaza, F. Sánchez-Garduño, P. Padilla, R. A. Barrio, P. K. Maini, *The effect of growth and curvature on pattern formation*, J. Dynam. Diff. Eq., **16**(4), (2004), pp. 1093-1121.

[31] I. Prigogine, R. Lefever, *Symmetry breaking instabilities in dissipative systems. II*, J. Chem. Physics, **48**, (1968), pp. 1695.

[32] E. A. Rakhmanov, E. B. Saff, Y. M. Zhou, *Minimal discrete energy on the sphere*, Math. Res. Lett., **1**, No. 6, (1994), pp. 647–662.

[33] S. J. Ruuth, *Implicit-explicit methods for reaction-diffusion problems in pattern formation*, J. Math. Biol., **34**(2), (1995), pp. 148–176.

[34] S. J. Ruuth, B. Merriman, *A simple embedding method for solving partial differential equations on surfaces*, J. Comput. Physics, **227**(3), (2008), pp. 1943–1961.

[35] E. B. Saff, A. Kuijlaars, *Distributing many points on a sphere*, The Mathematical Intelligencer, **19**(1), (1997), pp. 5–11.

[36] R. Szmytkowski, *Closed form of the generalized green's function for the Helmholtz operator on the two-dimensional unit sphere*, J. Math. Phys., **47**(6) (2006), 063506, 11 pp.

[37] V. Smyshlyaev, *The high-frequency diffraction of electromagnetic waves by cones of arbitrary cross-section*, SIAM J. Appl. Math., **53**, No. 3, (1993), pp. 670–688.

[38] A. Turing, *The Chemical Basis of Morphogenesis*, Phil. Trans. Roy. Soc. B, **327**, (1952), pp. 37–72.

[39] J. C. Tzou, A. Bayliss, B. J. Matkowsky, V. A. Volpert, *Stationary and slowly moving localized pulses in a singularly perturbed Brusselator model*, Europ. J. Appl. Math., **22**(5), (2011), pp. 423–453.

[40] J. C. Tzou, Y. Nec, M. J. Ward, *The stability of localized spikes for the 1-D Brusselator reaction-diffusion model*, Europ. J. Appl. Math., **24**(4), (2013), pp. 515–564.

[41] C. Varea, J. L. Aragón, R. A. Barrio, *Turing patterns on a sphere*, Phys. Rev. E., **60**(4), (1999), pp. 4588-4592.

[42] M. J. Ward, J. Wei, *Hopf bifurcation of spike solutions for the shadow Gierer-Meinhardt model*, Europ. J. Appl. Math., **14**(6), (2003), pp. 677–711.

[43] M. J. Ward, J. Wei, *Hopf bifurcations and oscillatory instabilities of spike solutions for the one-dimensional Gierer-Meinhardt model*, J. Nonlinear Sci. **13**(2), (2003), pp. 209–264.

[44] J. Wei, *On single interior spike solutions of the Gierer-Meinhardt system: uniqueness and spectrum estimates*, Europ. J. Appl. Math., **10**(4), (1999), pp. 353–378.

[45] J. Wei, M. Winter, *Spikes for the two-dimensional Gierer-Meinhardt system: the weak coupling case*, J. Nonlinear Sci., **11**(6), (2001), pp. 415–458.

[46] J. Wei, M. Winter, *Existence and stability of multiple spot solutions for the Gray-Scott model in $\mathbb{R}^2$*, Physica D, **176**(3-4), (2003), pp. 147-180.

[47] J. Wei, M. Winter, *Asymmetric spotty patterns for the Gray-Scott model in R^2*, Studies in Appl. Math., **110**(1) (2003), pp. 63–102.

[48] J. Wei, M. Winter, *Stationary multiple spots for reaction-diffusion systems*, J. Math. Biol., **57**(1), (2008), pp. 53–89.